Additive Manufacturing and Other Techniques for Fabrication of Foams and Electrically Conductive Polymer Composites

by

Adam N. Ostashek

A thesis submitted in partial fulfillment of the requirements for the degree of

Master of Science

Department of Mechanical Engineering

University of Alberta

Abstract

In this thesis, two aspects of advanced uses for additive manufacturing and microfabrication are investigated: stretchable electronics and polymer foams. These topics were initially part of an extended project effort to develop new capabilities in deformable, high-frequency antennas and the ability to rapidly prototype using combinations of materials that had previously required complex hand assembly. Several methods were investigated in which stretchable electronic devices were fabricated. A horn antenna with a reconfigurable reflector was designed and fabricated using EcoFlex silicone rubber and eutectic gallium indium (eGaIn) to comprise the deformable reflector. A method to produce stretchable electrical wires using an inexpensive consumer-grade fused deposition manufacturing (FDM) 3D printer was developed. Electrically conductive wires, a resistive spiral pressure sensor, and an inductive spiral strain sensor were printed and characterized. Electrical conductivity was achieved in all of the printed devices up to an elongation of 500 %.

The utility of foams in this work are that the structural materials reduce their impact on the high frequency performance of electronics, as air has lower inherent losses than solid materials. Foams are also highly useful for lightweight printing applications or in industries like metal casting, where lost foam casting is a common way to produce complex metal parts. The sections of this thesis that discuss foams pertain to applications in functionally graded materials, where the amount of porogen can be varied throughout the thickness of the foam, and applications in the foundry industry. Several foams made from poly(styrene-b-(ethylene-co-butylene)-b-styrene) (SEBS), poly(lactic acid) (PLA), and linear low density polyethylene (LLDPE) were produced and investigated for extensibility and applicability to the lost foam metal casting process. SEBS foams

were successfully fabricated via solution casting using widely available, inexpensive soluble templates. A commercially available foaming PLA filament was used to make an expendable pattern for a grey iron casting and the final product was visually characterized. Custom LLDPE filaments containing chemical foaming agents were produced and investigated for their applicability as an alternative material for lost foam patterns.

Preface

This thesis is an original work by Adam Ostashek under the supervision of Dr. Dan Sameoto. All of the fabrication and characterization of the experiments within took place at the University of Alberta in the Polymer Microfabrication Lab, nanoFAB, and Intelligent Wireless Technology Lab, and at Norwood Foundry. The experiments in Chapter 5 were performed in collaboration with the Intelligent Wireless Technology Lab, led by Pedram Mousavi. The design of the horn antenna was done by Dr. Rashid Mirzavand, and characterization of the reflectors was done by Rashid Mirzavand and Mahdi Honari. Chapter 6 is published as a journal article: Khondoker, M. A. H., Ostashek, A., & Sameoto, D. (2019), "Direct 3D Printing of Stretchable Circuits via Liquid Metal Co-Extrusion Within Thermoplastic Filaments", Advanced Engineering Materials, 21(7). I assisted in experiment design, fabrication, characterization, and manuscript preparation.

Acknowledgements

I would first like to thank my parents, for instilling in me a lifelong desire to seek and solve challenges and supporting me throughout my educational pursuits.

Secondly, I would like to thank my partner Breanna for her support, patience, advice, encouragement, and love throughout this endeavor.

I would also like to thank Dr. Dan Sameoto for sharing his knowledge, wisdom, and contagious enthusiasm towards innovation and for agreeing to supervise my research.

I would also like to thank Dr. Pedram Mousavi for acting as my co-supervisor and providing me with an initial direction in which to steer my research.

I would also like to thank all of the members of Dr. Sameoto's lab, among whom I have found fantastic colleagues and friends. I give you my utmost gratitude for the work we have done together and wish for your continued successes.

I would also like to thank Brant Dornan for allowing me to conduct lost foam experiments in the foundry and for allowing the use of Norwood foundry's characterization equipment.

I would also like to thank Taher Hosseinzadeh for his mentorship and introduction to the lost foam process.

Finally, I would like to thank those who have had instrumental roles over the years in steering me towards this path, whether directly or indirectly.

Contents

List of Tables ix

List of Figures x

Chapter 1: Introduction 1

Chapter 2: Polymer Foams 3

2.1 Background 3

2.2 Elastomeric Foams 5

2.2.1 Thermoplastic Elastomeric Foams 5

2.2.2 Thermoset Elastomeric Foams 6

2.3 Foaming Agents 8

Chapter 3: SEBS Foam 10

3.1 Introduction 10

3.2 Experimental 10

3.3 Results and Discussion 14

3.3.1 SEBS with NaCl as a Porogen 14

3.3.2 SEBS with Glucose as a Porogen 17

3.3.3 SEBS with MSG as a Porogen 17

3.4 Conclusion and Future Work 20

Chapter 4: Lost Foam Casting from Additively Manufactured Foam 22

4.1 Lost Foam Casting 22

4.2 PLA Foam 25

4.3 Lost PLA Foam Casting 28

4.4 Additively Manufactured LLDPE Foam 40

4.5 Conclusion and Future Work 43

Chapter 5: Liquid Metal Reconfigurable Reflector 45

5.1 Background 45

5.2 Experimental 51

5.2.1 Horn and Waveguide 51

5.2.2 Reflector 52

5.2.2.1 Pinned Reflector 54

5.2.2.2 EcoFlex Lamination 57

5.2.2.3 eGaIn Composite 58

5.2.3 Assembly 65

5.2.4 Actuation 68

5.3 Conclusion and Future Work 69

Chapter 6: Direct 3D Printing of Stretchable Circuits via Liquid Metal Co-Extrusion within Thermoplastic Filaments 70

6.1 Introduction 70

6.2 Experimental 71

6.2.1 Stretchable Wires 72

6.2.2 Spiral Pressure Sensor 73

6.2.3 3D Spiral Inductor 75

6.3 Results and Discussion 76

6.3.1 Drawing of the LM Wire 83

6.4 Conclusion and Future Work 85

Chapter 7: Conclusion 87

Bibliography 89

Appendices 106

Appendix A – Table of Material Properties 107

Appendix B – Reconfigurable Horn Antenna Drawing 108

Appendix C – Phase Diagram 111

List of Tables

Table 1. Comparison of Expanded Polystyrene Foam Versus Bulk Polystyrene. 3

Table 2. Dimensions of foam samples for characterization. 14

Table 3. CR-10 Parameters for Printing LW-PLA 28

Table 4. CR-10 v3 Parameters for Printing LLDPE Foaming Filament 40

Table 5. List of Low-Melting Point Pure Metals and Alloys 45

Table 6. Low Earth Orbit Environmental Effects [97]–[99] 49

List of Figures

Figure 1. Global Polymer Foam Market Share 2019 (Adapted from [27]). 4

Figure 2. SEBS monomer. The subscripts **m**, **x**, **y**, **n**, and **p** denote the number of each molecule and block (styrene, ethylene, butylene, ethylene-butylene block, and styrene, respectively) in the monomer. 6

Figure 3. Chalk-Harrod mechanism for addition-cured silicones (Adapted from [42], [43]). 7

Figure 4. Optical microscopy image of NaCl crystals. 12

Figure 5. Optical microscopy image of MSG crystals. 13

Figure 6. SEM image of SEBS/NaCl foam at 50 X magnification. A large undissolved NaCl crystal is visible in the top left of the image. Smaller NaCl pieces are shown strewn around the image. 15

Figure 7. SEM image of SEBS/NaCl foam at 400 X magnification. Small undissolved flecks of NaCl are visible embedded in the SEBS fibres. 16

Figure 8. SEM image of SEBS/NaCl foam at 1000 X magnification. Small undissolved flecks of NaCl are visible embedded in the SEBS fibres. 17

Figure 9. SEM image of SEBS/MSG foam at 50 X magnification. 18

Figure 10. SEM image of SEBS/MSG foam at 400 X magnification. The pore size becomes more regular at smaller domain lengths. 19

Figure 11. SEM image of SEBS/MSG foam at 1000 X magnification, showing measurments of pore size. 20

Figure 12. Schematic showing gaseous EPS decomposition products diffusing through the refractory coating into the surrounding sand. 23

Figure 13. PLA foams produced with MSG. (a) before sonication, (b) after sonication. 26

Figure 14. PLA foams produced with dextrose. (a) Before sonication, (b) After Sonication. 27

Figure 15. PLA foams produced with NaCl. (a) before sonication, (b) after sonication. 27

Figure 16. LW-PLA Calibration Shells. 29

Figure 17. LW-PLA Test Structures. Top: Athena of Velletri. Bottom: Mini All-in-One Printer Test. 30

Figure 18. Test pattern after printing. Note the severe branching on high detail features. 32

Figure 19. Side view of the test pattern showing the downsprue (outlined in blue) and the runner (outlined in orange). The printed downsprue was replaced with a piece of Type II EPS in order to make filling easier. 33

Figure 20. Expendable medieval cannon pattern. Left: before assembly. Right: partially assembled. The split sprue is shown at the bottom right. 34

Figure 21. Fully assembled medieval cannon pattern. 35

Figure 22. Left: Test pattern coated with Holcote 3100. Right: Test pattern molded in sand. 36

Figure 23. Left: Cannon pattern coated with Holcote 3100. Right: Cannon pattern molded in sand. 36

Figure 24. Test pattern casting. The EPS downsprue and the LW-PLA runner are visible. 38

Figure 25. Medieval cannon casting. The level of detail replication is high, with layer lines visible. 39

Figure 26. Relationship between extrusion temperature and foaming agent loading for LLDPE foams. 41

Figure 27. Top: LLDPE-F Test shells at 2 % F60 loading. Bottom: Optimized flow rate to achieve a wall thickness of 0.4 mm. 42

Figure 28. Top: LLDPE-F Test shells at 2 % F60 loading. Bottom: Samples tested at various flow rates to achieve a wall thickness of 0.4 mm. 43

Figure 29. Proposed design of reconfigurable horn antenna. The orange section is the waveguide, the yellow section is the horn, and the purple section is the reconfigurable reflector. 51

Figure 30. Assembled horn and waveguide. 52

Figure 31. Initial attempts at fabricating a stretchable reflector. (a) Pinning the liquid metal to steel balls, (b) EcoFlex laminated on top of liquid metal, (c) EcoFlex/liquid metal composite. 54

Figure 32. Top: schematic process flow of reflector fabrication. Bottom: intermediate steps in fabrication of a pinned reflector. 56

Figure 33. EcoFlex encapsulation defects encountered when casting too close to the end of the pot life. 57

Figure 34. Laminated reflector showing before (left) and after (right) massaging out air bubbles from the eGaIn. 58

Figure 35. Optical microscopy image of EcoFlex 00-30 containing 10 wt.% eGaIn. 59

Figure 36. Optical microscopy image of EcoFlex 00-30 containing 20 wt.% eGaIn. 60

Figure 37. Optical microscopy image of EcoFlex 00-30 containing 30 wt.% eGaIn. 61

Figure 38. Optical microscopy image of EcoFlex 00-30 containing 60 wt.% eGaIn. 62

Figure 39. Escape of eGaIn out of the composite after applying mechanical pressure. 63

Figure 40. Reflection coefficient results (S11) for EcoFlex 00-30/eGaIn composite films. (Clockwise from top left) 10 wt.% eGaIn, 20 %wt. eGaIn, 30 %wt. eGaIn, 60 %wt. eGaIn. 64

Figure 41. Reflector thickness distribution. 65

Figure 42. Reflector containing eGaIn prior to top layer lamination. Left inset: eGaIn that overflowed and penetrated between the paper mask and EcoFlex. Right inset: Oxidized eGaIn around air bubble pockets. 66

Figure 43. Assembled horn, waveguide, and reflector. 67

Figure 44. Side and top views for actuation system for reconfigurable reflector antenna. 68

Figure 45. (a) 3D schematic of a 2D spiral pressure sensor composed of SEBS channels with a LM core printed directly on a SEBS substrate. (b) Experimental setup to measure change in electrical resistance as a function of pressure applied with no load and (c) with a load of 3.2 kg. Used with permission from [50]. 74

Figure 46. (a) SEBS/eGaIn spiral resistor pressure sensor. (b) Percent change of electrical resistance of the pressure sensor as a function of the applied pressure. Used with permission from [50]. 75

Figure 47. SEBS/eGaIn 3D spiral inductor. Used with permission from [50]. 76

Figure 48. (a) Exploded view of the tri-extruder assembly used for coaxial extrusion, (b) Schematic of the 3D printing system showing the syringe pump at the top left, the pellet extruder at the top right with the heated hose (orange) and silicone tubing leading to the 3D printer nozzle, (c) Schematic view of the nozzle outlet. Inset: Detail view of the nozzle exit showing the coaxial nozzle diameters (d_o and d_i), the surface tension force of the LM (F_T), and the viscous drag force imparted by the SEBS (F_D). (d) Illustration showing the effect of surface tension dominating due to low viscosity of the polymer at high temperatures. (e) Illustration showing viscous drag of the SEBS being greater than the surface tension of the LM. Used with permission from [50]..... 77

Figure 49. (a) State diagram showing the relationship between the Ca number of SEBS and the We number of LM, and how it affects the coaxial extrusion regime. The hatched region shows combinations of Ca and We numbers at which jet formation is not possible. A transition from the droplet regime to the continuous jet regime as the temperature increases from (b) 180 °C to (c) 200 °C is shown with flow rates of 2 mm/s and 2.5 mm/s for SEBS and LM, respectively. (d)

Microscope image showing that increasing the flow rate of the LM caused the LM to be continuous and increase in diameter as the flow rate was further increased. Scale bars are 1 mm. Used with permission from [50]..... 81

Figure 50. (a)-(d) Various cross-sections produced by holding the Ca number of the SEBS constant but decreasing the We number of the LM. (e) and (f) show repeatable stretchability of the wire up to 400 % with no noticeable decrease in electrical properties. (g) and (h) show the ability for the wire do be thermally drawn from a core diameter of approximately 670 μm to approximately 190 μm. (i) Graph showing the relationship between drawing speed and resultant diameter with agreement between the experimental devices and the theoretical values. (j) shows a drawn wire attached to an LED with electrical conductivity in the wire preserved. Used with permission from [50]..... 82

Figure 51. Plot of loading and unloading cycles of a 10 cm long SEBS/LM wire showing the relative change in resistance over a total of 1010 cycles. Used with permission from [50]..... 85

Chapter 1: Introduction

Polymer microfabrication is a broad field in which manufacturing technologies are leveraged to produce polymeric devices with feature sizes on the order of approximately 100 nm – 100 μm. The field arose with the development of microelectronics in the 1960s and has continued to mature with the development of microelectromechanical systems (MEMS), microfluidics, and labs-on-a-chip, the latter of which combine aspects of the former three technologies.

In general, polymer microfabrication requires specialized machinery and is often performed in cleanroom labs which requires significant capital investment, in turn presenting large barriers for new companies entering the microfabrication industry worldwide [1], [2]. As technology continues to advance and more highly specialized components gain more demand, there is a need for alternative methods to produce advanced technologies with low-complexity and at a low-cost. In particular, prototyping with electronics or functional electro-mechanical devices is still very challenging to achieve and is an underexamined area where additive manufacturing can make significant advances [3]. This thesis investigates the usage of additive manufacturing and gallium-based room temperature liquid metal alloys (LM) in several applications that suffer from several limitations in their current designs [4]–[11]. The original purpose was to support a strategic grant on the topic of additive manufacturing of stretchable electronics, but funding ended when the commercial partner left Canada. Alternative applications for making foaming materials became prioritized for the second half of the work described in this thesis. Chapters 2-4 involve the production and applications of foamed polymers. Chapter 2 introduces a background of polymer foams and their various methods of production, with a focus on thermoplastic elastomers, which was the original application of the thesis work. This section of the project began after one of the lab's industrial partners ceased Canadian operations, and was an open-ended project based on literature review of functionally graded foams. Chapter 3 builds upon the discussions of Chapter 2 and discusses the production of SEBS foams using water-soluble templates [12], [13]. Several foams were produced, and their extensibility was measured. One foam was tested for its absorptivity to oil as a potential application in reusable hydrocarbon spill remediation. Chapter 4 introduces the lost foam casting process and details an attempt at lost foam casting using an

additively manufactured PLA foam, as well as detailing the production and application of an additively manufactured LLDPE foam. Two patterns were produced and cast, and the resultant castings were visually inspected. This project was developed after Dr. Pedram Mousavi tragically passed away, and a need for a new project application was required.

The final two chapters involve the combination of LM and elastomeric polymers. Chapter 5 discusses the manufacture of a reconfigurable horn antenna using an LM reflector. Chapter 6 discusses the production and application of additively manufactured, stretchable, and electrically conductive wires. This was based on and improved in collaboration with the PhD work of Dr. Hasan Khondoker.

Chapter 2: Polymer Foams

2.1 Background

Polymers are a type of material in which repeating chains of covalently-bonded molecules, called monomers, are interwoven or cross-linked in an amorphous and/or crystalline microstructure. Polymers can either be thermoplastic or thermosetting. Thermoplastics have a softening point in which the polymer chains become mobile, resulting in the ability to be formed into shapes multiple times. Thermosets are highly crosslinked, meaning that the polymer chains are not able to move relative to each other. When heated, thermosets will decompose or burn, rather than melt.

Polymer foams are comprised of cellular structures with a gas (typically air) filling the space between each cell. The cells can be either open or closed, where open-cell foams typically have lower tensile and compressive strengths and are more flexible than closed-cell foams. The cellular structure of polymeric foams yields a very low-density structure where more than 95 % of the material is gas. Typical densities of expanded polystyrene foam versus bulk polystyrene from extrusion or injection molding processes are shown in Table 1, where the void fraction (ϕ), expressed as a percentage, was calculated using Equation 1 [14].

$$\phi = 1 - \frac{\rho_{\text{Foam}}}{\rho_{\text{Bulk}}} \qquad \text{Eq. 1}$$

Table 1. Comparison of Expanded Polystyrene Foam Versus Bulk Polystyrene.

ASTM C578 Grade [15]	**Type XI**	**Type I**	**Type VIII**	**Type II**	**Type IX**	**Bulk Polystyrene**
Minimum Density [kg/m^3]	12	15	18	22	29	1050
Void Fraction [%]	98.9	98.6	98.3	97.9	97.2	0

Polymer foams are a class of material that is used in a wide variety of industries with the construction, packaging, automotive, and furniture markets comprising 80 % of the global market, shown in Figure 1. Polymer foams can have a high strength-to-weight ratio and large surface area, which lead to applications in force dampening [16], [17], lightweighting [12], [18], and thermal insulation [15]. The structure and large surface area of polymer foams have also led to applications in scaffolding and filtration [19]–[22], and their low density has led to applications in the metal casting industry as consumable patterns [23]–[26].

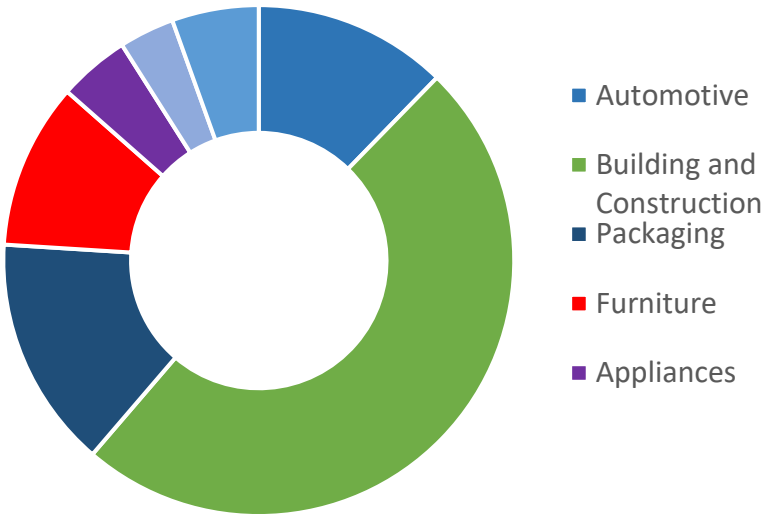

Figure 1. Global Polymer Foam Market Share 2019 (Adapted from [27]).

The goal of this part of the thesis is to determine a suitable composition of porogen and thermoplastic polymer that can be used for producing polymer foam structures in arbitrary shapes, and then characterizing the physical and absorptive properties of the produced foams. This work focuses on thermoplastic foams due to their recyclability, ability to be 3D printed, low viscosity in solution, and combustibility. Two types of porogens will be investigated: 1) porogens that decompose into gaseous products while the polymer is in a molten, rubbery state, and 2) porogens that must be removed via chemical means. A PDMS foam was also produced to compare with results in literature [13], [19], [20], [28]. The following sections will introduce polymeric elastomers and detail methods for polymer foam production.

2.2 Elastomeric Foams

An elastomer is a polymer that has a low Young's modulus, a comparatively large bulk modulus, and is able to deform elastically by several hundred percent before failure [29]. Its extensibility is due to the initial reconfiguration of long polymer chains upon tensile forces compared to the stretching of bonds seen in linear elastic materials. Elastomeric foams are elastomers that exhibit a combination of the properties of both elastomers and foams, such as low density and high mechanical compliance.

Elastomeric foams see uses in similar fields as rigid foams, such as in the packaging industry, but they also are common in energy dissipation [17], [30], aerospace [31], [32], consumer goods [33], and medical applications [34].

2.2.1 Thermoplastic Elastomeric Foams

Thermoplastic elastomer foams (TEF) are made from thermoplastic polymers, which are polymers that are able to melt and be formed into a variety of shapes using a variety of processing methods. ISO 18064 [35] classifies commercial thermoplastic elastomers into six groups: Styrenic block copolymers, thermoplastic polyolefinelastomers, thermoplastic vulcanizates, thermoplastic polyurethanes, thermoplastic copolyesters, and thermoplastic polyamides. Common processing methods include injection molding, thermoforming, blow molding, and extruding.

The TEF considered in this work focus primarily on styrene tri-block copolymer elastomers, more specifically, elastomers with the base structure poly(styrene-b-(ethylene-co-butylene)-b-styrene) (SEBS), as shown in Figure 2.

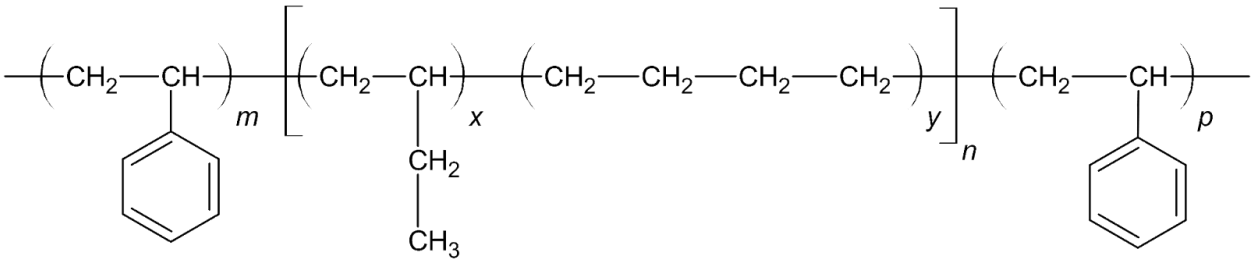

Figure 2. SEBS monomer. The subscripts **m**, **x**, **y**, **n**, and **p** denote the number of each molecule and block (styrene, ethylene, butylene, ethylene-butylene block, and styrene, respectively) in the monomer.

SEBS is a UV-, acid-, base-, and steam-resistant, highly stretchable, and biocompatible material. It also has a high extensibility and relatively high tensile strength. The combination of these properties is due to high strength provided by the polystyrene blocks in a glassy phase, and the high flexibility of the ethylene-butylene blocks above their glass transition temperature in a rubbery phase [36], [37].

2.2.2 Thermoset Elastomeric Foams

Thermoset elastomeric foams are comprised of crosslinked polymer chains that prevent dissolution and melting of the polymer due to strong covalent bonds. Crosslinking can be facilitated by homopolymerization via catalysts (RTV silicones) [38], [39], thermal curing (polyesters), light (electronics adhesives, additive manufacturing resin and binders) [40], [41], or copolymerization (2-part silicones and epoxies). They are not typically easily recycled once they are cured. However, thermoset polymers tend to have better mechanical properties and thermal stability compared to thermoplastics. The properties of the foam are highly dependent on the chain length (and therefore the molecular weight) of the initial oligomers, initial degree of crosslinking, and structure of the crosslinking agent.

In this work, platinum-catalyzed polydimethylsiloxane (PDMS) foams were investigated for their use as absorbent agents for oils. These are types of silicones which are comprised of two parts: a hydridosilane and a molecule with an unsaturated double bond in the presence of a platinum catalyst. The platinum catalyst facilitates the reaction between the molecules in the Chalk-Harrod mechanism, shown below in Figure 3. The process follows three main steps:

I_{HS}: oxidative addition of Si–H bonds to platinum

II_{HS}: migratory insertion of the coordinated alkene to Pt–H bond

III_{HS}: reductive elimination with the formation of Si–C bonds

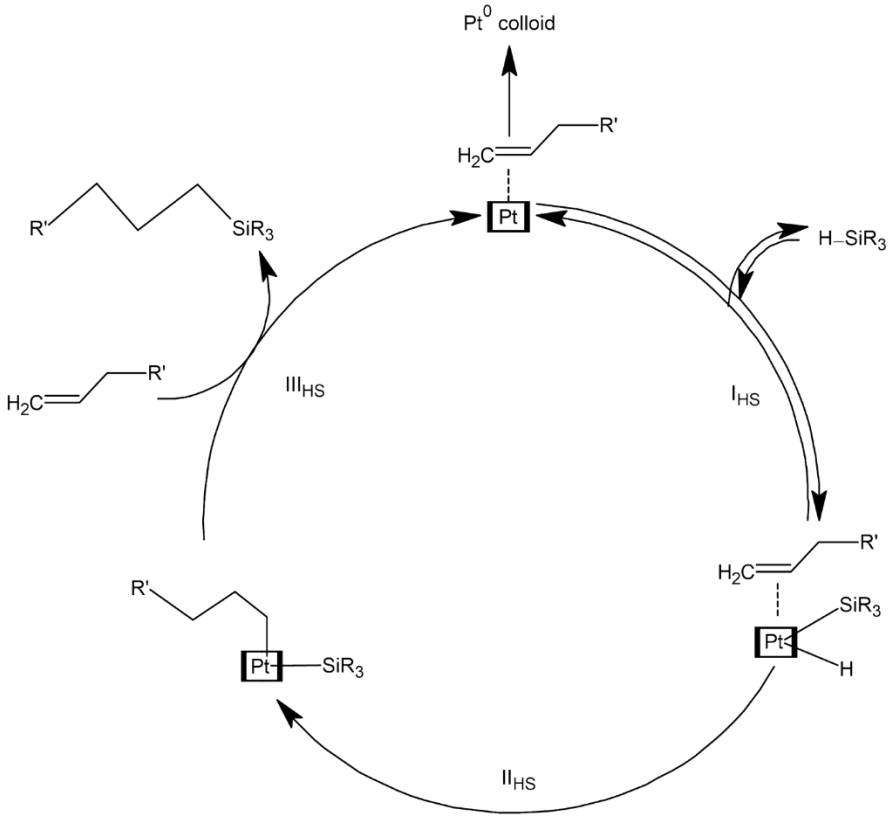

Figure 3. Chalk-Harrod mechanism for addition-cured silicones (Adapted from [42], [43]).

The platinum catalyst is typically composed of platinum and a number of alkene ligands. During oxidative addition (I_{HS}), a hydridosilane forms a complex with the Pt catalyst. Hydrogenation of

the alkene (II_{HS}) occurs from the hydrogen on the hydridosilane, followed by release of the hydrosilylized molecule. The platinum catalyst then repeats the cycle with more hydridosilanes.

2.3 Foaming Agents

Foaming agents are classified into two groups - physical and chemical. Physical foaming agents are pressurized gases that are injected directly into the melt prior to extrusion [14]. Upon exit from the extrusion nozzle, the gases expand, resulting in expansion of the polymer. In the case of EPS, pentane is added during the polystyrene polymerization step, creating spherical polystyrene pellets containing encapsulated pentane. The pellets are then pre-expanded in a steam environment before being molded and further steamed to produce the final desired shape. Gases for physical foaming typically are hydrocarbons (butane, pentane), supercritical N_2 or CO_2 [44], [45], and water [46]. Lee and Park investigated the use of nitrogen as a blowing agent in HDPE foams and found that the void fraction of the foams was insensitive to the die temperature, and was most affected by the content of talc as a nucleating agent [47]. Xu and Huang investigated the use of supercritical nitrogen as a foaming agent for PLA foams [45]. Sahnoune showed that PP/EPDM foams produced using water as a physical blowing agent had a 66 % density reduction from the bulk material [48].

Chemical foaming agents are those that undergo a chemical change during processing, typically from a thermal degradation reaction. Chemical foaming agents are classified into exothermic and endothermic types. Endothermic chemical foaming agents are typically inorganic and release CO_2 and/or other gases while absorbing the heat of the molten foam, which typically results in larger cells than exothermic foaming agents. Sodium carbonates and similar calcining compounds are often used in this case, as CO_2 and H_2O are both released during decomposition [14], [49]. Exothermic foaming agents are typically organic and release N_2 while increasing the foam temperature. Azo, diazo, and azido compounds such as azodicarbonamide or 4,4'-oxybis(benzenesulfonyl hydrazide) are organic exothermic chemical blowing agents which produce N_2 gas upon decomposition [14].

The foaming agents used in subsequent chapters are physical for producing SEBS and some PLA foams, whereby templates of water-soluble materials are used to produce an interconnected

structure and then dissolved after the polymer shape has been made. The foaming agents used in the lost foam section are chemical, and are added into a FDM 3D printer filament prior to printing.

Chapter 3: SEBS Foam

3.1 Introduction

SEBS has shown excellent potential as a thermoplastic material for polymer microfabrication. It can easily be processed in solution for casting of films, extruded [36], [37], [50], [51], and compression molded [44], [52]. SEBS has a very high elongation at failure (750 %), relatively high tensile strength (23.4 MPa), low hardness (47 Shore A), low 300 % modulus (2.4 MPa), and high melt index (22 g/10 min at 230 °C, 5 kg) [53]. It has a relatively low dielectric constant but a large loss tangent (ε_r = 2.3 and tanδ = 0.07 at 3.5 GHz) [52]. However, the free space in the foam structure is filled with air, which reduces the effective loss [52].

In this chapter, experiments were performed to fabricate SEBS foams using solution casting of polymer into packed bed of water soluble porogen. The goal of this experiment is to produce elastomer foams quickly in arbitrary shapes for use in reconfigurable antenna components and soft robotics applications.

The expectation with this experiment is that the individual grains within the packed bed of porogens will remain in contact with each other after the polymer has been cast over top. It is anticipated that thin films of polymer will exist between the grains. However, during an ultrasonication step to remove the porogens, the expectation is that the local pressures and temperatures imparted on the foams at those locations will be enough to rupture them, producing an open-celled foam.

A major benefit to this method is that the porogens can be recrystallized after being dissolved, the toluene can be captured and reused, and the SEBS foam can be redissolved at the end of its life, minimizing its impact to the environment.

3.2 Experimental

SEBS foams were produced using a solution casting method where SEBS (Kraton G1657 M, Kraton Corporation, USA) was dissolved in a solution of toluene (Fisher Scientific, Canada), after

which the solution was mixed with one of several porogens and allowed to cure by passive solvent evaporation. For detailed properties of the polymers and porogens used, see Appendix A.

Two water-soluble porogens were selected for this experiment, due to their low cost and abundance:

1. sodium chloride (NaCl), in the form of iodized table salt. Table salt is NaCl with additions of potassium iodide, sucrose, and calcium silicate (anti-caking agent). In water, NaCl dissociates completely into its corresponding ions.

monosodium glutamate (MSG). This is typically used as a culinary flavour enhancing agent, and is typically sold as a monohydrate. Similar to NaCl, MSG dissociates in water into Na^+ and the glutamate ion.For each experiment, at 10 vol% solution of SEBS in toluene was prepared. 1.06 g of SEBS was dissolved in 10 mL of toluene (in a beaker and then stirred using a glass rod until the solution became visually homogeneous and transparent.

For experiments using NaCl (Windsor, Canada) or MSG (Lucky99, Canada), six aluminum sample boats were loosely loaded with porogens to prepare samples with 60 vol% and 70 vol% of porogen. For the NaCl porogen, the boats were loaded with 3.76 g and 7.09 g of NaCl for 60 vol% and 70 vol%, respectively. Both coarse table salt, and powdered NaCl were used for experiments. Powdered NaCl was produced by pulverizing coarse table salt in a coffee grinder for 30 seconds. The coarse table salt had a cubic structure with an edge length of approximately 200-600 μm, as shown below in Figure 4. The MSG had a structure made of clusters of acicular pillars, as shown below in Figure 5. The MSG particles had a length of approximately 1-2 mm and a width of 0.5-1.5 mm. For the MSG porogen, 2.73 g and 5.57 g each were used for 60 vol% and 70 vol% loading, respectively.

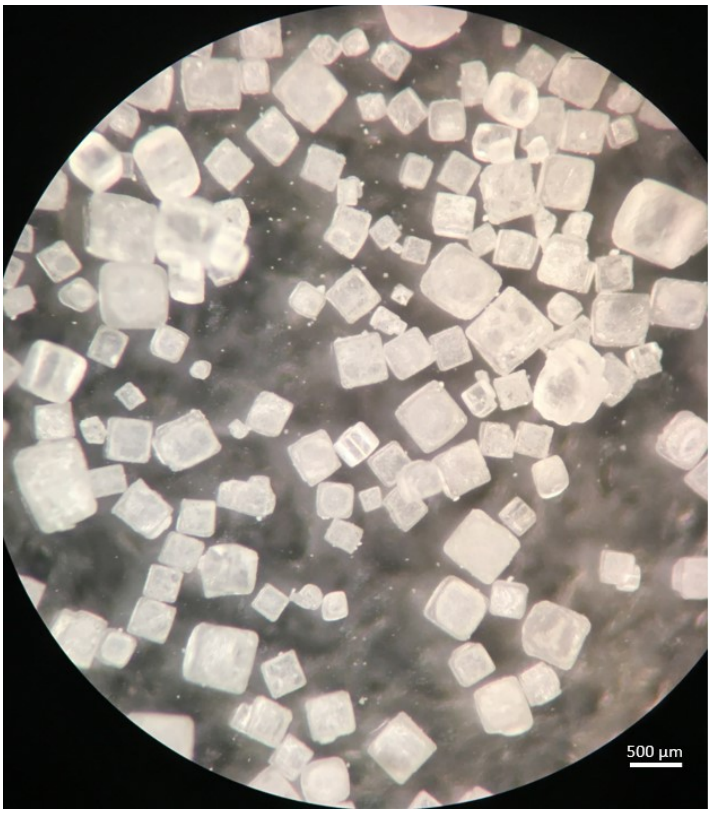

Figure 4. Optical microscopy image of NaCl crystals.

Figure 5. Optical microscopy image of MSG crystals.

After each boat had been loaded with porogen, the SEBS solution was poured over top of the loaded porogens, and gently mixed with a glass stir rod to ensure that the solution and porogen was thoroughly mixed. A thin layer of porogen was added to the top of each boat to prevent a continuous film from forming on the top of the sample boat. The loaded boats were then placed in an ultrasonic water bath for 1 hour, and then placed under a fume hood for 16 hours to evaporate off the toluene.

The samples were then removed from the aluminum boats and were placed in beakers containing 150 mL of deionized water. The samples in the beakers were then sonicated for 1 hour, flipped over, and then sonicated for 1 additional hour, replacing the water after each 1 hour cycle. Residual water was removed from the samples by placing the samples in an oven at 100 °C for 2 hours.

The samples were then allowed to cool to ambient temperature and sectioned into 5 mm x 10 mm samples for tensile testing and 5 mm x 5 mm samples for characterization via SEM. The

thicknesses of the porogen-loaded samples were always greater than the thickness of the control samples without porogen, as shown below in Table 2.

Table 2. Dimensions of foam samples for characterization.

Sample	Width [mm]	Length [mm]	Thickness [mm]	Mass [g]
SEBS	4.45	10.03	1.01	0.03
SEBS/MSG	5.89	11.60	2.29	0.04
SEBS/NaCl (Coarse)	5.07	10.61	2.47	0.01

The samples were then held at one end, parallel to a tape measure, and then the samples were pulled alongside the tape measure until the sample failed. The elongation was then recorded.

In experiments using glucose as a porogen, 10 mL of a 10 vol% solution of SEBS in toluene was prepared, as above. A sugar cube with sides of approximately 12 mm was placed inside a 50 mL glass beaker, and the SEBS solution was carefully poured over top of the sugar cube. The saturated cube was then left for 24 hours in a fume hood at ambient temperature for the toluene to evaporate. The foam was then sonicated for two cycles of 1 hour, with the water being replaced after each cycle. The cube was then manually squeezed to remove excess water, and then left overnight in a fume hood to dry.

The dried foam sample was then immersed in a beaker of olive oil until saturated to test its absorptive properties.

3.3 Results and Discussion

3.3.1 SEBS with NaCl as a Porogen

When NaCl was used as a porogen, yellowing was an issue with both coarse and powdered NaCl. Initially, this was thought to be due to oxidation of the polymer via stilbene formation due to thermal degradation of contained antioxidants [54]–[56], but this was not the case in samples prepared with MSG, which suggests either the NaCl or one of its additives or contaminants. The chemical mechanism of yellowing is beyond the scope of this work. In the samples with coarse

NaCl, impurities in the porogen due to its applicability for consumer use, may be the cause for the yellowing reaction. The foam produced with powdered NaCl was not able to have all of the NaCl removed, and produced a brittle, fragile material.

As was expected, the elongation to failure of the porous samples compared to the solid samples decreased significantly. However, the mechanical strength decreased so significantly in the SEBS/NaCl samples that they failed almost immediately after applying force.

SEM images were taken of the sample, as shown in Figures 6-8, below. From the images, it is evident that not all of the NaCl had been dissolved and removed from the composite. NaCl can be seen embedded in the fibres and the pore size is very large and irregular in distribution.

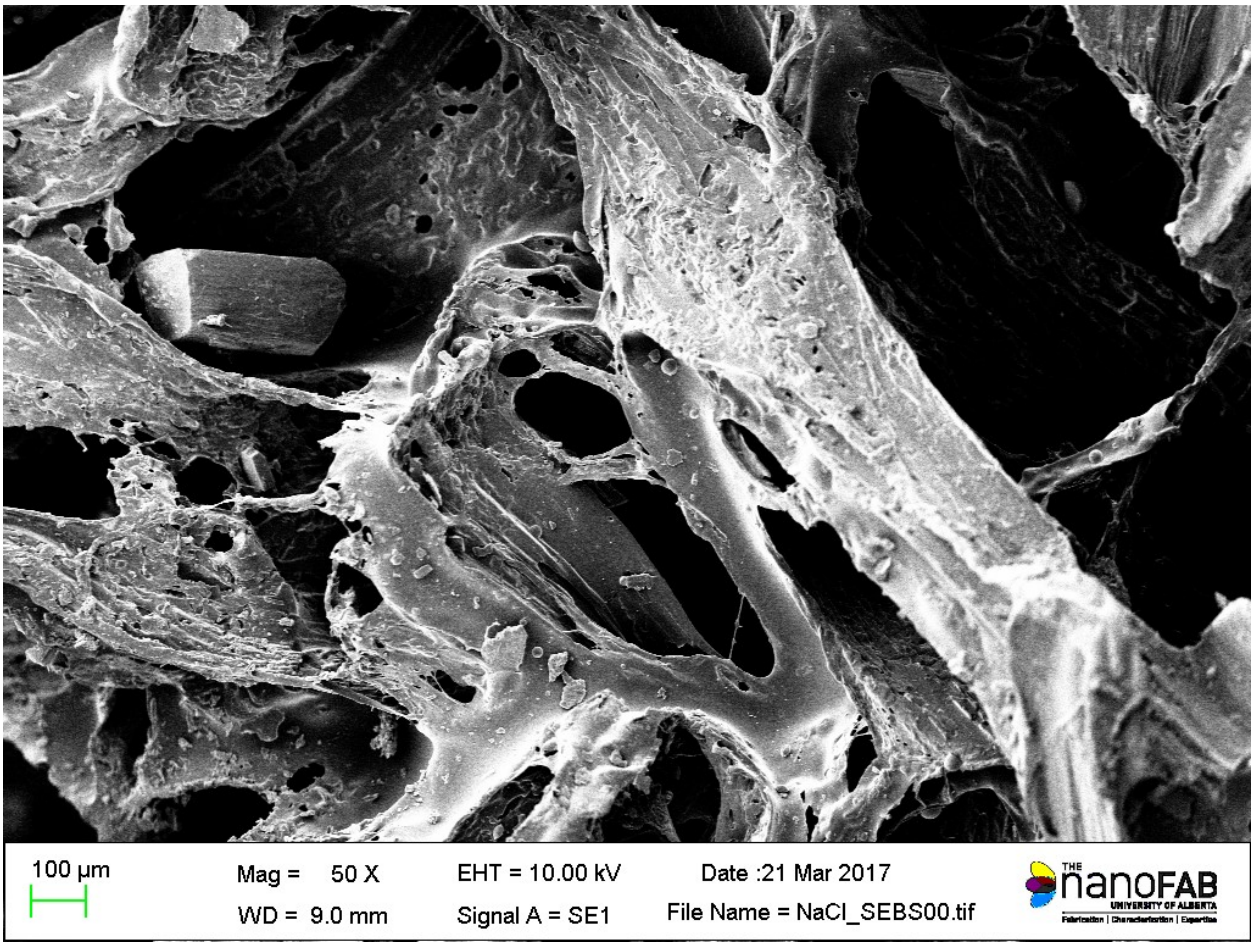

Figure 6. SEM image of SEBS/NaCl foam at 50 X magnification. A large undissolved NaCl crystal is visible in the top left of the image. Smaller NaCl pieces are shown strewn around the image.

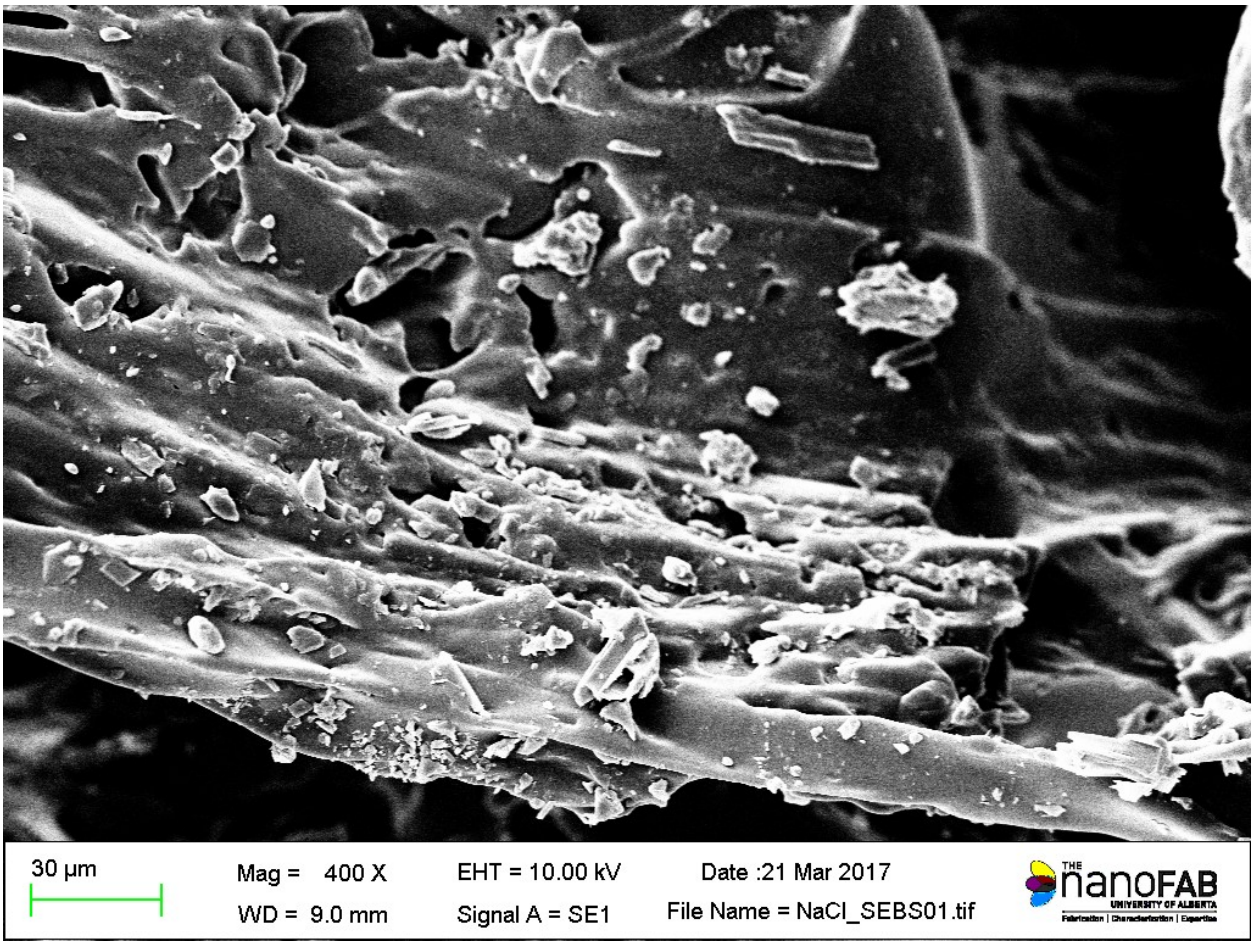

Figure 7. SEM image of SEBS/NaCl foam at 400 X magnification. Small undissolved flecks of NaCl are visible embedded in the SEBS fibres.

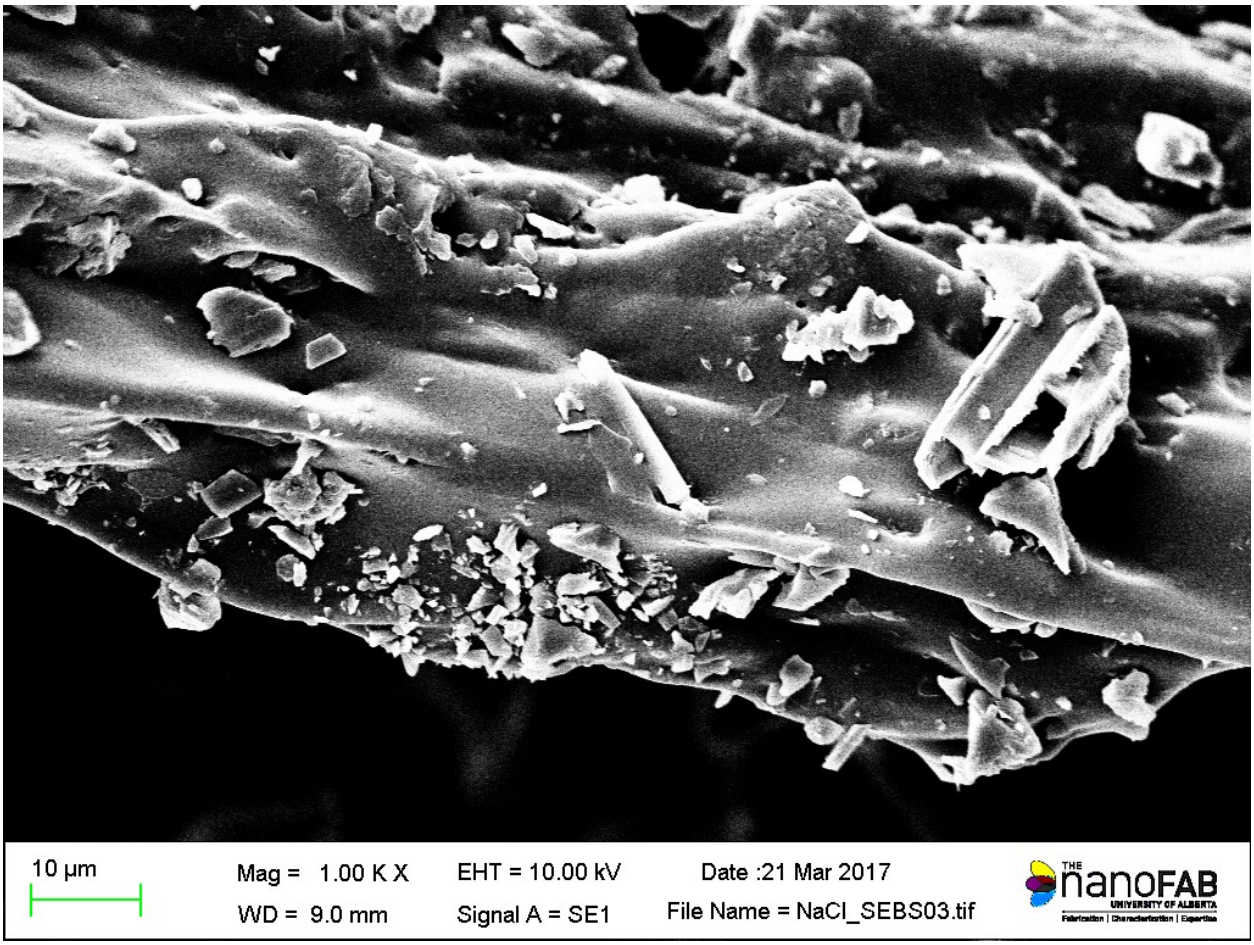

Figure 8. SEM image of SEBS/NaCl foam at 1000 X magnification. Small undissolved flecks of NaCl are visible embedded in the SEBS fibres.

3.3.2 SEBS with Glucose as a Porogen

The resultant foam from the experiment exhibited a visually uniform open-cell foam structure in the shape of the sugar cube template upon which it was cast. The foam exhibited excellent absorptive properties with olive oil, but immediately lost the required mechanical strength to return to its original shape, and collapsed into a gel.

3.3.3 SEBS with MSG as a Porogen

The foam produced from an MSG porogen had smaller pores than the other foams, was soft to the touch, and produced an opaque white foam with no yellow discoloration. These foams exhibited a decrease in elongation of 50 % compared to the bulk sample. As shown in the SEM images in

Figures 9-11 below, the overall pore size of the foam is representative of the acicular shape of the MSG crystals, but there also exist smaller domains on the order 1 -20 µm of where the pore size becomes more regular with an average pore size of 5 µm.

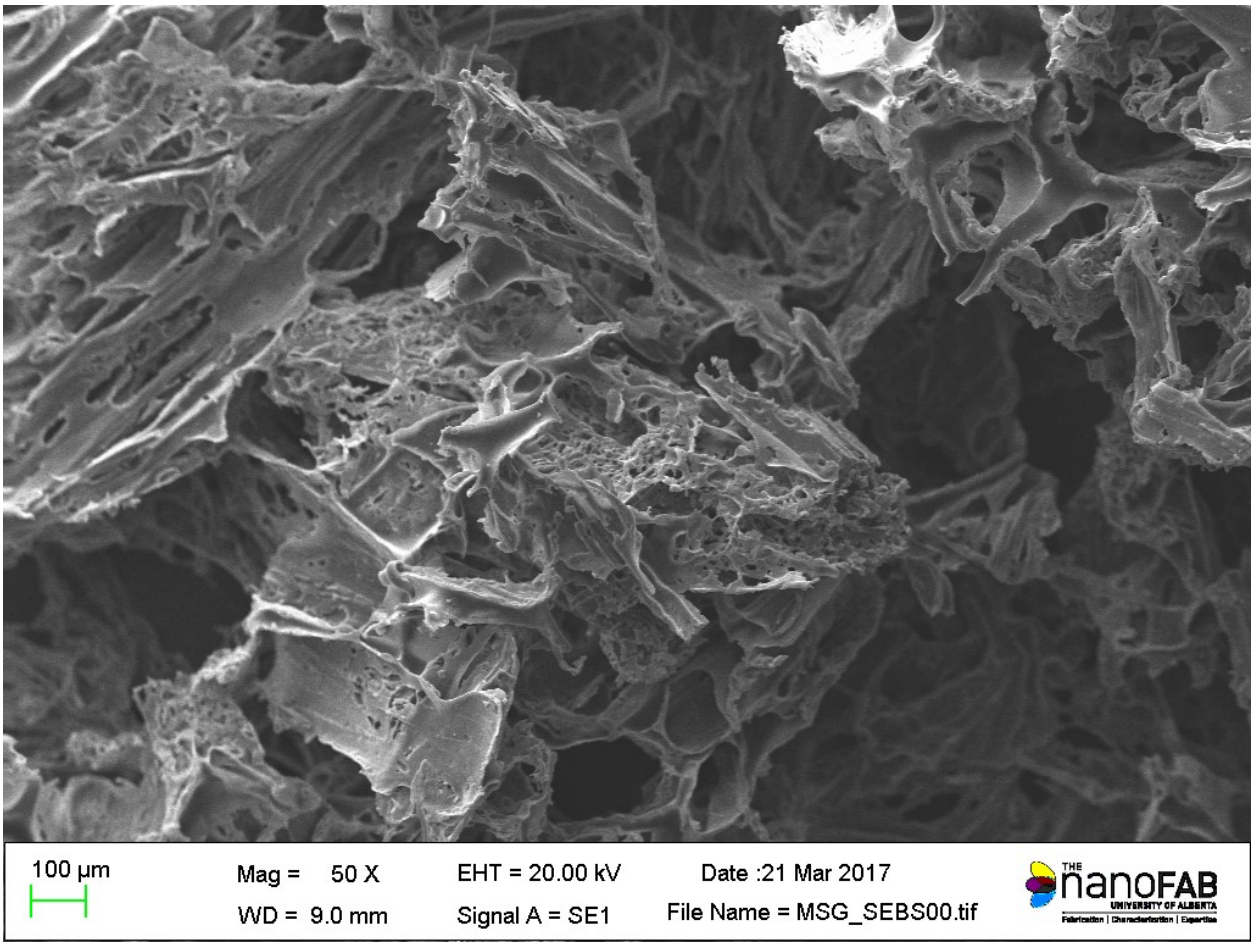

Figure 9. SEM image of SEBS/MSG foam at 50 X magnification.

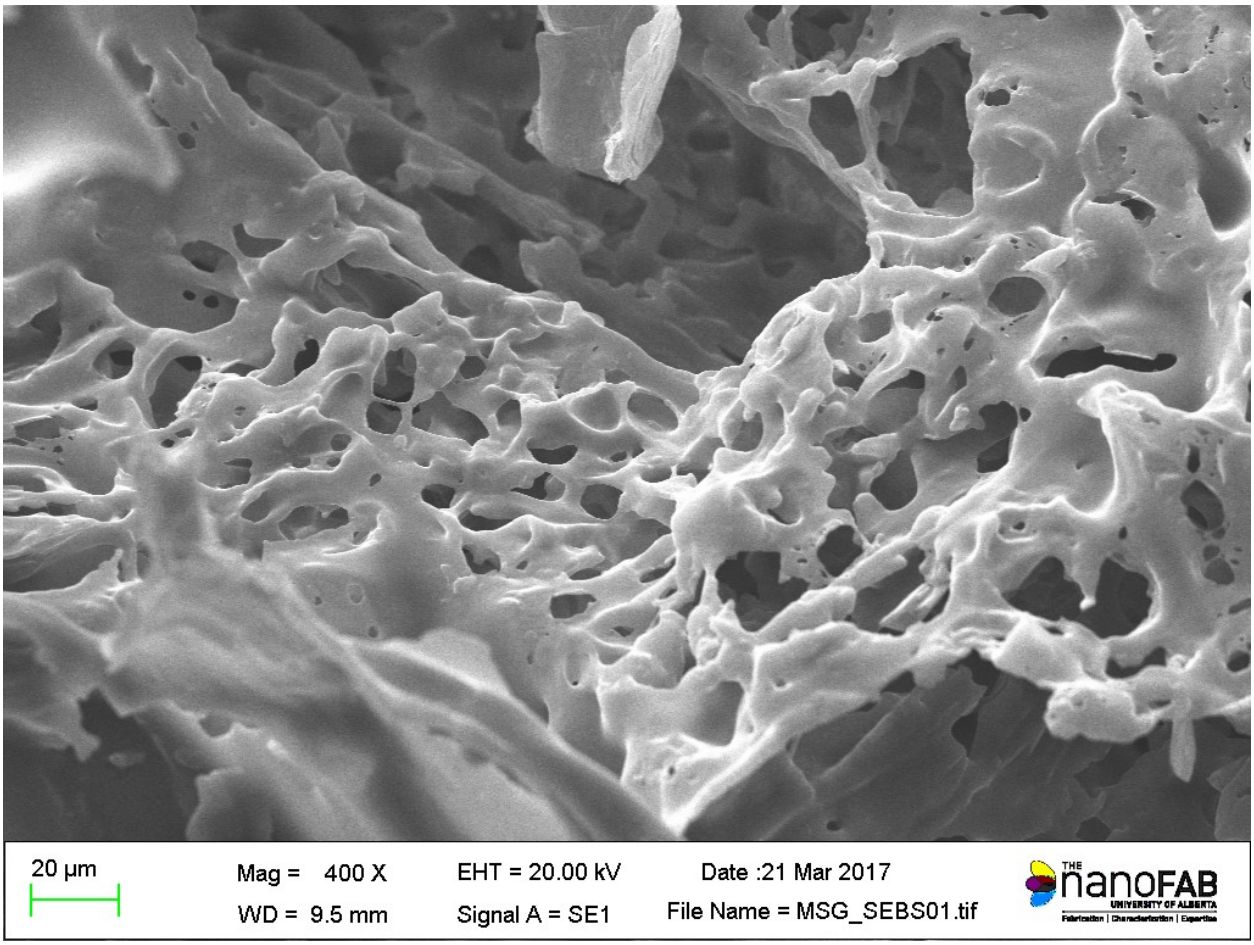

Figure 10. SEM image of SEBS/MSG foam at 400 X magnification. The pore size becomes more regular at smaller domain lengths.

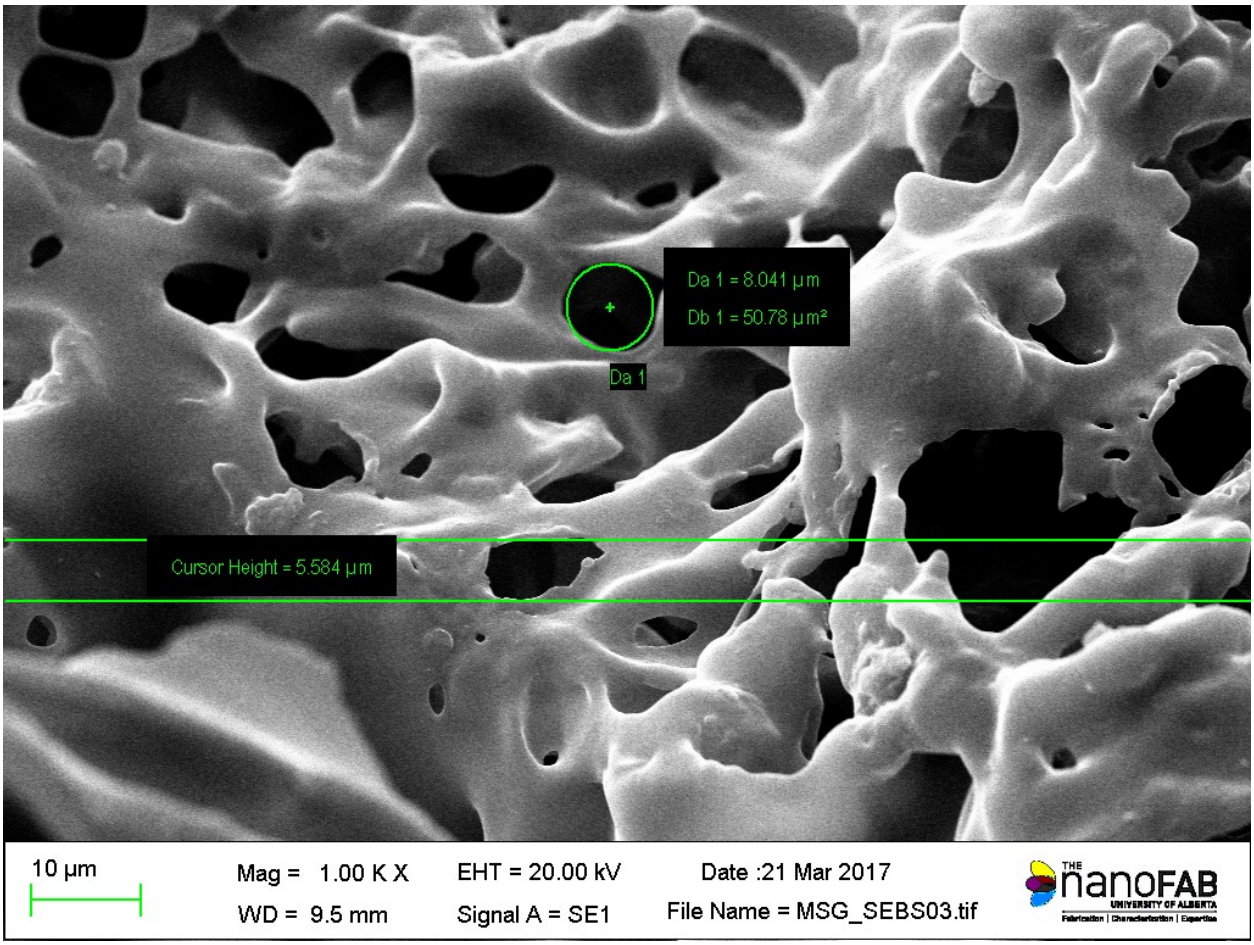

Figure 11. SEM image of SEBS/MSG foam at 1000 X magnification, showing measurments of pore size.

3.4 Conclusion and Future Work

This work began as an investigation into the production of SEBS foams using water-soluble templates coupled with solution casting of the polymer. Foams were successfully produced using a low-cost, safe, and facile method using table salt and MSG as porogens in a SEBS foam. SEM analysis showed incomplete porogen dissolution in the table salt foam, while the porogen was completely removed in the MSG foam. A foam using a glucose template was also successfully produced, but it was not characterized beyond its oleophilicity, which was very high. Although two porogens were used in this work, in theory, these foams can be fabricated with any solution-processable thermoplastic and compatible water-soluble salt. Although the mechanical properties of the foams were significantly lower than that of a film of SEBS, their absorbance to oils and

open space in the foam structure showed favourable results. There is potential for this work to continue along similar lines with the following considerations to be taken:

- MSG is a better water-soluble porogen for SEBS than table salt due to the difficulty in completely removing the table salt from the material.
- The MSG crystals used were too large to use appropriately and should be crushed in future experiments.
- Other methods for templating should be investigated, such as compression molding the polymer around a template.
- The potential exists for SEBS to be mixed with a water-soluble porogen as an extruded filament to be used in an additive manufacturing application. Several difficulties would need to be overcome, such as offgassing of steam from the MSG at typical printing temperatures, and clogging/increased wear in the nozzle.

Chapter 4: Lost Foam Casting from Additively Manufactured Foam

4.1 Lost Foam Casting

Lost foam casting is a metal casting process in which a consumable pattern made from an expanded foam pattern, typically EPS, expanded PMMA (EPMMA), or a copolymer made from both [57] is inserted into a sand mold and molten metal is then poured into the mold, vapourizing the foam pattern in the process. In the process, the final shape of the casting is currently produced by one or more of the three following processes: 1. Expanding PS beads in an expansion vessel using steam, 2. Using a heated nichrome wire to cut a foam billet into the proper shape, and 3. Machining the desired shape from a billet of foam [58]–[60]. The ease of machining foam using a hot wire or traditional machine tools is advantageous for jobbing foundries due to the relatively low tooling and material costs required. Complex foam patterns are typically machined in several parts and then glued together. Further benefits to lost foam casting are that the castings do not require drafts or cores, which leads to increased design freedom for the casting designer.

Once the foam pattern is fully machined and assembled, a refractory coating that acts as a barrier and release agent between the casting and sand to prevent sand incorporating into the casting during pouring is applied to all surfaces of the foam pattern. The coating is also permeable to gases that are generated when the foam pattern is vapourized from the molten metal front. The coated foam pattern is then lowered into a steel box, and sand fills the box and cavities via vibration. Both unbonded or bonded sand can be used. If unbonded sand is used, the process is called “Lost Foam”, and if the sand is bonded with a chemical binder, the process is called “Full Mold” [61]. Lost Foam casting can be further aided by pulling a vacuum on the mold, jamming the sand particles together, causing them to hold the mold shape. In this process, only blind risers may be used, since the combustion of thermoplastic foams produces significant amounts of polycyclic aromatic hydrocarbons (PAH) and soot, as well as CO_2, CO, and NO_x [62]. By using blind risers, the vapourized products are exposed to less atmospheric oxygen, resulting in a reduction in combustion products in the mold.

When the molten metal is poured into the foam mold, the thermal energy imparted into the foam is sufficient to cause it to vapourize, producing a gaseous front of styrene and its thermal decomposition products directly in front of the molten metal head. Warner et al. proposed a kinetic zone, which is the region between the molten metal front and the liquifying and vapourizing polymer [26], [63]–[65]. Rather than combust, the gaseous thermal decomposition products diffuse through the refractory coating into the surrounding sand, as shown in Figure 12, below.

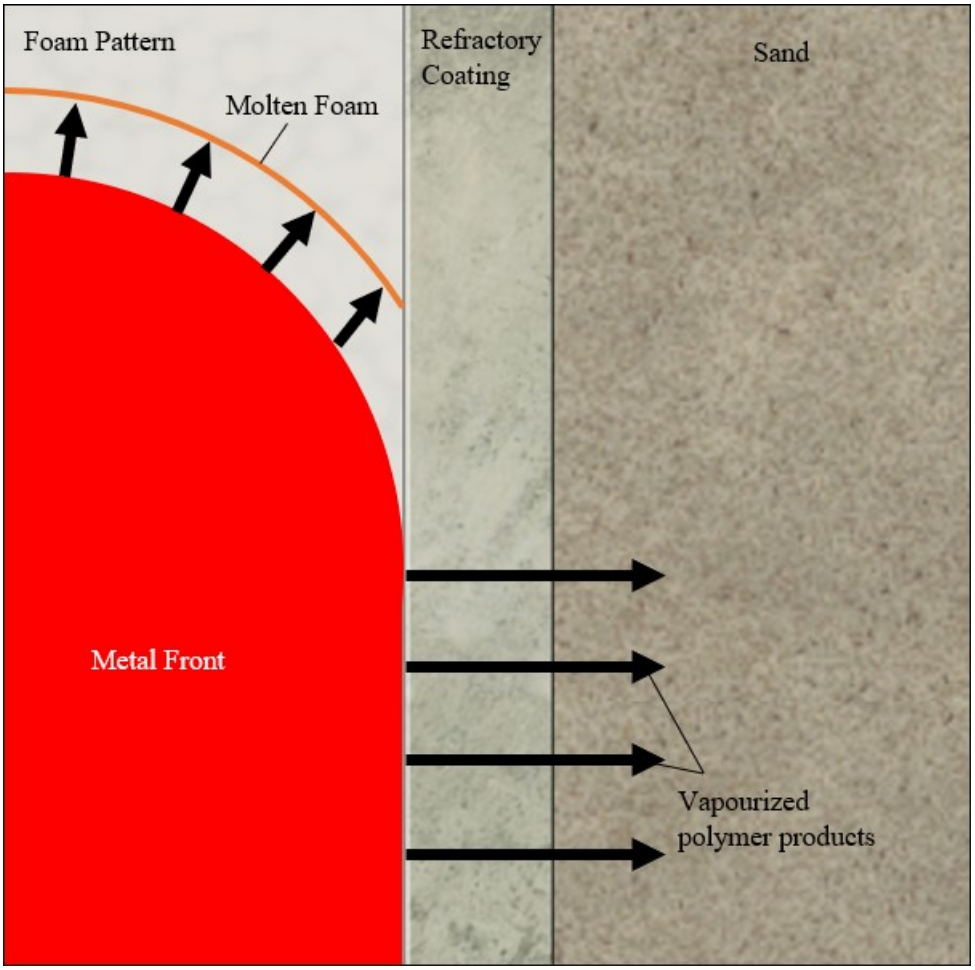

Figure 12. Schematic showing gaseous EPS decomposition products diffusing through the refractory coating into the surrounding sand.

The metal flow rate in lost foam casting tends to be lower than in traditional sand casting, due to the back pressure experienced by the metal front caused by the gaseous products formed, and due to the reduction in fluidity of the metal caused by the transfer of some thermal energy from the melt to the foam. Liu et al. modeled the metal front velocity of 319 aluminum in EPS foam by

performing an energy balance between the energy given from the molten metal front and the energy required to liquify, vapourize, and depolymerize the foam [65]. Equation 2 describes the heat transfer rate from the liquid metal front into the kinetic zone using Newton's Law of Cooling, where q_{s} is the heat transfer rate, h is the heat transfer coefficient at the metal front, T_{s} and T_{z} are the temperatures of the metal front and kinetic zone, respectively, and A_c is the cross-sectional area of the metal front.

$$q_{\mathrm{s}} = h(T_{\mathrm{s}} - T_{\mathrm{z}})A_{\mathrm{c}} \qquad \text{Eq. 2}$$

Equation 3 describes the energy required to reduce the foam into its monomers and thermal decomposition products, where q_{f} is the surface heat flux to the foam, c_{p} is the specific heat of the foam, Q_{liq}, Q_{vap}, and Q_{depoly} are the latent heats of fusion, vapourization, and depolymerization, respectively.

$$q_{\mathrm{f}} = \dot{m}c_{\mathrm{p}}(T_{\mathrm{s}} - T_{\mathrm{z}}) + \dot{m}Q_{\mathrm{liq}} + \dot{m}Q_{\mathrm{vap}} + \dot{m}Q_{\mathrm{depoly}} \qquad \text{Eq. 3}$$

The mass flow rate is defined as

$$\dot{m} = \rho A_{\mathrm{c}} V_{\mathrm{adv}} \qquad \text{Eq. 4}$$

Where ρ is the foam density and V_{adv} is the velocity of the advancing metal front. After setting q_{s} and q_{f} equal to each other and rearranging for V_{adv}, the equation for the metal front advancing velocity becomes

$$V_{\mathrm{adv}} = \frac{h(T_{\mathrm{s}} - T_{\mathrm{z}})}{\rho\left(c_{\mathrm{p}}(T_{\mathrm{s}} - T_{\mathrm{z}}) + Q_{\mathrm{liq}} + Q_{\mathrm{vap}} + Q_{\mathrm{depoly}}\right)} \qquad \text{Eq. 5}$$

Experiments by Liu et al. have shown that the heat transfer coefficient is a function of foam density, coating thickness, metal front velocity, and time, with the heat transfer coefficient increasing over time[63], [64].

4.2 PLA Foam

Polylactic acid (PLA) is a thermoplastic biopolymer created from the polymerization of lactide or lactic acid (2-hydroxy propionic acid). It is a thermoplastic polyester that has seen increased usage commercially since the 1980s due to its availability to be produced from fermented byproducts of starchy plants (ex. Corn, cassava, sugar cane) [66]. PLA is also compostable under specialized conditions and can be recycled back into the monomer form to produce new PLA.

PLA is used primarily in the packaging industry, but also sees applications in the medical industry, where biocompatible polymers are required [67]. As well, with the expiration of several patents pertaining to FDM printing, PLA has seen significant usage in the consumer 3D printing industry due to its low cost, low melting point, favourable properties for many consumer products, and biodegradeability.

PLA foams are being thoroughly investigated for their potential use as a replacement for petroleum-based foams, such as EPS. The ability to use PLA foams in place of EPS provides several advantages, not least being the inherent abundance of waste material required to produce the polymer, the reduced energy requirements to produce an equivalent quantity of PLA compared to petroleum-based polymers [68]. PLA foams already see use in food packaging applications (ex. Clamshell packaging and egg cartons).

Unlike the majority of thermoplastic polymers PLA is not solution processable, hence a PLA foam must be melt-processed [12]. MSG has a melting point of 232 °C, which is slightly above the processing temperature of PLA. For an initial experiment, MSG (Lucky99, Canada), dextrose (Fisher Scientific, Canada), and fine NaCl (Windsor, Canada) were used as porogens. 5 mm long, 1.75 mm diameter pieces of PLA were cut from a spool and placed in an aluminum dish. A mass of porogen was added to the aluminum boat in a 50 wt% fraction. The dish was then placed in an oven at 210 °C for 1 hour.

Due to a lack of agitation of the polymer in the oven, the shear thinning characteristics of the PLA prevent proper mixing of the porogen and PLA. In order to avoid this, the samples were removed after 30 minutes and stirred with a Teflon stir rod, before placing them back in the oven for an additional 30 minutes. After 1 hour, the samples were removed from the oven and placed in an ultrasonic bath in water for 1 hour.

The results of the samples were generally unfavourable with non-uniform distribution of the porogens and a difficulty in removing the porogens from the samples. The results are shown below in Figures 13-15.

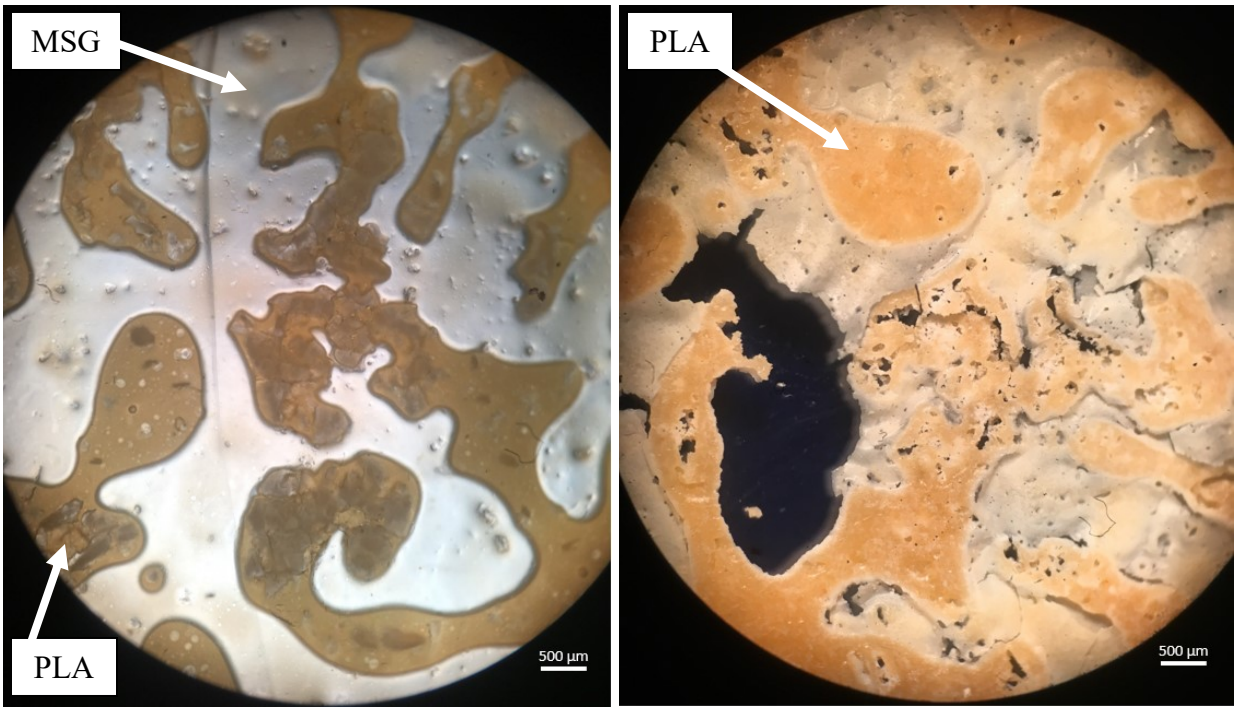

Figure 13. PLA foams produced with MSG. (a) before sonication, (b) after sonication.

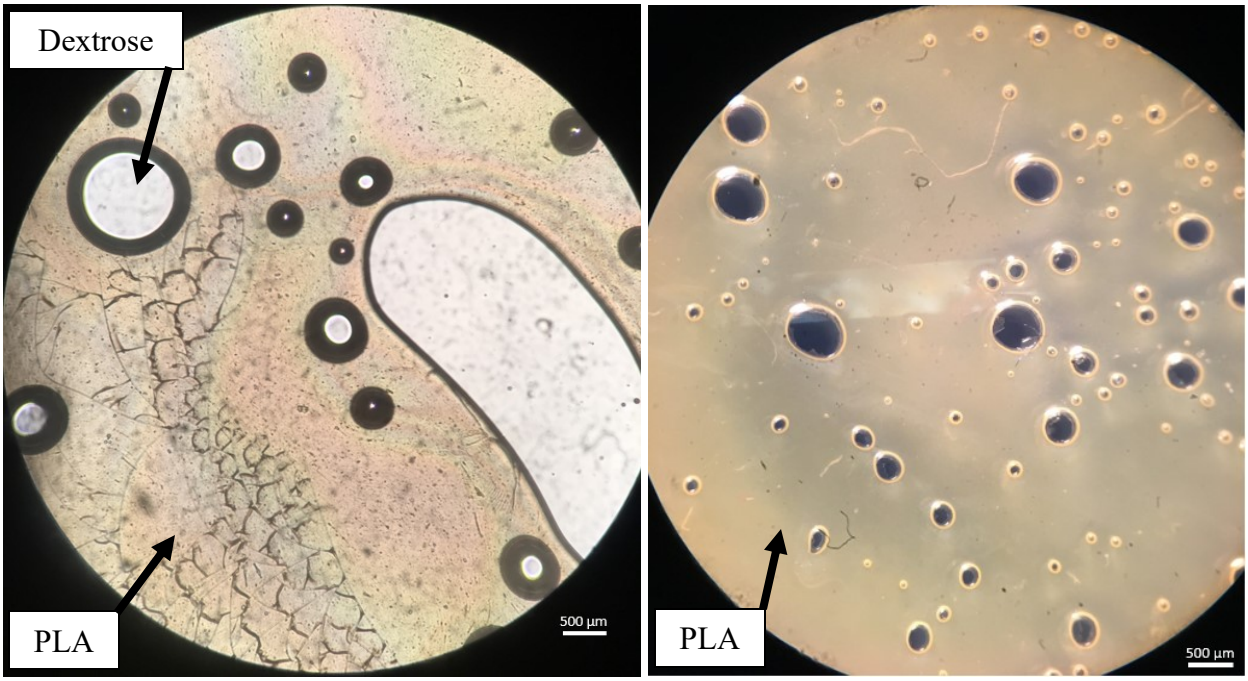

Figure 14. PLA foams produced with dextrose. (a) Before sonication, (b) After Sonication.

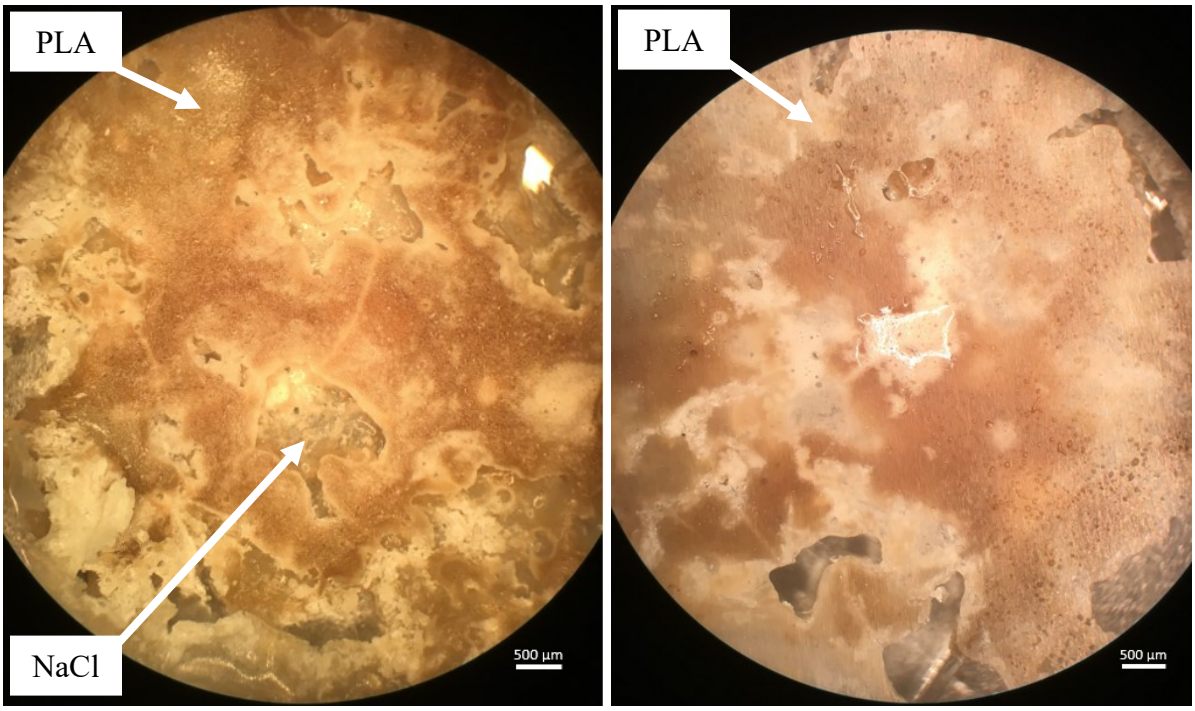

Figure 15. PLA foams produced with NaCl. (a) before sonication, (b) after sonication.

4.3 Lost PLA Foam Casting

To test the applicability of foamed PLA as a consumable pattern for metal casting, a PLA filament containing a foaming agent called LW-PLA (ColorFabb, Netherlands) was used to print several patterns that were then cast in ASTM A48 grey iron. The LW designation stands for "light weight". A CR-10 3D printer (Creality, China) was used to print all of the parts in this section. The printer parameters are shown in Table 3, below.

Table 3. CR-10 Parameters for Printing LW-PLA

Bed Adhesion	Bed Temperature [°C]	Nozzle Opening [mm]	Enclosure	Filament Drive
Painter's Mate Blue Tape	60	0.4	None	Bowden

The LW-PLA was calibrated as per the following procedure:

1. Four cubic shells were printed between 230 °C – 260 °C at 25 mm/s with a 0.2 mm layer height and their wall thickness was measured. The print with the greatest wall thickness exhibited the most expansion, and that temperature was used in further calibrations. Figure 16 shows the parameters used for the test shells and their resultant wall thicknesses. 260 °C was determined to produce the greatest amount of expansion.

2. The flow rate multiplier in the slicer settings was then reduced to produce a wall thickness equal to that of the nozzle opening. The flow rate multiplier is a dimensionless number that affects the extrusion rate. The multiplier setting for 260 °C was determined to be 0.33.

Figure 16. LW-PLA Calibration Shells.

In order to validate the printing parameters, several test structures were printed that contained holes, text, bridges, high aspect ratio structures, and varying degrees of overhanging structures. The test structures were freely available from Thingiverse, as shown in Figure 17, below [69], [70]. The bust of Athena of Velletri was printed with 1.2 mm thick walls and a 10 % lightning infill to maximize the amount of empty space inside the print. The Mini All-in-One Printer Test showed that although the filament printed well structurally at a variety of overhangs, bridges, holes, and towers, there was a lack in detail sharpness on small features. As well, branches of filament form over the course of the print due to errant expanded foam emerging from the nozzle tip contacting the walls and other branches. On larger prints such as the Athena bust, they are easily removed using flush cutters or pinching them off by hand. On smaller, more finely-detailed prints such as the All-in-One Printer Test, the branches connect between features, increasing the amount of post-processing required to remove them, as well as increasing the risk of failed prints due to nozzle collisions with the branches. It was determined that although at 260 °C, the maximum

amount of expansion occurs, print quality is degraded, where significant stringing, sagging, and loss of feature resolution occurs. At 250 °C, stringing remained a problem, but the expansion was comparable enough to produce components at an extrusion multiplier of 0.35.

Figure 17. LW-PLA Test Structures. Top: Athena of Velletri. Bottom: Mini All-in-One Printer Test.

Initially, two patterns were printed. As shown in Figures 18-21, below. The first pattern (Figures 18-19) was designed to both test the resolution capabilities of the casting process, as well as print structures that are otherwise prohibitively difficult to produce in conventional sand molding processes, such as cast-in threads, overhanging structures, internal channels, and shapes that are swept along a profile. The existing sprue was removed and replaced with a larger EPS sprue in order to accommodate enough volume of the molten metal.

The second pattern (Figures 20-21) was a scaled-down version of a medieval cannon, printed in 5 parts – the main cannon body, 2 trunnions, the back end of the cannon including the knob, and a 2-way split sprue. All of the wall thicknesses were 1.2 mm and the parts were printed with a 10 % grid infill. In a typical sand-casting operation, this would be difficult to mold with the trunnions cast integral to the cannon.

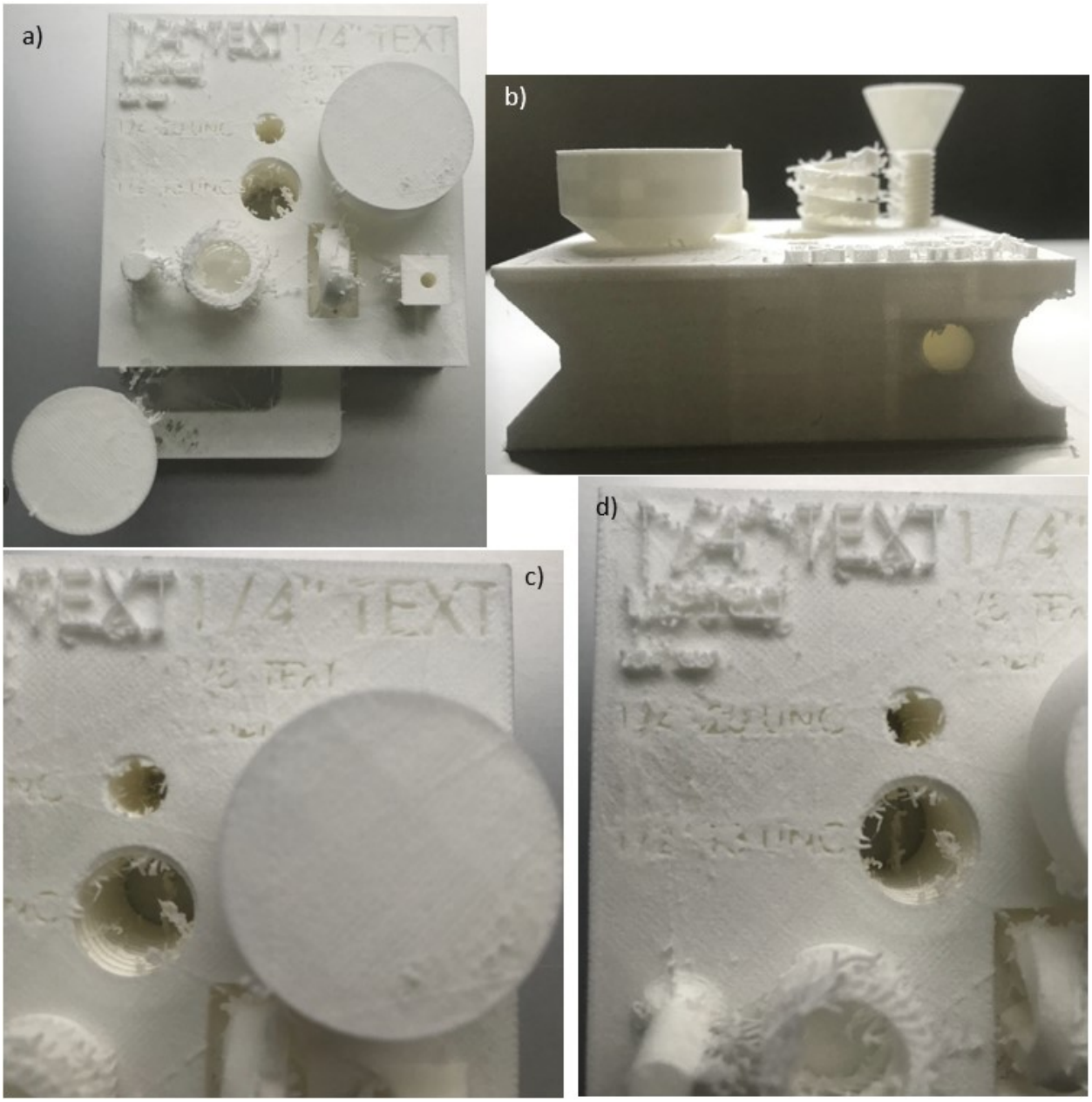

Figure 18. Test pattern after printing. Note the severe branching on high detail features.

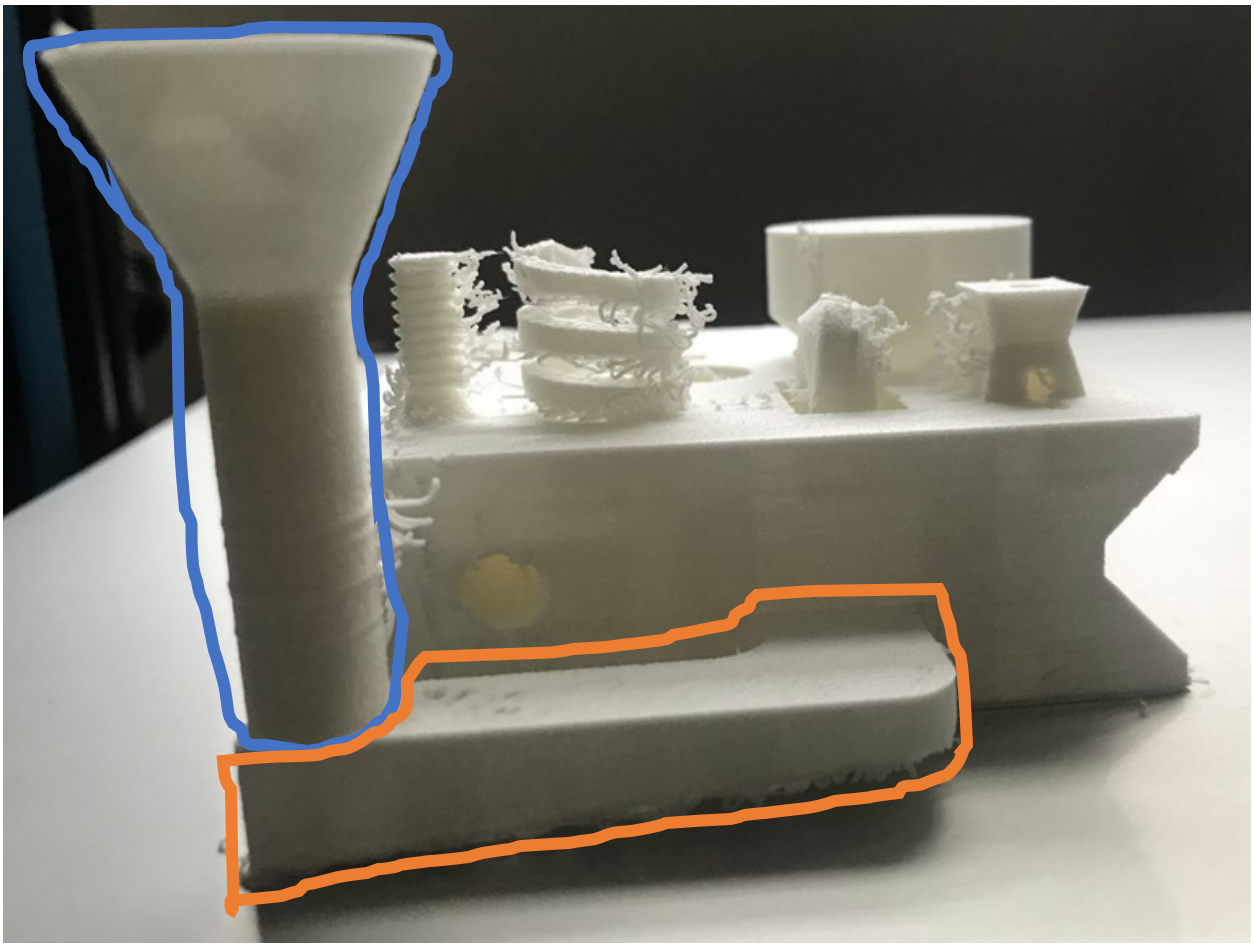

Figure 19. Side view of the test pattern showing the downsprue (outlined in blue) and the runner (outlined in orange). The printed downsprue was replaced with a piece of Type II EPS in order to make filling easier.

Figure 20. Expendable medieval cannon pattern. Left: before assembly. Right: partially assembled. The split sprue is shown at the bottom right.

Figure 21. Fully assembled medieval cannon pattern.

The pieces were assembled using BP-8003 (Polytek, USA), a thixotropic adhesive composed of latex dispersed in water. Once the adhesive had dried, the patterns were coated in Holcote 3100 (Vesuvius, UK), a zirconia-water slurry that dries as a refractory coating. It changes colour from green to yellow as it dries as visual aid, shown below in Figures 22 and 23.

Figure 22. Left: Test pattern coated with Holcote 3100. Right: Test pattern molded in sand.

Figure 23. Left: Cannon pattern coated with Holcote 3100. Right: Cannon pattern molded in sand.

After the coating had dried, two additional coats were applied to ensure that metal penetration through the mold would not occur. Once the final coat had dried, the coated patterns were molded in sand molds using no-bake sand. A pouring cup made from sand was placed on top of each mold, and grey iron was poured into the mold at 1288°C. Due to either retained moisture or poor coating permeability, the first metal to enter the mold was promptly ejected out of the top of the pouring cup, resulting in an incomplete fill, as shown in Figures 24 and 25. Despite the incomplete pour, the resolution of the casting matched that of the pattern, with the layer lines easily visible. Future work is required to determine the optimum wall thickness that allows for quick polymer vapourization while also retaining enough structural strength to prevent pattern collapse during handling or application of the zirconia slurry.

Figure 24. Test pattern casting. The EPS downsprue and the LW-PLA runner are visible.

Figure 25. Medieval cannon casting. The level of detail replication is high, with layer lines visible.

4.4 Additively Manufactured LLDPE Foam

Expanded linear low-density polyethylene (LLDPE) was produced via extrusion through a FDM 3D printer nozzle. LLDPE is a thermoplastic with a short chain length and limited branching, resulting a relatively low density (0.91 g/cm^3) compared to many other thermoplastic polymers [71]. LLDPE was primarily chosen due to its low density compared with high density polyethylene (HDPE) and for its low melting and ignition temperature [72]. Compared with low density polyethylene (LDPE), LLDPE has a higher crystallinity due to the lower degree of branching, leading to a more rigid polymer without sacrificing the low density desired. For this experiment, a chemical blowing agent was used. Foamazol F60 (Bergen International, USA) was used as a chemical blowing agent. Foamazol is an endothermic blowing agent with a decomposition temperature beginning at 180 °C. LLDPE was provided in the form of 4 mm pellets (Sigma Aldrich, USA). For each trial, 100 g of LLDPE pellets were mixed with the LLDPE in 2 wt% and 3 wt% loadings, and then added to a filament extruder hopper (Wellzoom B desktop filament extruder, China). The temperature of the extruder heater was set to 175 °C, and the control dial in which to control the screw speed was set to maximum, producing an extrusion rate of 1.6 g/minute. The F60-laden LLDPE filament was coiled on a standard filament spool attached to a filament winder (Wellzoom, China).

The resultant filament was fed into a CR-10 v3 (Creality, China) with the following parameters shown in Table 4.

Table 4. CR-10 v3 Parameters for Printing LLDPE Foaming Filament

Bed Adhesion	Bed Temperature [°C]	Nozzle Opening [mm]	Enclosure	Filament Drive
Adhesive-backed polyethylene film	25	0.4	None	Direct Drive

Similarly to the LW-PLA experiment, the LLDPE foam (LLDPE-F) was calibrated as per the following procedure:

1. Four cubic shells were printed between 200 °C – 250 °C at 25 mm/s with a 0.2 mm layer height and their wall thickness was measured. The print with the greatest wall thickness exhibited the most expansion, and that temperature was used in further calibrations. Figure 26 shows the parameters used for the test shells and their resultant wall thicknesses.

2. The flow rate multiplier in the slicer settings was then reduced to produce a wall thickness equal to that of the nozzle opening.

Each of the 4 walls of each sample were measured for their thickness, and their average values are shown in Figure 26, the samples produced with 2 % F60 exhibited increasing expansion as the temperature increased. However, with 3 % F60, the wall thickness decreased at 250 °C, suggesting that the cell walls either recoalesced into a solid structure or the walls collapsed due to a lack of structural integrity at 250 °C.

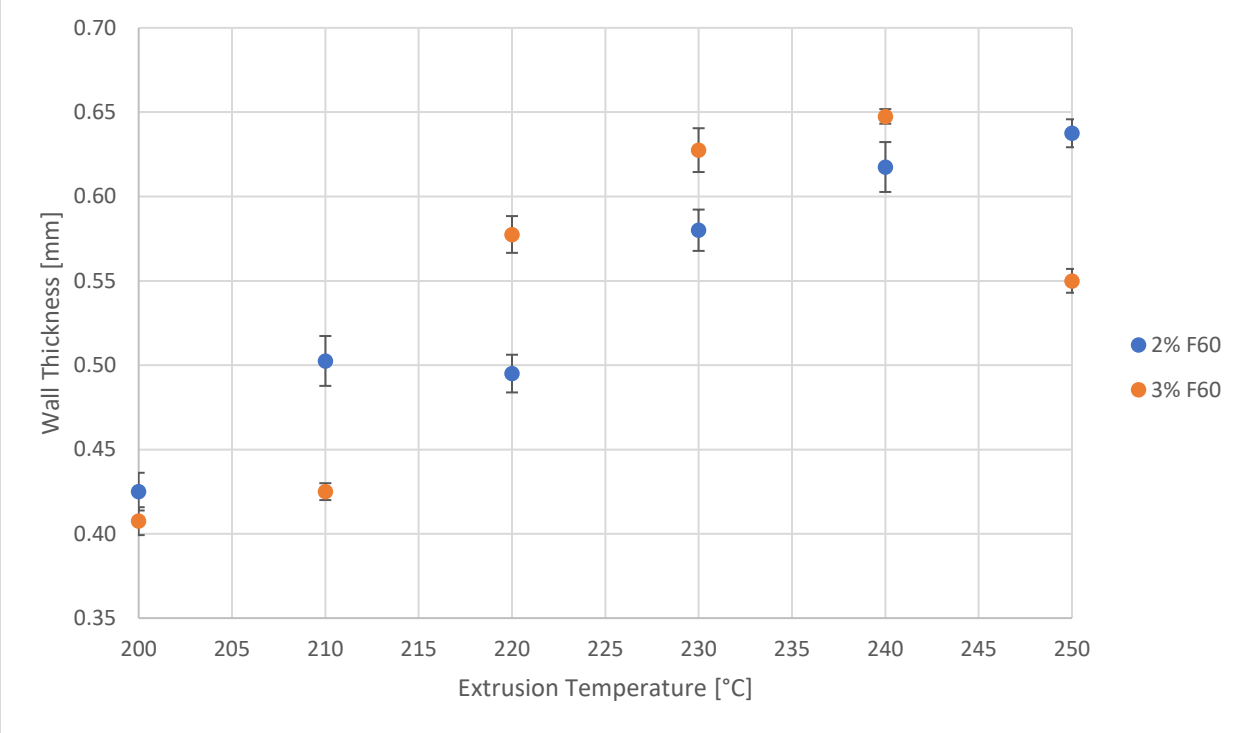

Figure 26. Relationship between extrusion temperature and foaming agent loading for LLDPE foams.

The temperatures at which maximum foaming occurred was 250 °C for 2 % F60 LLDPE-F and 240 °C for 3 % LLDPE-F. The decrease in foamability at higher temperatures is most likely caused by a poor melt strength of the LLDPE, leading to recoalescence of the cellular structure [49]. A wall thickness of 0.40 mm was achieved at a flow rate of 70 % for 2 % F60 LLDPE-F, while 0.40 mm was not achievable with a 3 % F60 loading. At 63 % flow or greater, the wall thickness averaged at 0.43 mm, while at 62 % flow the wall thickness averaged 0.38 mm. Noticeably, the foaming in the LLDPE-F samples was significantly lower than the foaming observed in the LW-PLA discussed in the section 3.3. Images of the test shells are shown below in Figures 27 and 28.

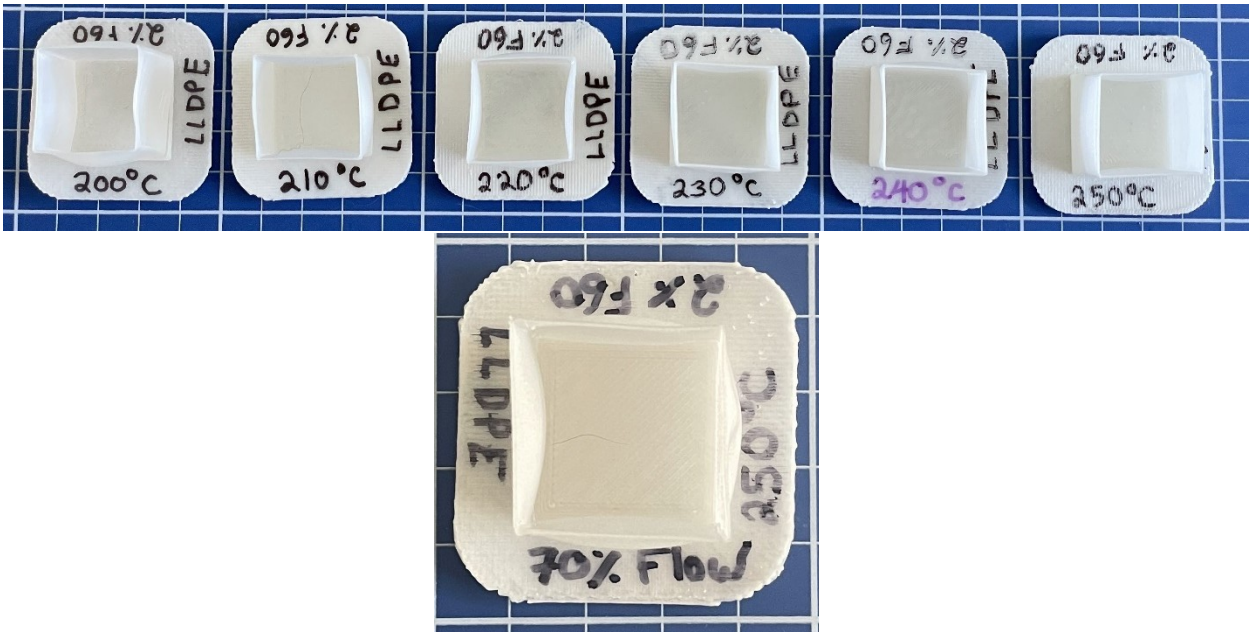

Figure 27. Top: LLDPE-F Test shells at 2 % F60 loading. Bottom: Optimized flow rate to achieve a wall thickness of 0.4 mm.

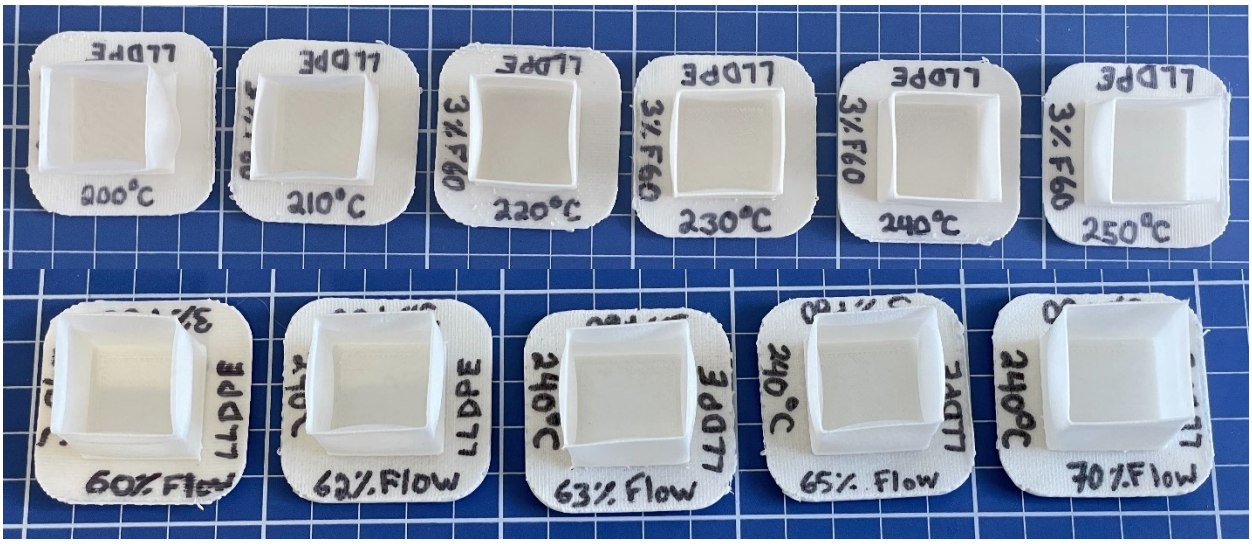

Figure 28. Top: LLDPE-F Test shells at 2 % F60 loading. Bottom: Samples tested at various flow rates to achieve a wall thickness of 0.4 mm.

4.5 Conclusion and Future Work

In this chapter, PLA foams were produced using FDM additive manufacturing in order to produce expendable patterns for metal casting operations. A commercially available PLA that contained a foaming agent that activated above 200 °C was used to print the patterns, and optimal printing parameters for maximum foamability were determined. The 3D printed patterns were prepared according to typical lost foam casting practices and grey iron was poured into the molds.

Although the initial experiments did not produce successful castings, the areas in which metal replicated the pattern showed as-cast surface finishes comparable to those of FDM additively manufactured parts. Potential changes that can be made to address the challenges experienced in this chapter include:

- Determining an optimal wall thickness in which the pattern retains enough structural rigidity to hold its shape during the coating and sand packing processes.
- Holding the coated pattern in a humidity and temperature-controlled environment prior to casting in order to minimize the absorption of atmospheric moisture.
- Designing optimized gating such that the risk of gaseous blowback is mitigated into the sand, rather than back up the sprue.

Besides optimizing the printing parameters and handling of the expendable patterns, future investigations into proper coatings for LLDPE and casting trials for LLDPE foams are required.

Chapter 5: Liquid Metal Reconfigurable Reflector

5.1 Background

Liquid metal-based electronics (LMBE) are devices composed of traditional components such as resistors, capacitors, and inductors, using liquid-state metals to form the conductive medium of the circuit. Colloquially called liquid metals are metals or metal alloys which are in the liquid state at or near room temperature. Liquid metals are able to deform freely while retaining their electrical and thermal conductivities and will conform to the shape of its container. This ability allows for the creation of stretchable electronics, given that the liquid metal can be encapsulated within a liquid-impermeable, stretchable, electrically insulating medium.

Several metals and metal alloys are liquid at room temperature, with mercury (Hg) being ubiquitous in most people's minds. Table 5 below lists several pure metals and metal alloys that exist as liquids at or near room temperature.

Table 5. List of Low-Melting Point Pure Metals and Alloys

Metal/Alloy	**Melting Point [°C]**
Mercury (Hg)	-38.8
Gallium (Ga)	30
Cesium (Cs)	28.5
eGaIn	15.5
Galinstan	-19
NaK	-12.6

Gallium-based alloys are increasingly being investigated for use in LMBE due to their relatively high electrical and thermal conductivities [73], non-toxicity to humans [74], [75], low room temperature vapour pressure [76], and unique processing methods due to a readily forming oxide shell in air [10], [11], [50], [51], [77], [78].Gallium is a transition metal with a relatively low melting point (29.76 °C). This low melting point gives gallium and several of its alloys the ability to be used in the liquid phase at or near room temperature, in which it retains its high electrical and thermal conductivities, reflectivity to electromagnetic radiation, and ability to wet and alloy with other metals. These properties are desirable for electronics applications in which the devices undergo significant stretching, twisting, and bending forces, such as in smart textiles for remote patient monitoring or athletic fitness trackers [79], reconfigurable antennas [52], [80]–[82], magnetohydrodynamic devices [83], [84], and reflective surfaces [85], [86].

Similarly to aluminum, which is in the same periodic group, gallium readily forms a thin but dense oxide shell of several nanometers in the presence of very small concentrations of oxygen by the chemical reaction below [87]–[89]:

$$4\mathrm{Ga} + 3\mathrm{O}_2 \rightarrow 2\mathrm{Ga}_2\mathrm{O}_3 \qquad \text{Eq. 6}$$

The dense oxide has enough strength to contain the liquid gallium within it, which enables the metal to be extruded into various profiles that freeze in place [11], [73]. When the alloy is free of the oxide, it exhibits Newtonian fluid characteristics. Conversely, when an oxide shell has formed on the surface, the alloys exhibit shear thinning characteristics [87]. This extrusion capability, coupled with additive manufacturing equipment, allows for three-dimensional metal structures to be produced at relatively low temperatures.

Gallium readily alloys with several metals [90], but is well-known for its properties as a room temperature, non-toxic, liquid metal. Alloying gallium with indium in the eutectic composition (75 % Ga, 25 % In) makes an alloy known as eutectic gallium-indium (eGaIn). When both indium and tin are added in the proportions 21.5 % In, and 10.0 % Sn, with the remaining 68.5 % Ga, galinstan is produced.

Gallium and its alloys exhibit relatively high electrical and thermal conductivities and a high reflectivity to electromagnetic radiation in the radio frequency band, making them ideal for electronic applications. At AC frequencies, electrical current experiences a skin effect, where the current is more easily able to travel along the outer surface of a conductor rather than through the bulk, as in DC circuits. The depth from the surface at which the current is able to penetrate is called the skin depth (δ), and is given by the following equation:

$$\delta = \sqrt{\frac{\rho}{\pi \mu f}} \qquad \text{Eq. 7}$$

where ρ is the electrical resistivity and *f* is the working frequency. μ is the magnetic permeability, given by the equation

$$\mu = \mu_0(1 + X_{\mathrm{V}}) \qquad \text{Eq. 8}$$

where μ_0 is the permeability of vacuum ($\mu_0 = 4\pi \times 10^{-7}$ H/m) and X_{V} is the volumetric magnetic susceptibility. X_{V} has not been reported in literature for eGaIn or galinstan. However, the mass magnetic susceptibility of eGaIn was reported to be -2.2×10^{-8} CGS M/g at a composition of 76 % Ga and 24 % In by mass [91]. The mass magnetic susceptibility can be converted to volumetric magnetic susceptibility and then from CGS units to SI units using the following two equations:

$$X_V = \rho X_{\mathrm{Mass}} \qquad \text{Eq. 9}$$

$$X_V^{SI} = 4\pi X_V^{CGS} \qquad \text{Eq. 10}$$

Where ρ in this case refers to the density of eGaIn of 6280 kg/m^3 [88]. The resultant volumetric magnetic susceptibility and magnetic permeability is -1.7×10^{-3}, and 1.25×10^{-6} H/m, respectively.

At 10 GHz, the frequency at which the experiment in the following section is designed, the skin depth for eGaIn is 2.73 μm. This gives a minimum allowable thickness of eGaIn metal for the device to function.

In recent years, gallium alloys have seen increased research of application in wireless communication technology, due to their high electrical conductivity and reflectivity. As a room-temperature liquid, gallium alloys combine the benefits of fluid properties with metallic properties. The increasing need for connectivity across the world has given rise to the desire for orbiting antennas that can precisely direct a signal to a specific point on the ground. One method of achieving this is by launching hundreds or thousands of satellites into orbit for maximum coverage, an alternative method is to use antennas that can reconfigure the shape of their reflecting dish. Several works have been published detailing several different designs of antennas [52], [80], [81], [92]–[96], however, each of those publications involved fabrication of relatively small (< 25 x 25 cm) antennas, or reconfigurable antennas made from mechanical components.

In this section, a horn antenna with a stretchable, liquid metal-based reconfigurable reflector was designed and fabricated for use at 10 GHz. The reconfigurable horn antenna discussed will ultimately be designed for low Earth orbit (LEO) applications, but space qualified materials will need to be investigated to further this work. The environmental effects of LEO are severe, and include the effects detailed in Table 6. Figure 29 shows a visual representation of the horn antenna assembly.

Table 6. Low Earth Orbit Environmental Effects [97]–[99]

Effect	**Details**	**Failure Risk Modes**
Vacuum	-Pressures between 10^{-6} – 10^{-9} torr	-Outgassing of polymeric materials
Atomic Oxygen	-The most significant component of LEO component degradation -Produced when UV below 253.7 nm breaks the bond in molecular oxygen	-Reacts strongly with carbon, hydrogen, nitrogen, and sulfur bonds, and degrades fluorinated polymers -Reacts with PDMS to produce brittle SiO_2 surface layers and forms polar groups with C and H
Ultraviolet Radiation (UV)	-Without atmospheric absorption, short-wave UV (< 253.7 nm) emitted by the sun is more prominent in LEO	-Damages polymers via chain linking or chain scission
Ionizing Radiation	-Caused by galactic cosmic rays, protons emitted by solar flares, or radiation belts	-Similar effects as UV radiation, but not as significant
Plasma	-Composed mainly of O+ ions and free electrons	-Similar effect as atomic oxygen

Temperature	-Typically cycles between -120 °C – 120 °C -16 cycles per day at International Space Station (ISS) elevation	-Heating and cooling is required to maintain large components at proper operating temperatures -Thermal properties must be sufficient that astronauts can handle them without temperatures exceeding the gloves specified limits
Orbital Debris Impact	-Micrometeoroids of 10 – 100 µm in size -Larger particles 1 mm and above -Impact velocities from 10 – 60 km/s	-Micrometeoroids may embed within the material or pass through if the material is soft enough

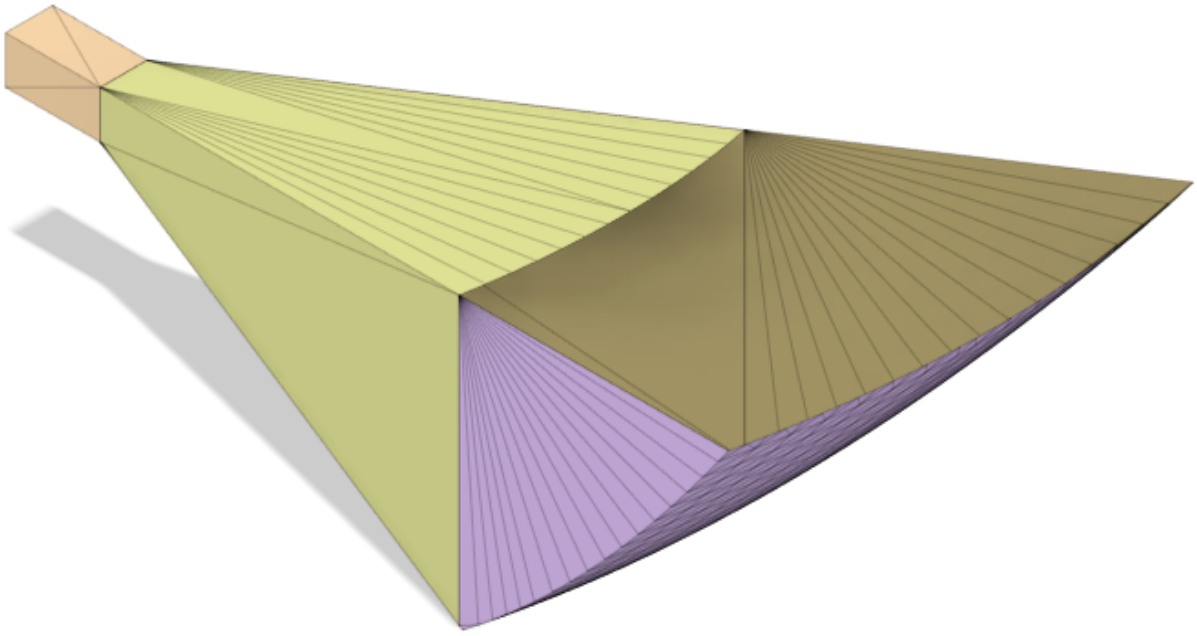

Figure 29. Proposed design of reconfigurable horn antenna. The orange section is the waveguide, the yellow section is the horn, and the purple section is the reconfigurable reflector.

5.2 Experimental

In order for the reflector to be effective, its electrical properties must match those of the frequency band in which it is designed. For this experiment, three main components were required: The horn and waveguide body, reflector, and coaxial adaptor, of which the two former components must be electrically conductive.

5.2.1 Horn and Waveguide

The horn and waveguide are static components, so they may be made from rigid materials. AA6061 aluminum was chosen due to its low density, and its current use in aerospace applications [100], [101]. AA6061 has a high electrical conductivity of 2.5×10^7 S/m, making it a suitable choice of material for these components[102]. Gallium is known to effectively embrittle aluminum alloys [103]–[105], so it is of utmost importance to prevent any liquid-phase gallium alloy from contacting the horn.

The horn and waveguide were designed as 5 pieces and welded together at the corner seams, as shown below in Figure 30. A CAD drawing for the horn and waveguide can be found in Appendix B.

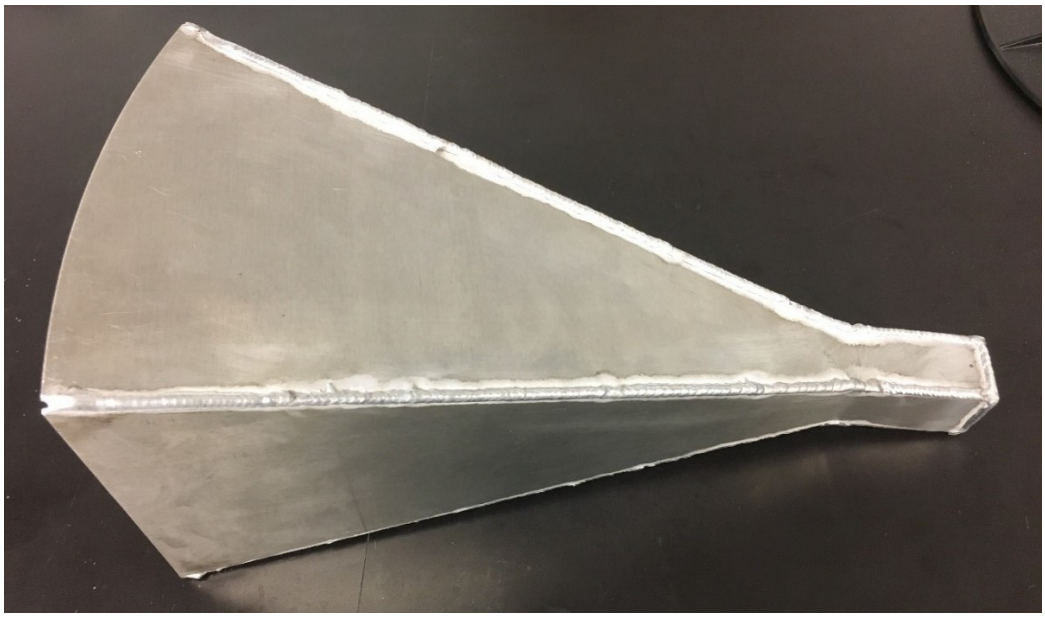

Figure 30. Assembled horn and waveguide.

5.2.2 Reflector

EcoFlex 00-30 (Smooth-On, USA) was chosen as the substrate material for the reflector based on several advantages. EcoFlex is a trademark name for a series of two-part, platinum-cured silicone with a Shore hardness range between 00-10 and 5A, and elongation to failure values from 800 % – 1000 %. It has a mixed viscosity low enough that it can be cast into molds after mixing and degassing. Mechanically, EcoFlex 00-30 has a high elongation to failure (900 %), which is desired for continuously compliant devices. Further, there has been other research involving the use of EcoFlex in tandem with gallium alloys to create compliant electrical devices, including those working at or near 10 GHz frequencies [80], [106]–[109]. EcoFlex 00-30 has a reported dielectric constant (ϵ_r) and loss tangent ($\tan\delta$) of 2.8 and 0.02, respectively at 2 GHz [110]. The low loss tangent is beneficial for preventing too much loss of the signal as it passes through the EcoFlex layer twice.

The shape of the reflector required building it in 3 parts – 2 side walls and the main parabolic dish. Both of the sidewalls are identical in dimensions, and the main dish required a cavity, so 2 molds and 1 core were required. The molds and the core were produced from 3 mm thick transparent PMMA sheets, laser cut into the profiles of the reflector. The cut molds were then adhered to a backing layer of 3 mm thick PMMA using a thin layer of acetone and clamped together for 24 hours.

Some crazing was evident between the joints, which is a common issue encountered with PMMA and organic solvents when stress is applied [111]. Crazing is surface defect in which a tensile stress causes the polymer chains to separate, creating voids within the material. It is analogous to a crack, with the difference being that a crazing defect is mostly confined to the surface of the material, but it can eventually create cracks in the bulk. Crazing appears in transparent PMMA as a network of white surface fractures caused by a difference in the refractive index of the crazed area compared to the rest of the PMMA. Similar to a crack, crazing decreases the mechanical strength of the polymer. However, in this case mechanical properties are not critical, and the effectiveness of acetone as a bonding agent between PMMA and itself outweighs the reduction in mechanical properties imparted by the defect. The criteria for a successful mold was based on the ability for the mold to contain the mixed silicone until cured, and for the mold to release the cured part.

EcoFlex 00-30 was prepared by weighing and then vigorously mixing together 125 g of each of Part A and Part B in a polypropylene cup with a stir rod for 1 minute, followed by placing the cup in a vacuum oven (Isotemp™ Model 281A, Fisherbrand™, USA). The chamber door was then closed, and a vacuum valve was slowly opened until a vacuum pressure of 610 mmHg was reached. Too fast of a pressure drop resulted in large air bubbles forming in the silicone, leading to overflow of the polymer over the sides of the cup. After approximately 1 minute, the vacuum valve was closed, and the cup was removed from the oven. The silicone was then poured by hand from as low a height as possible into the PMMA mold, ensuring that all of the corners were filled, and the thickness of the polymer was uniform. The part was then left for 24 hours to cure and then removed from the mold.

eGaIn was used as the reflective material due to its ease of processing compared to galinstan. 60 g of eGaIn was prepared by slicing 15 g of thin strips of indium (99.99 % purity) (Rotometals,

USA) using a scalpel and placing them into a 100 mL Pyrex beaker. Solid gallium (99.99 % purity) (Rotometals, USA) was heated to 60 °C and 45 g of the molten gallium was poured into the beaker containing the indium. A Teflon stir rod was used to mix the metals together and then the beaker was placed on a hot plate set to 165 °C to ensure that the indium fully alloyed with the gallium. Indium has a melting temperature of approximately 157 °C [112], so the 8 °C superheat ensures that all of the indium will have melted, improving the alloying capability between the gallium and indium. The same procedure was used in preparing galinstan, but 41.1 g Ga, 12.9 g In, and 6 g Sn were added to the beaker instead.

Several different approaches to fabricating the reflector were attempted, as shown in Figure 31.

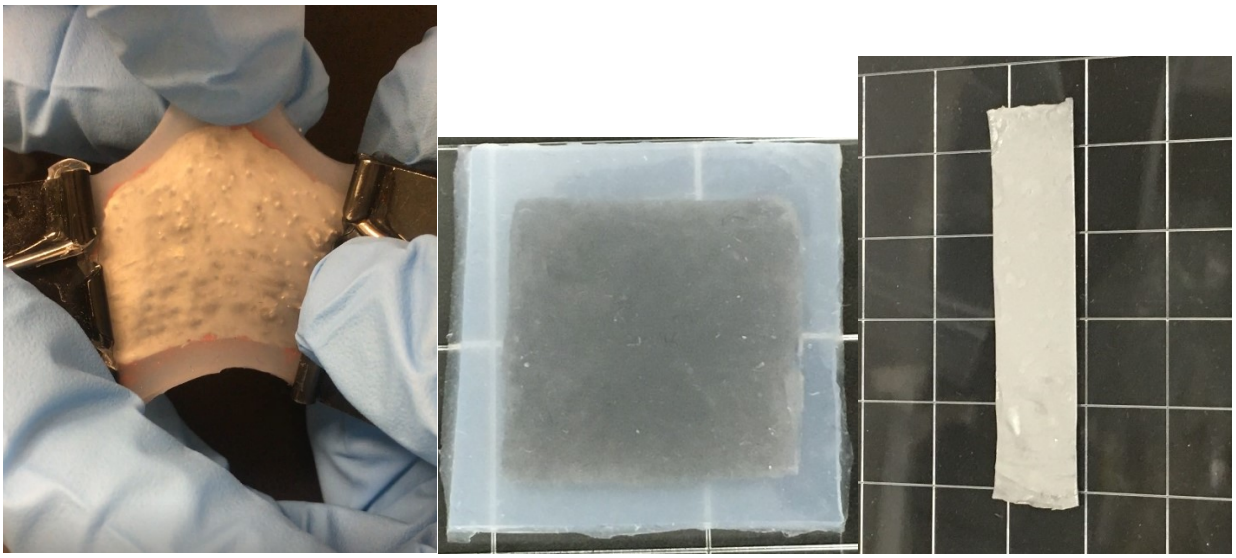

Figure 31. Initial attempts at fabricating a stretchable reflector. (a) Pinning the liquid metal to steel balls, (b) EcoFlex laminated on top of liquid metal, (c) EcoFlex/liquid metal composite.

5.2.2.1 Pinned Reflector

The first attempt involved attempting to pin the liquid metal in place using steel balls fixed to a stretchable silicone substrate. An EcoFlex mold was made by casting EcoFlex around a 25 x 25 x 1 mm piece of PMMA fixed to the base of a petri dish. After the mold had cured, RTV 159, a room-temperature vulcanizing silicone (Momentive, USA), was applied to the mold cavity until it was just below the surface of the mold. RTV 159 is a very viscous (~200000 cP), acetoxy-cure silicone that bonds well to many materials [39]. It has a hardness of Shore 28A and an elongation to failure of 825 %, which make RTV stiffer than EcoFlex 00-30. However, it is sufficient for this

application. A 22 x 22 mm grid of 1 mm diameter holes was laser cut in PMMA. A total of 121 holes (11 holes x 11 holes) were filled with 0.79 mm (1/32”) steel balls, and then the uncured RTV silicone was lowered onto the steel balls, causing them to lift from the grid and become embedded in the silicone. After the silicone had cured, galinstan was placed in the 25 x 25 mm square using a polypropylene transfer pipette until the steel balls were completely submerged. Steel balls were used in an attempt to pin the liquid metal in place by causing it to wet and partially adhere to the steel balls, preventing bulging of the liquid metal at the lowest point of the reflector due to gravitational effects, or from forming a sphere in zero-gravity applications. The exact grade and composition of the steel balls is unknown, but due to observed magnetism of the balls, they are expected to be a type of chromium-alloyed steel or high-carbon steel. Previous work has shown that gallium alloys do not aggressively attack 316L stainless steel below 300 °C after up to 3 months of continuous exposure [10], [113]. Steels are excellent candidates for interface materials with gallium alloys below approximately 400 °C due to the limited intermetallic formation between gallium and iron that occurs below 400 °C [114]. A phase diagram showing this relation is shown in Appendix C.

Encapsulating the liquid metal using EcoFlex was initially done by mixing Parts A and B and degassing as above, and then carefully pouring over top of the EcoFlex/RTV159/steel ball/liquid metal assembly, followed by a subsequent degassing step. Figure 32 shows the reflector in each intermediate step.

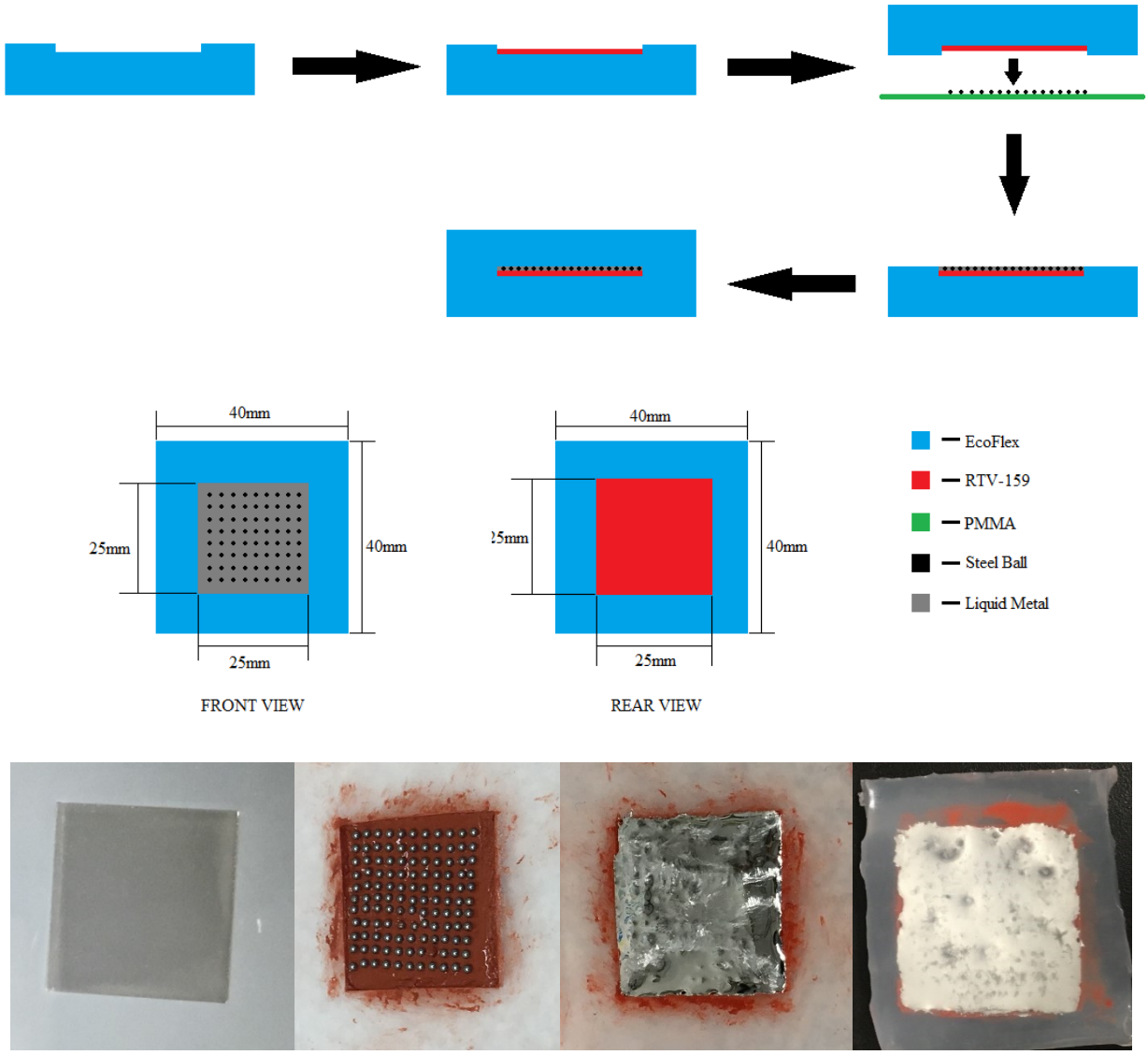

Figure 32. Top: schematic process flow of reflector fabrication. Bottom: intermediate steps in fabrication of a pinned reflector.

The pot life sensitivity to degassing was significant, as shown below in Figure 33. The EcoFlex had become so viscous after 30 minutes that degassing produced large bubbles that stabilized in that shape and produced significant defects. The EcoFlex showed indications of shrinking away from the liquid metal, producing uneven surfaces containing porosity. Furthermore, the left image in Figure 33 shows that the galinstan did not always wet the steel balls, which defeats the purpose of this method.

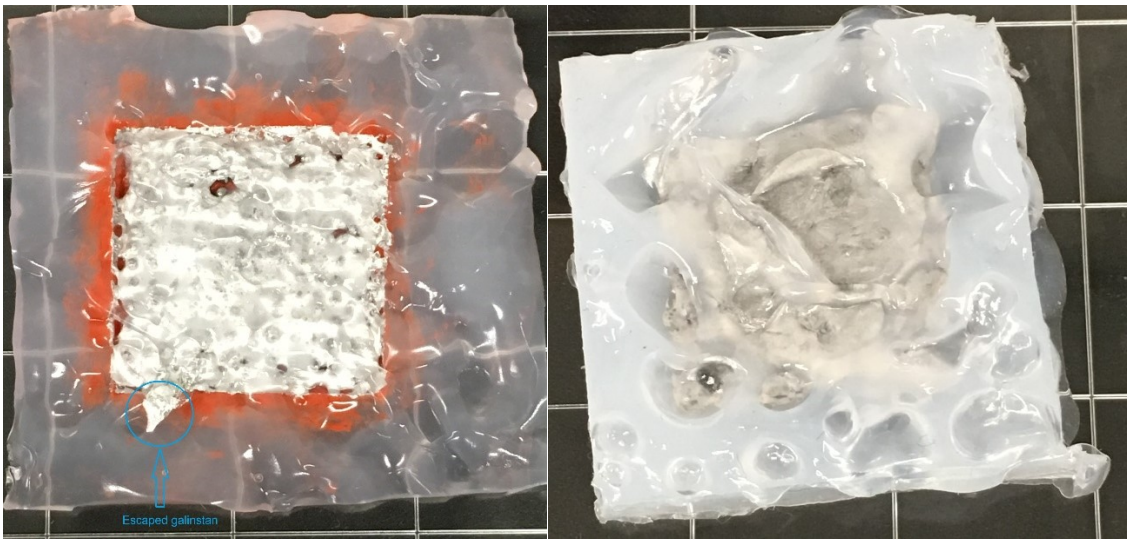

Figure 33. EcoFlex encapsulation defects encountered when casting too close to the end of the pot life.

5.2.2.2 EcoFlex Lamination

In order to avoid the defects encountered when directly casting EcoFlex on gallium alloys, an attempt to laminate a semi-cured layer of EcoFlex on top of a fully cured layer was made. The base layer was fabricated by casting EcoFlex 00-30 around a 25 x 25 x 1 mm piece of PMMA as above and left to cure for 24 hours. A piece of paper with a 25 x 25 mm square cut out of it was used as a mask for preventing eGaIn from contacting undesired parts of the EcoFlex. Conversely to the previous method, the cavity produced by the PMMA was filled to the top solely with eGaIn. A 50 x 50 x 5 mm piece of EcoFlex was cast separately. After 1 hour, a small amount of EcoFlex was mixed together to use as an adhesive and brushed on the cured EcoFlex. The recently cast piece was removed from its mold and placed on top of the cured part and a small amount of pressure was applied by hand. The resultant reflector functioned well, but needed to be massaged to remove air bubbles trapped in the eGaIn, as shown in Figure 34.

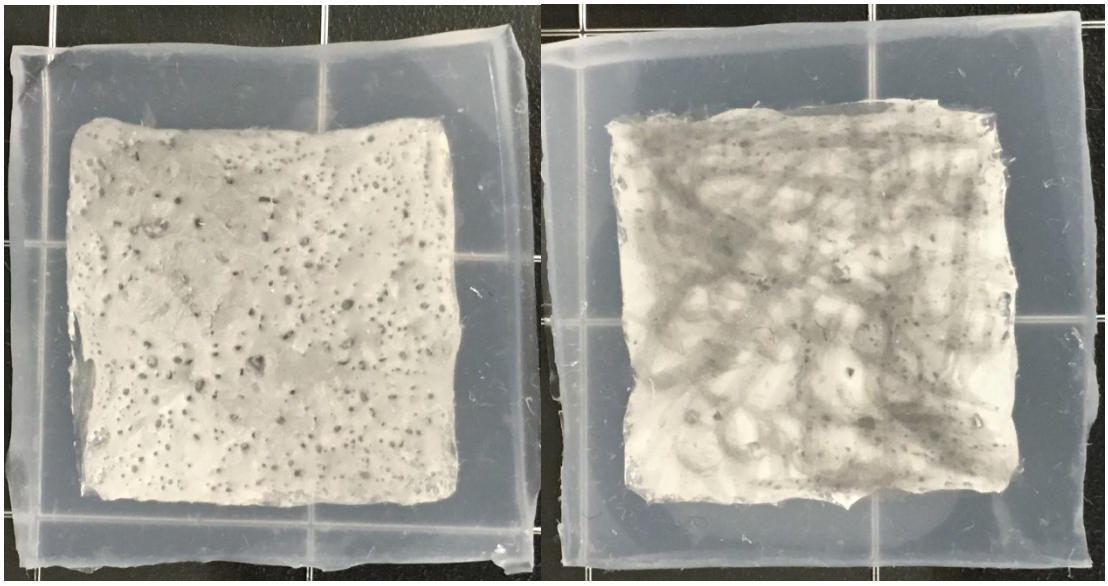

Figure 34. Laminated reflector showing before (left) and after (right) massaging out air bubbles from the eGaIn.

The reflector sample was tested by students in Dr. Mousavi's lab and was empirically verified to have a detectable reflectance between 8 – 12 GHz.

5.2.2.3 eGaIn Composite

A third method similar to that described in [115] was attempted in order to prepare an EcoFlex/eGaIn composite. 5 g samples were produced for this experiment. 0.5 g of Part A of was added along with a measured amount of eGaIn based on the desired concentration to a polypropylene cup. Using a Teflon stir rod, the prepolymer and liquid metal were thoroughly mixed by hand for 3 minutes until a visibly uniform mixture was formed. Next, 0.5 g of Part B was added and mixed for another minute by hand, followed by placing the cup in a vacuum furnace and degassing at 508 mmHg vacuum with the oven off for 5 minutes. Afterward, the vacuum was turned off, the sample was removed from the oven, and the contents were poured into the lid of a polypropylene petri dish and left to cure for 24 hours. Samples with eGaIn concentrations of 10, 20, 30, and 60 wt.% were produced.

Electrical conductivity was not achieved with any of the liquid metal weight fractions after applying mechanical pressure to create traces, which agrees with [115] for weight fractions below 60 %. The optical microscopy images shown in Figures 35-38 below confirm that although a

generally uniform composite was produced, the spacing between the liquid metal droplets was too great to reliably rupture the walls between them and produce a continuous electrical trace. In the 60 % sample, any distinction between the eGaIn and EcoFlex is undiscernible.

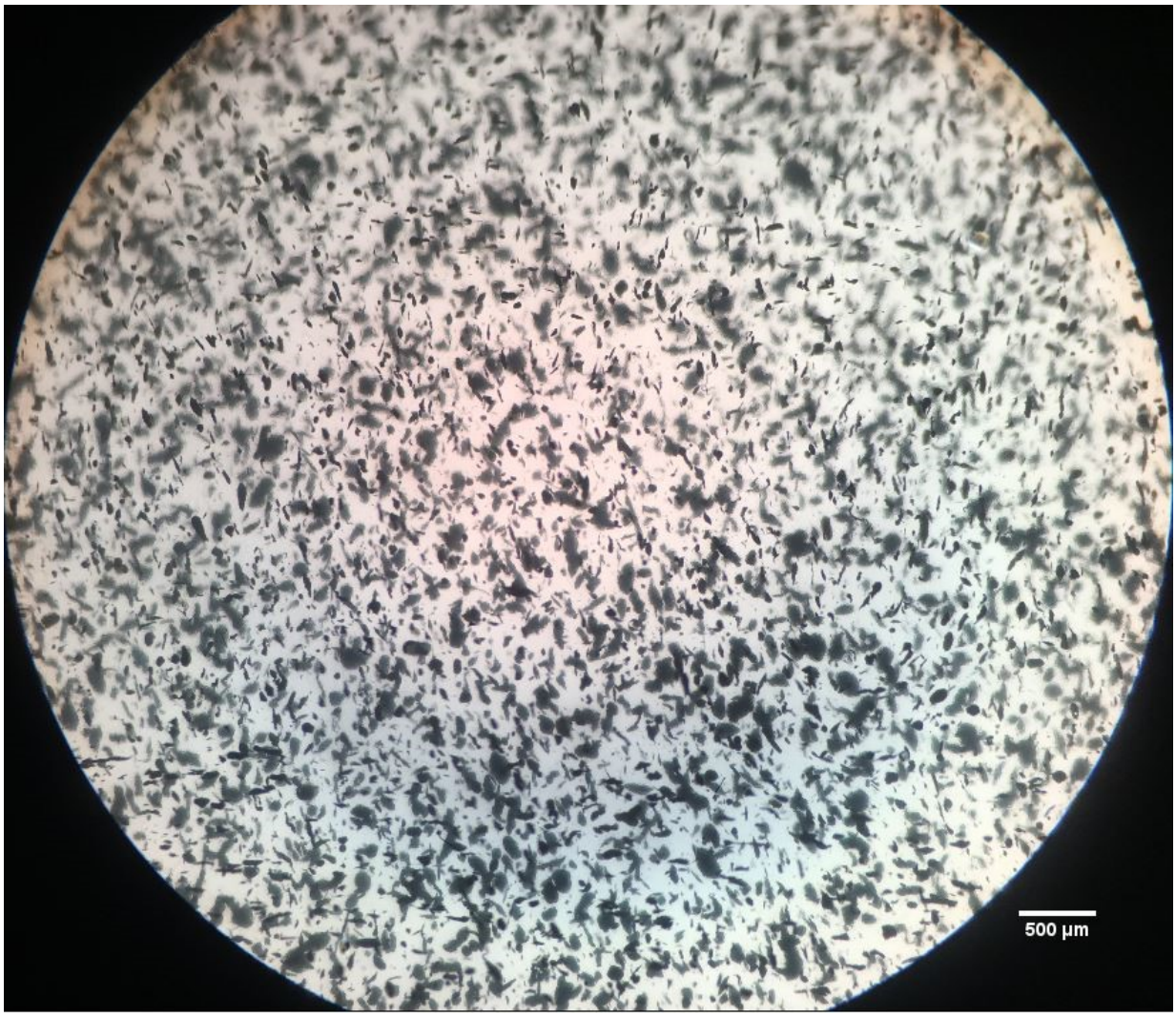

Figure 35. Optical microscopy image of EcoFlex 00-30 containing 10 wt.% eGaIn.

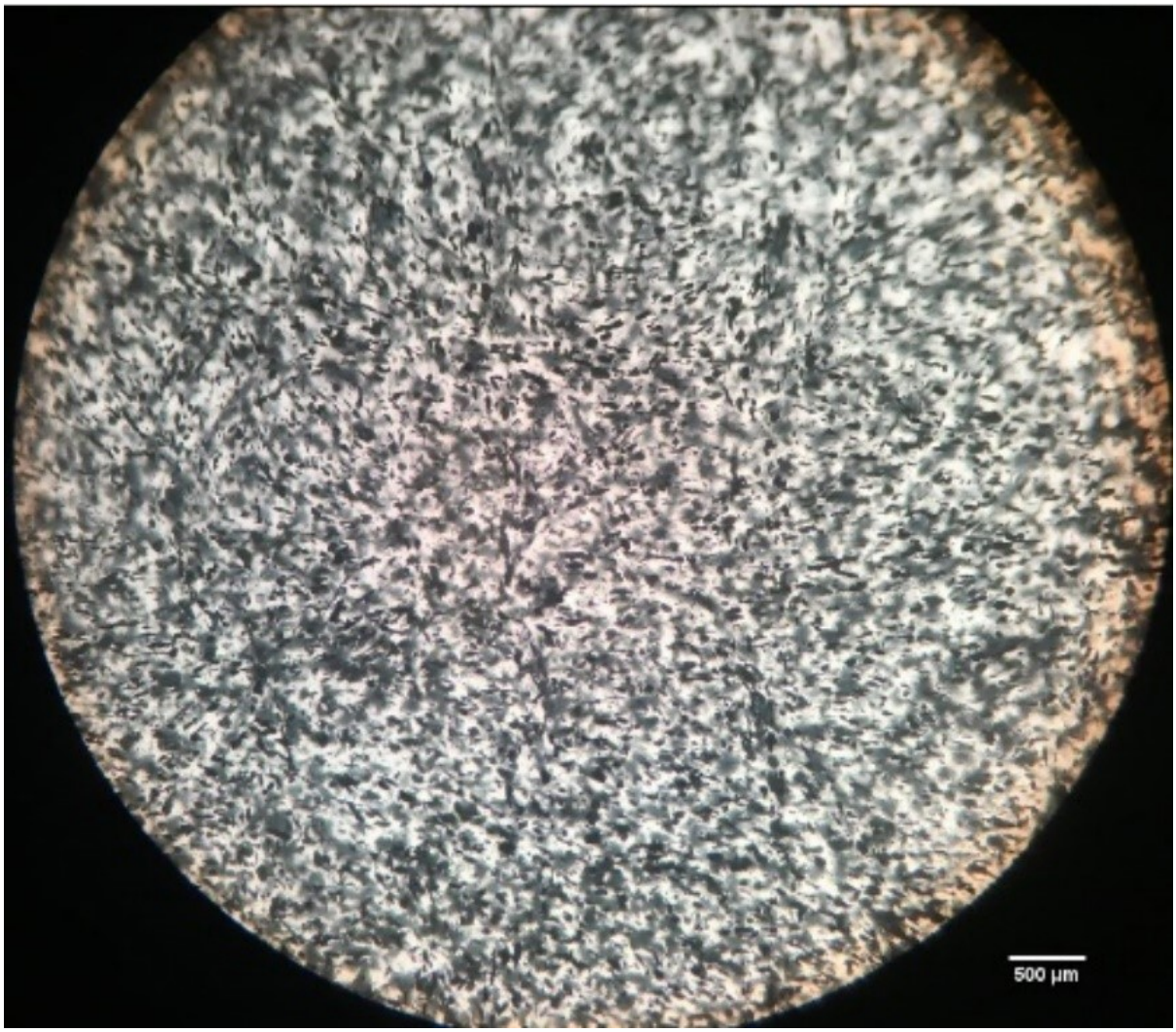

Figure 36. Optical microscopy image of EcoFlex 00-30 containing 20 wt.% eGaIn.

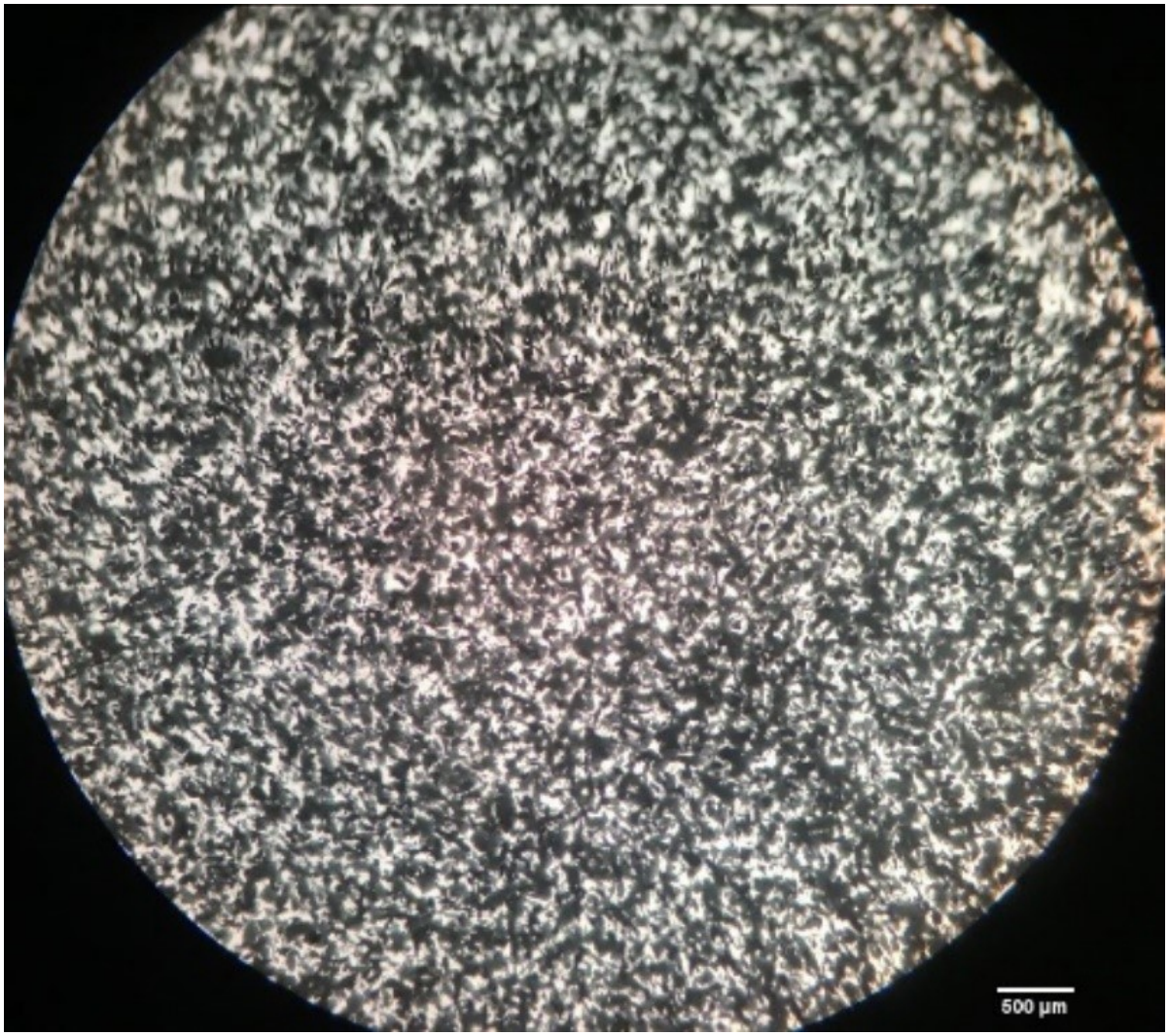

Figure 37. Optical microscopy image of EcoFlex 00-30 containing 30 wt.% eGaIn.

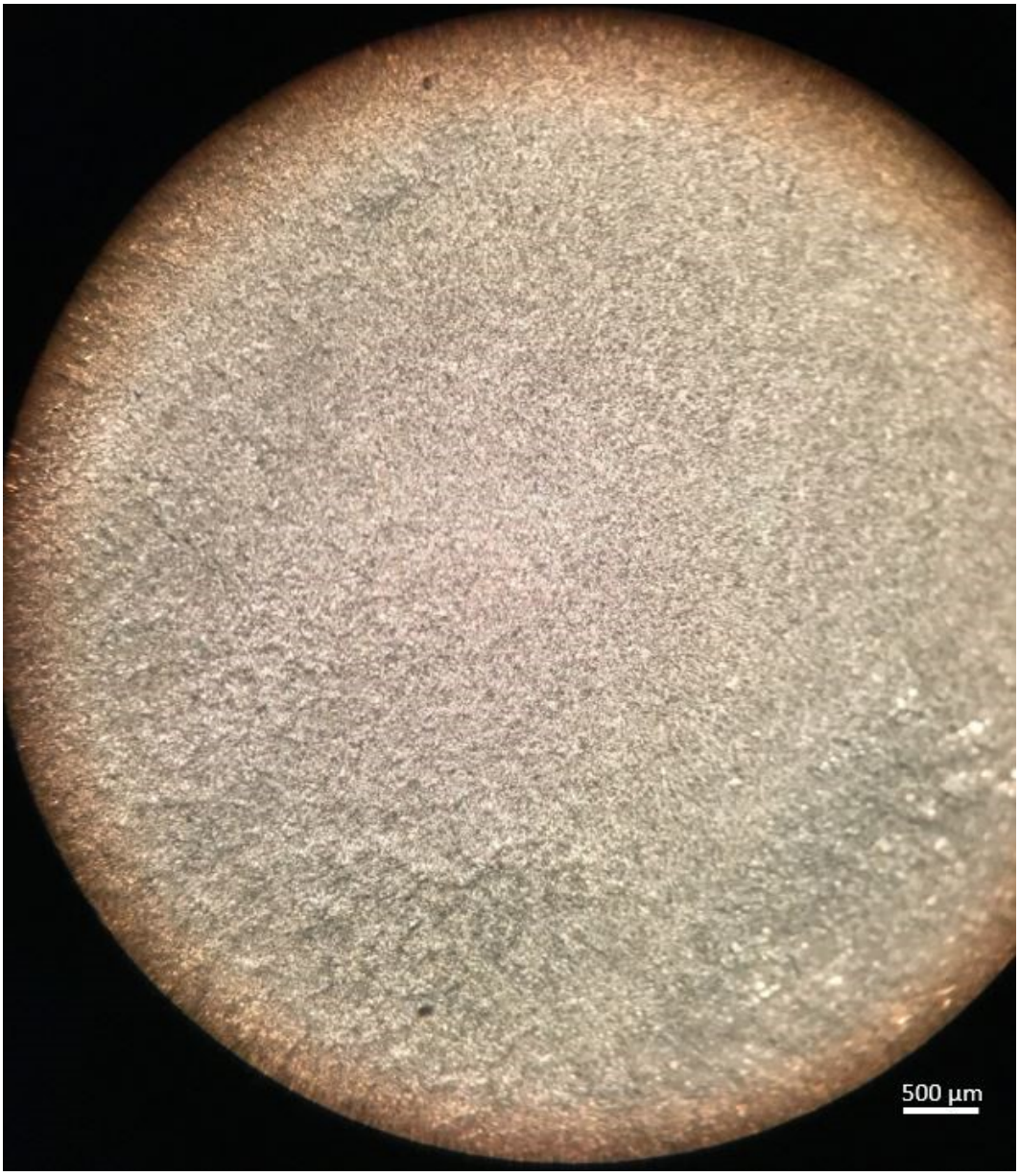

Figure 38. Optical microscopy image of EcoFlex 00-30 containing 60 wt.% eGaIn.

When the 60 % eGaIn sample was pressed with a light mechanical force, the polymer walls ruptured and eGaIn began to ooze out of the composite, as shown below in Figure 39.

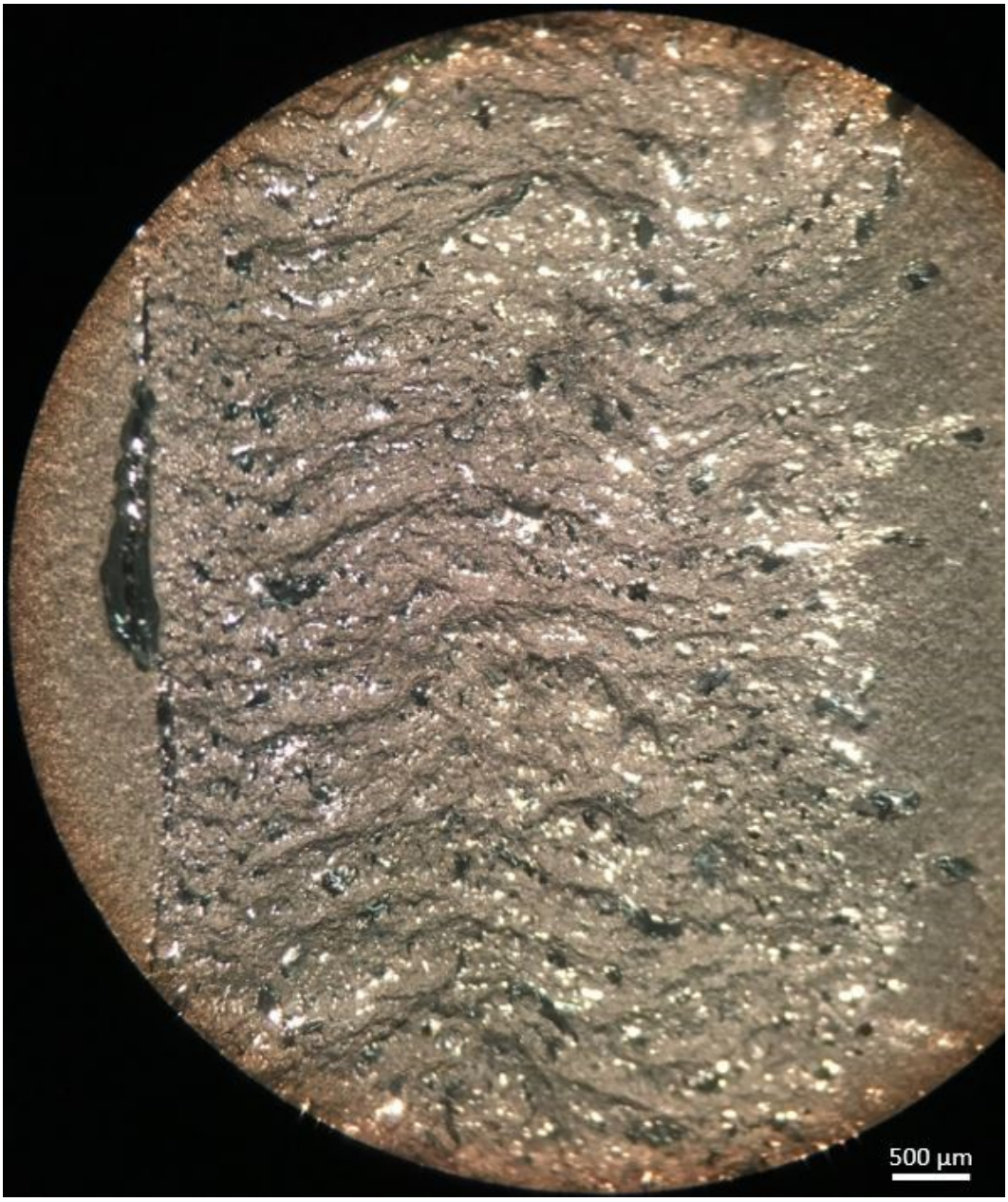

Figure 39. Escape of eGaIn out of the composite after applying mechanical pressure.

The samples were tested for their reflection coefficients using a ZVA 67 vector network analyzer (Rohde & Schwarz, Germany). This device measures the behaviour of electronic devices when an RF signal is applied to them. In this case, only the reflection response is considered. The results are shown below in Figure 40, shown as S_{11} values. The subscripts following the S indicate the port number, where the first and second subscripts indicate the output and input ports, respectively. The value of S_{11} therefore indicates the amount of RF energy reflected back from the reflector.

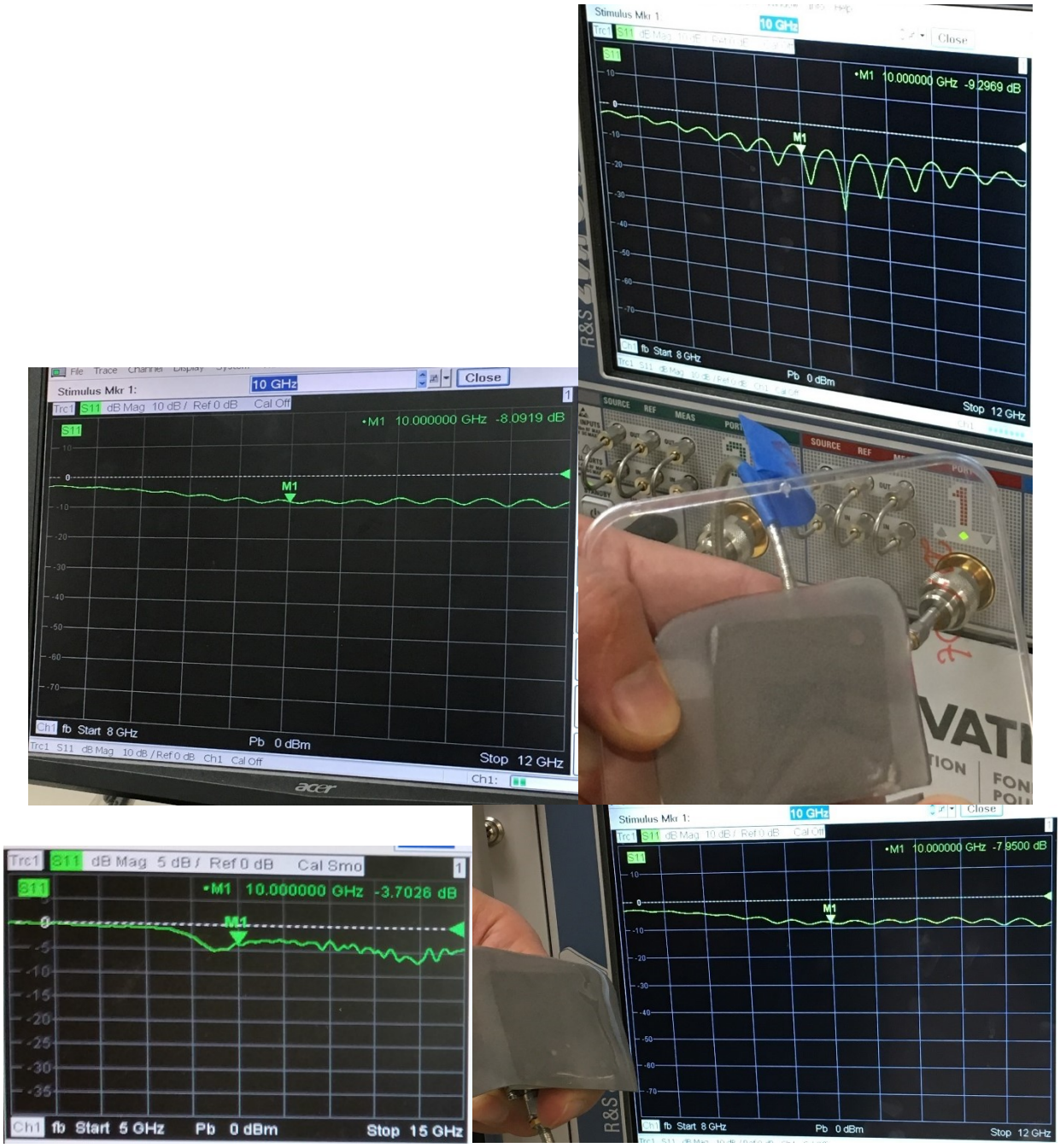

Figure 40. Reflection coefficient results (S11) for EcoFlex 00-30/eGaIn composite films. (Clockwise from top left) 10 wt.% eGaIn, 20 %wt. eGaIn, 30 %wt. eGaIn, 60 %wt. eGaIn.

5.2.3 Assembly

Ultimately the most effective solution was to use as few components as possible which resulted in using an EcoFlex cavity filled with eGaIn followed by lamination of a top layer.

Despite having a relatively low viscosity, the EcoFlex did not produce a uniform thickness in the mold. Areas near the base of the reflector were thicker than near the top edge, as shown in Figure 41.

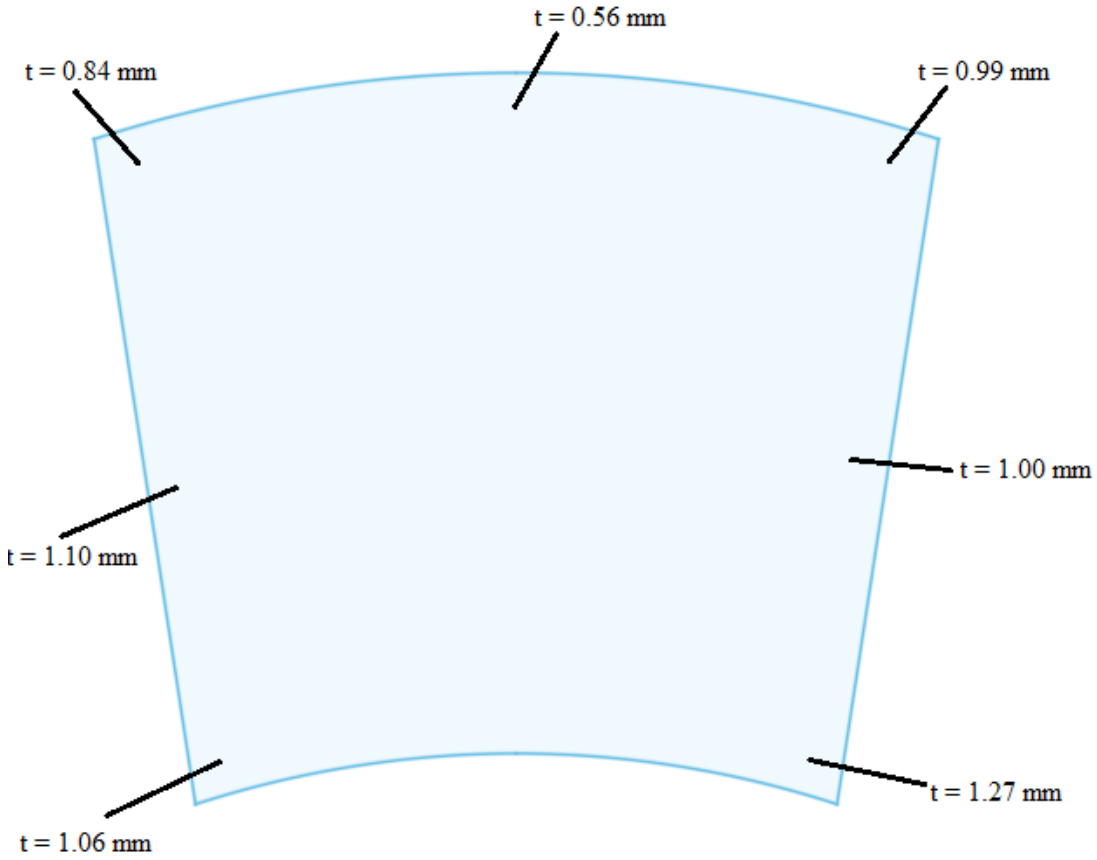

Figure 41. Reflector thickness distribution.

As was done in the qualifying experiment, a paper mask was placed around the edge of the cavity produced in the mold and eGaIn was cast into the cavity. Some eGaIn was able to squeeze between the paper and EcoFlex, as shown in Figure 42, below.

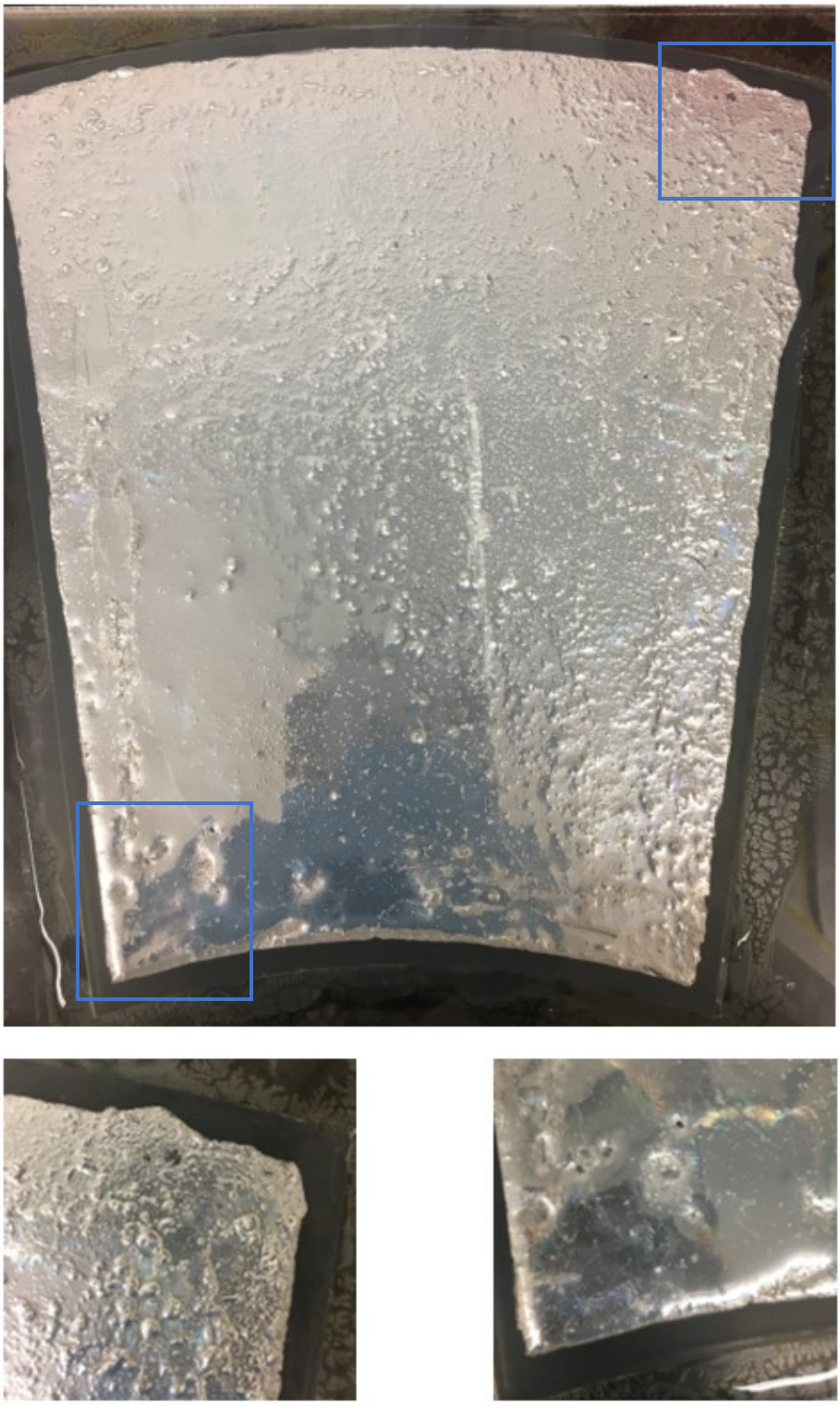

Figure 42. Reflector containing eGaIn prior to top layer lamination. Left inset: eGaIn that overflowed and penetrated between the paper mask and EcoFlex. Right inset: Oxidized eGaIn around air bubble pockets.

The top layer was produced using the same mold as the bottom layer without the core section. After allowing the EcoFlex to cure for an hour, a thin layer of freshly prepared EcoFlex was brushed onto the layers to be bonded, and then the top layer was placed on top and adjusted for alignment. The reflector was allowed to cure for 24 hours, and the process was repeated for both of the side sections of the reflector.

RTV 159 exhibits good bonding strength with silicones and metals, which led to it being chosen to assemble reflector to the waveguide and horn. RTV 159 was applied to the edges of the reflector components to attach the side pieces to the main reflector. Although the manufacturer specifies a tack-free time of 45 minutes, it takes up to 7 days for the silicone to reach its full mechanical strength [39]. Hence, a jig was made to hold the side pieces upright using binder clips while the RTV 159 cured. Once the reflector assembly was finished, RTV 159 was applied the horn opening and the reflector assembly was attached. The final reflector is shown below in Figure 43. Unfortunately, the strength of the RTV 159 between the reflector and horn was not sufficient, and the reflector collapsed under its own weight. Some RTV 159 remained on the edge of the reflector surface, preventing reattachment to the horn because RTV 159 does not bond to cured RTV 159.

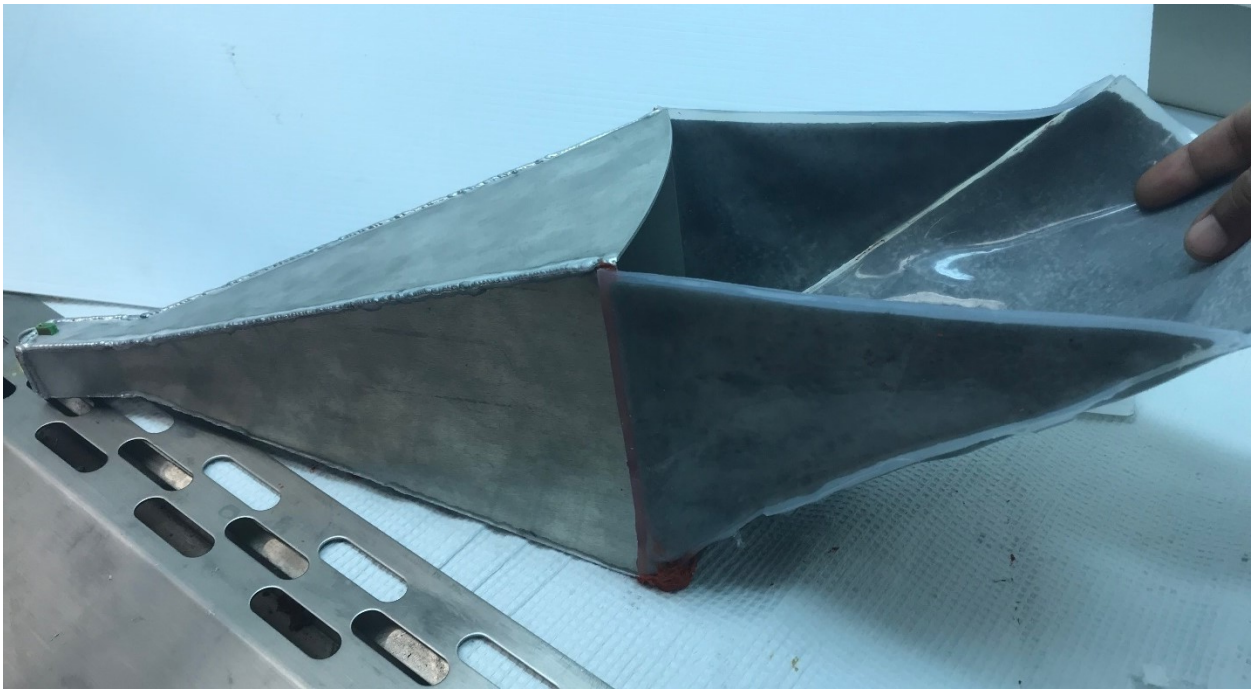

Figure 43. Assembled horn, waveguide, and reflector.

5.2.4 Actuation

In order to change the direction of the produced signal, actuation of the reflector is required. A ratcheting gear system was designed and prototyped using laser cut PMMA, as shown below in Figure 44, but it was unable to be tested before the project was suspended.

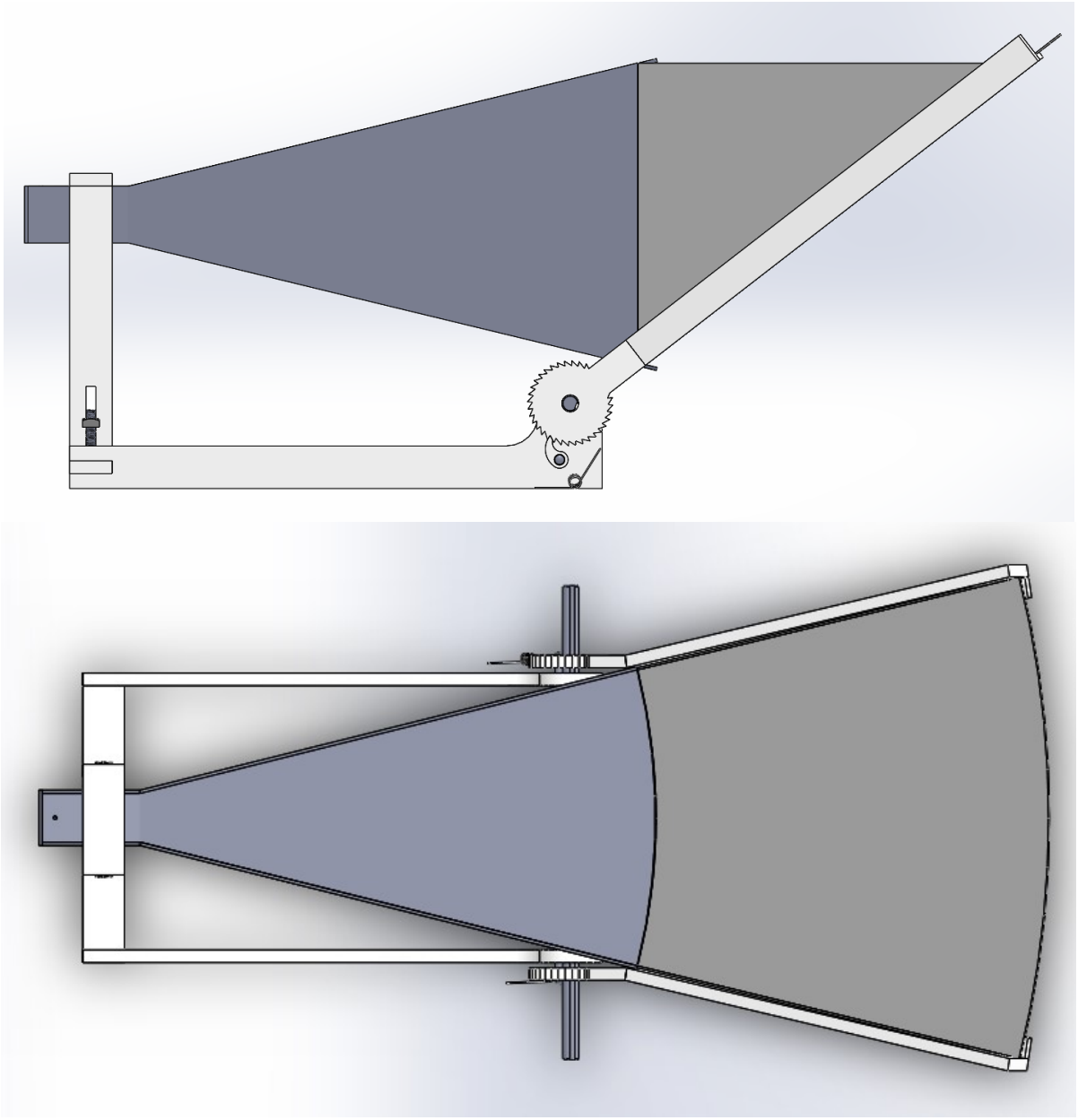

Figure 44. Side and top views for actuation system for reconfigurable reflector antenna.

5.3 Conclusion and Future Work

There is much potential for this project to be successful. There are several problems to solve in which to ensure success:

- Utilization of a stiffer silicone. It was determined near the end of the project that the maximum required strain of the reflector was approximately 15 %, which is significantly lower than the reported elongation to failure of 900 % for EcoFlex 00-30 [116]. An appropriate material is achievable with a wide variety of commercially available silicones. However, too stiff of a silicone will require additional force from the actuation mechanism, so a balance between the silicone stiffness and actuator capability will need to be investigated [117]. Dragonskin 30, TC-5030 from BJB Enterprises and Sylgard 184 are all stiffer silicones that may have been useful had this project continued.
- Despite the lack of success in producing an electrically conductive EcoFlex/eGaIn composite, other work [115] showed that it is possible. Further investigation into the ideal composition of liquid metal to silicone is required, as well as the feasibility of fabricating the composite on a large scale ($\geq$ 25 x 25 cm) which is larger than most demonstrated materials in the academic literature. The composite takes less time to prepare and uses less material than the other proposed methods in this section. What isn't known is the impact of the non-conductive areas of the composite on antenna performance.
- Attachment of the reflector to the horn requires improvement. This can be done by extending the length of the reflectors so that they can be attached to the horn along the sides and bottom. The increased surface area would theoretically provide enough of a bonding area such that the reflector will stay attached to the horn, including after strain has been applied to the reflector. A gradient of material stiffnesses should also aid in the durability of the bond.

Chapter 6: Direct 3D Printing of Stretchable Circuits via Liquid Metal Co-Extrusion within Thermoplastic Filaments

6.1 Introduction

This section involves the design and application of additively manufactured, stretchable, and conductive wires. There has been growing interest in the use of gallium-based liquid metals, as described earlier. This is partly due to their ability to be patterned relatively easily because of the combination of a low viscosity liquid phase and an oxide skin that forms in air, providing some structural support for the molten metal inside. As well, previous investigations into the use of LM in stretchable electronics suggest that it is a good material for such applications.

Various methods of fabricating LM exist, of which stencil printing, droplet deposition, injection into channels or cavities, and direct writing [10], [11]. Despite its relative ease of patterning, the non-Newtonian behaviour of the alloy caused by the oxide makes direct printing of LM alloys difficult and unpredictable. One potential solution is by combining LM with microparticles to form a thixotropic paste [118], [119]. This provides a method to control the effective viscosity of the alloy. Mohammed et al. successfully printed liquid metal based flexible electronics [51], however, they used a suspension of liquid metal particles, and it required an additional sintering step. Zheng et al. demonstrated directly printed circuits-on-paper flexible electronics using a low-cost, simpler technique which can only process 2D circuitry without a sealing material [120].

Regardless of the patterning method, prevention of the LM circuits from being destroyed by mechanical abrasion or contact with other surfaces for all actual end applications, requires an encapsulation step [81], [121], [122]. Because of this, direct printing of liquid metal in additive manufacturing processes is still an unsolved issue. Only one paper to date has demonstrated a method for direct encapsulated printing of eGaIn, and it was difficult to achieve consistent streams of liquid metal because the viscosity of the surrounding silicone rubber was relatively low [121]. To address this encapsulation challenge, a thermoplastic FDM extruder was modified to extrude thermoplastic polymers combined with coaxially extruded LM cores to produce directly printed

stretchable wires that can be deposited in 2D or 3D shapes. This printing method is compatible with other thermoplastic or thermosetting process steps and can also produce very thin wire cross-sections through a combination of extrusion and drawing processes, eliminating most of the challenge of injecting liquid metal into small diameter channels [81], [123]. In this work, only LM alloys were used as conductive materials, however, the technique can also be utilized to print with other low-melting-point metals, as well as gallium, bismuth, tin and indium-based alloys which melt at around 250 °C [122]. Despite some not being liquid at room temperature, low melting point metals or alloys have the potential for use in applications where stretchability is not a desired property, but rather where mechanical strength, conductivity, or density are of primary concern. The stretchable electronic devices fabricated in this section are designed to work optimally between STP and average internal body temperature (37°C). However, based on the properties of the component materials, these devices would be operational with liquid metal properties to minimum temperatures of 15.5°C and -19°C when using eGaIn or galinstan, respectively. SEBS has two distinct glass transition temperatures, corresponding to that of styrene (90.5°C) and of the ethylene-butylene block (-44.5°C) [36], [124], [125], which permit elastomeric properties down to low temperatures. The upper T_g of 90.5°C allows for operation up to this temperature until viscous flow of the styrene blocks occurs.

6.2 Experimental

In this chapter, a thermoplastic tri-extruder system compatible with FDM printers that is capable of both intermixed and co-axial extrusion of multiple materials in a single process was used to print the samples and devices, as presented in previous works [126]–[128]. The printing head has three input channels where two angled inputs are designated for feeding thermoplastic materials with the third input reserved for co-axial extrusion of a central core fluid. A 3D model of the tri-extruder is presented in Figure 45(a).

In order to directly 3D print thermoplastic elastomers from pellets, an extruder-based feeding system was developed, as described elsewhere [128]. The feeding system consists of a screw extruder coupled with a heated hose to convey the polymer melt to the print head. The screw extruder system is a modified version of a filament extruder system purchased from Filastruder

(USA) [129]. In this work, one thermoplastic input channel was closed using an M6 screw, but it can be opened to take other thermoplastic filament inputs for blending functions [74]. The central LM core was fed using a reusable, 304 stainless steel central needle (gauge 22, ID = 0.016" (0.406 mm), OD = 0.028" (0.711 mm), McMaster-Carr) which was kept concentric to the nozzle having an inner diameter of 1.8 mm. The needle was connected to a syringe pump (Harvard Apparatus, Pump 11, Pico Plus Elite) through flexible silicone tubing and luer-lock connections. The tri-extruder system was installed on a Geeetech M201 FDM 3D printer (Geeetech, China) [130]. The whole setup is shown in Figure 45(b), where all of the major components are illustrated.

For the encapsulating material, an insulating thermoplastic with high stretchability, flexibility, and mechanical stability was desired. Based on these properties, SEBS was chosen because of its superior mechanical properties suitable for stretchable electronics applications [36], [52], [126], [131]. In this work, a commercially available type of SEBS, Kraton G1657 was used. Three types of electrical devices were printed: stretchable wires, a planar spiral resistive sensor, and a 3D spiral inductor.

6.2.1 Stretchable Wires

Stretchable wires were produced by simply allowing the extruder to extrude a continuous stream of coaxially-filled SEBS vertically while varying the extrusion temperature, extrusion rate of the SEBS, and flow rate of the LM. The most reliable extrudates were produced between 180 °C and 200 °C, at flow rates between 2 – 5 mm/s for the LM and 2 mm/s for the SEBS. Samples of 1 m long each were produced, showing two distinct encapsulation regimes. By lowering the LM needle tip approximately 1 mm outside of the extruding nozzle, a continuous trace of LM was produced.

After the coaxial wires were extruded, while the temperature of the SEBS was above the T_g, the wires were further drawn using a motorized winder to reduce the diameter of the SEBS and subsequently the diameter of the internal LM. By varying the drawing speed, LM diameters as fine as 25 µm were achieved. Lin et al. reported a manual drawing process of liquid metal wires at room temperature using curable polymers [77]. However, that process is not suitable for producing continuous wire because the length of the drawn wire is limited by the initial size of the LM droplet, and it is solely a manual method whereas the technique developed in this work requires

less manual effort with better control over the diameter of wire through the use of a motorized winder. Using this method, ultrafine conductive wires were able to be produced which may be used in future applications such as micro-electrode interconnects for nerve systems [132]–[134].

6.2.2 Spiral Pressure Sensor

In order to test the applicability of the coaxially extruded, stretchable, electrically conductive wires, the 3-axis system of the 3D printer was used to print a planar spiral pressure sensor onto a SEBS substrate, as inspired by Park et al. [135]. The ability for the sensor to conform to dynamic surfaces coupled with the durability of SEBS has immediate applications in wearable systems [135]. While LM filled micro-electronics as sensors have already been reported in literature [73], [135], [136], the novelty of the current research comes from the unique fabrication technique to directly print these functional devices in a single step as opposed to the multiple casting, injecting and sealing processes used previously.

The sensor was designed to have 2 mm thick extrudates with a 1 mm gap between adjacent traces. The size of the overall sensor was approximately 60 mm in diameter. The 3D model and the experimental setup are shown in Figure 45. The printed sensor with 22 gauge, 1-pin male to male jumper cables is shown in Figure 46(a). The elasticity of the SEBS allows the cable ends to simply be slid over top of the cable pins to interface to electronic equipment. This was the connection method used for connecting all of the liquid metal devices to electronic equipment.

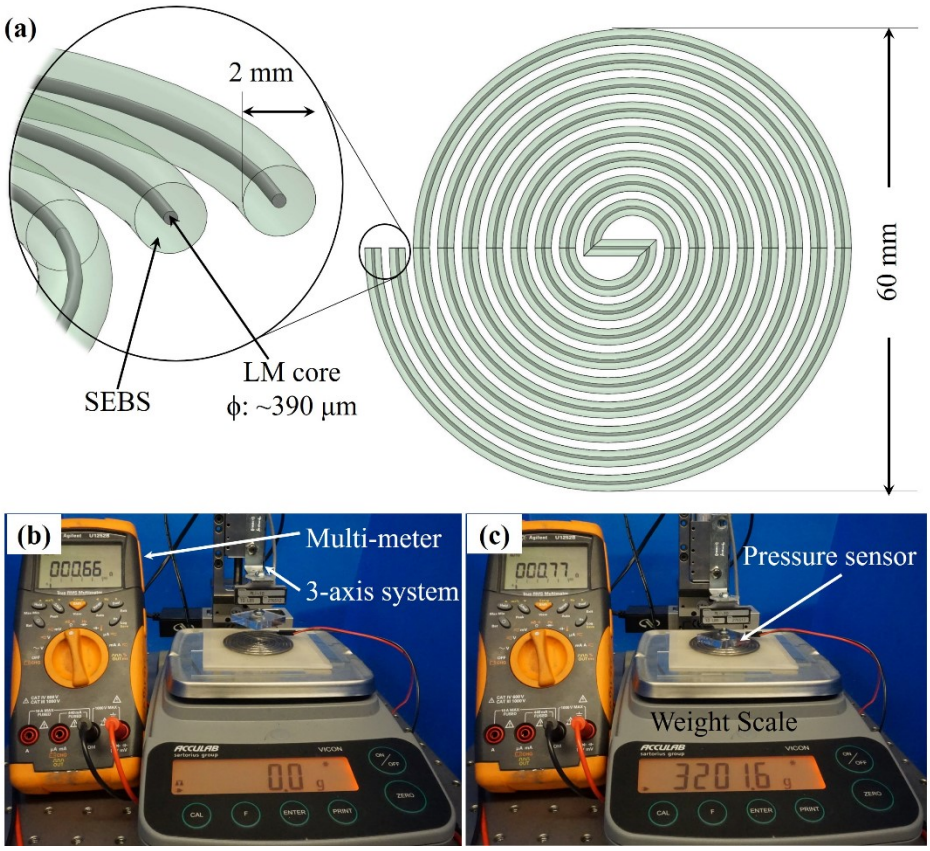

Figure 45. (a) 3D schematic of a 2D spiral pressure sensor composed of SEBS channels with a LM core printed directly on a SEBS substrate. (b) Experimental setup to measure change in electrical resistance as a function of pressure applied with no load and (c) with a load of 3.2 kg. Used with permission from [50].

The sensor was then connected to a multi-meter (Agilent, U1252B), and placed on a load cell underneath a 3-axis movement system, shown in Figure 45(b). A 30 x 30 x 6 mm piece of PMMA was attached to the movement system and lowered to apply a distributed pressure to the sensor. When a force is applied to the sensor, deformation of the circular cross-section of the LM core increases the length of the trace, resulting in an increase in the electrical resistance. The original electrical resistance of the un-stressed sensor was 0.66 Ω, which increased non-linearly to 0.77 Ω for a load of 3.2 kg, equivalent to 34.9 kPa. The non-linearity observed is supported by the model developed by Park et al [135]. Figure 46(b) also shows the change in electrical resistance as a function of the pressure applied.

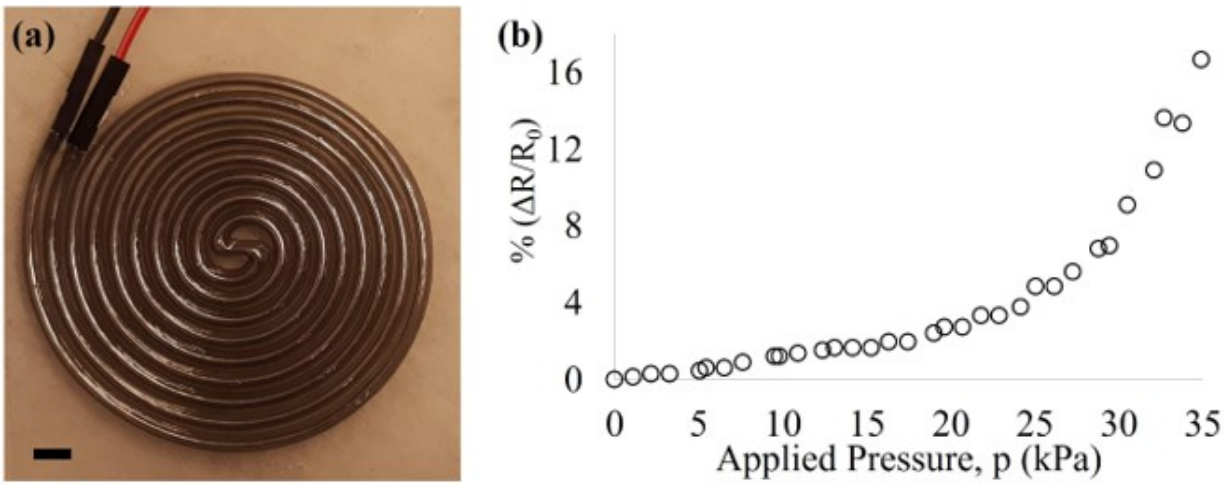

Figure 46. (a) SEBS/eGaIn spiral resistor pressure sensor. (b) Percent change of electrical resistance of the pressure sensor as a function of the applied pressure. Used with permission from [50].

The experiment was repeated 3 times and the plot in Figure 46(b) was produced from the average changes in resistance during loading and unloading.

6.2.3 3D Spiral Inductor

A three-dimensional stretchable inductor was also printed in this work as shown in Figure 47(a). The inductor has an outer diameter of 46 mm, a height of 40 mm, and 2 mm thick SEBS coils having a LM core of approximately 620 μm. A radial axisymmetric circumferential strain was applied on the inductor which resulted in a change in both the cross-sections of the individual LM cores in SEBS channels as well as the overall circular area perpendicular to the inductor axis. The inductance of the inductor (L) was computed using Equation 18,

$$L = \frac{\mu_o N^2 A}{h} \qquad \text{Eq. 11}$$

where μ_o is the permeability of vacuum, N is the number of coils, A is the cross-sectional circular area of the inductor, and h is the height of the inductor. As the inductor is uniformly radially expanded, the inductance increases as a function of its diameter (D) according to Equation 12, below. Details can be found in the Supporting Information.

$$L^2 \propto D^3 \qquad \text{Eq. 12}$$

In Figure 47(b), the relationship between the inductor's inductance and diameter is presented. Each measurement was repeated three times and their average data was used to plot the relationship. In Figure 47(b), the solid line represents the theoretical relation from Equation 12 and the open circles are experimental data points.

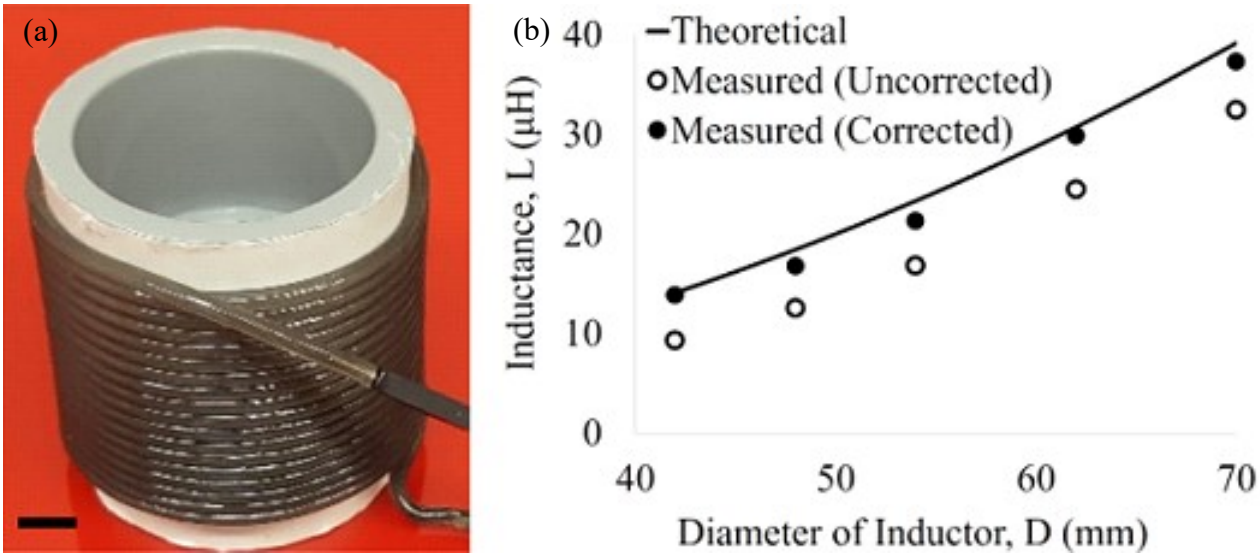

Figure 47. SEBS/eGaIn 3D spiral inductor. Used with permission from [50].

The data shows that inductance increases non-linearly with an increase in the inductor diameter. By introducing an aspect ratio correction factor, namely the Nagaoka coefficient (k) [137], the measured inductances were corrected, and it was found that the corrected data coincide well with the theoretical prediction. The minor discrepancy between predicted and corrected data is believed to be caused by the possible contact resistance and the self-inductance of the connecting wires.

6.3 Results and Discussion

While the FDM extruder system is much larger than typical microfluidics devices, the higher viscosities of thermoplastic melts provide similar Reynolds numbers and design principles applied to very laminar flows despite being a non-Newtonian fluid. Therefore, the coaxial extrusion of LM and SEBS can be explained by the dripping and jetting mechanism in coflowing microfluidic

systems of two immiscible fluids [138]. Dripping occurs when the inner fluid forms periodic droplets that pinch-off from the injecting tip. However, in the jetting regime, the inner fluid first forms a jet which may be broken up into droplets downstream away from the tip. The dynamics of this coflowing system are determined by the viscosities of both fluids and their average velocities, densities, surface tension, surface chemistry, and device geometry [139]. Once the LM is injected through a needle surrounded by the viscous polymer melt, two major forces define the continuity of the core fluid: the surface tension and viscous drag forces [140], as shown in Figure 48(c).

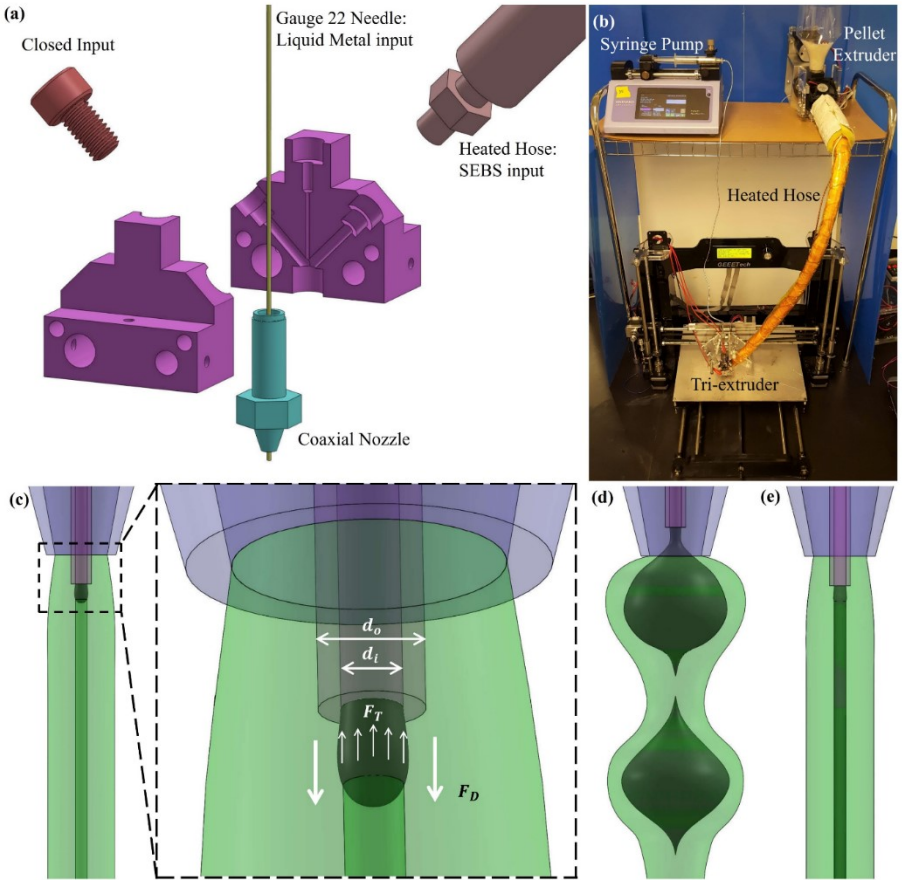

Figure 48. (a) Exploded view of the tri-extruder assembly used for coaxial extrusion, (b) Schematic of the 3D printing system showing the syringe pump at the top left, the pellet extruder at the top right with the heated hose (orange) and silicone tubing leading to the 3D printer nozzle, (c) Schematic view of the nozzle outlet. Inset: Detail view of the nozzle exit showing the coaxial nozzle diameters (d_o and d_i), the surface tension force of the LM (F_T), and the viscous drag force imparted by the SEBS (F_D). (d) Illustration showing the effect of surface tension dominating due to low viscosity of the polymer at high temperatures. (e) Illustration showing viscous drag of the SEBS being greater than the surface tension of the LM. Used with permission from [50].

In comparison with these forces, the effects of gravity, buoyancy, and momentum transfer terms can be assumed to be negligible [140]. Initially, the force due to interfacial surface tension (F_T) dominates the viscous drag applied by the outer fluid and minimizes the surface area by forming a spherical droplet that adheres to the needle. The surface tension force (F_T) is approximated to be

$$F_T \approx 1.3\pi d_i \gamma \quad \text{Eq. 13}$$

where d_i is the internal diameter of the LM needle and γ is the surface tension of the LM and molten SEBS interface [140]. On the other hand, the viscous drag force (F_D) forces the LM downstream away from the needle tip, which can be approximated from a modified version of the Stokes formula as:

$$F_D = 3\pi\eta_{SEBS}(d_{LM} - d_i)(u_{SEBS} - u_{LM}) \quad \text{Eq. 14}$$

where η_{SEBS} is the dynamic viscosity of the SEBS melt, u_{SEBS} is the average velocity of SEBS melt, u_{LM} is the average velocity of the LM and d_{LM} is the diameter of the LM core [140]. The viscous drag takes into account the shielding of the LM droplet due to the needle and reduction in drag due to the relative velocity between both fluids. Continuous feeding of LM causes the droplet to grow, which eventually contributes to an increase in the viscous drag. Once the viscous drag overcomes the surface tension force and the droplet is forced to move away from the needle, a slight undulation on the droplet tail forms. Due to Plateau-Rayleigh instabilities, the droplet is then pinched-off and encapsulated [141]. In this application, the LM droplets are oblong because the temperature of the polymer melt quickly drops below T_g and restricts droplets from becoming fully spherical. A 3D model of a discontinuous series of LM droplets encapsulated in SEBS is shown in Figure 48(d).

In order to achieve a continuous jet of LM encapsulated in SEBS, the viscous drag must be high enough to force LM away from the needle before droplets can grow, hence the following relationship must hold true:

$$1.3\pi d_i \gamma \leq 3\pi\eta_{SEBS}(d_{LM} - d_i)(u_{SEBS} - u_{LM}) \quad \text{Eq. 15}$$

which reduces to

$$d_{cr} \geq d_i \left[1 + \frac{1.3\,\gamma}{3\pi\eta_{SEBS}\,(u_{SEBS} - u_{LM})}\right] \quad \text{Eq. 16}$$

The viscosity of the polymer melt increases non-linearly by decreasing the temperature and shear rates outside of the nozzle. Hence, when the LM is injected, it is surrounded by the highly viscous polymer melt which restricts droplet growth, and the combined flow of both fluids favors the condition of a continuous jet as shown in Figure 48(e). The shear rate of the SEBS was assumed to be 10 s^{-1} for all cases immediately after exiting the nozzle tip. The shear rates were determined to be 2700 Pa·s and 2500 Pa·s for 180 °C and 200 °C, respectively, in previous work [128]. As suggested by Utada et al., the conditions favourable to continuous jet of LM encapsulated in SEBS can be expressed by the capillary number of the SEBS,

$$Ca_{SEBS} = \frac{\eta_{SEBS} u_{SEBS}}{\gamma} \quad \text{Eq. 17}$$

and the Weber number of the LM,

$$We_{LM} = \frac{\rho_{LM} d_{cr} u_{LM}^2}{\gamma} \quad \text{Eq. 18}$$

where d_{cr} is the critical minimum diameter of LM core which causes the force balance and favors the jet formation and ρ_{LM} is the density of LM [138]. By solving Equations 17 and 18 for u_{SEBS} and u_{LM}, respectively, the relationship shown in Equation 19 was derived.

$$\sqrt{We_{\mathrm{LM}}} \leq \left(\frac{\sqrt{\rho_{\mathrm{LM}} d_{\mathrm{cr}} \gamma}}{\eta_{\mathrm{SEBS}}}\right) Ca_{SEBS} - \left(\frac{1.3 d_{\mathrm{i}} \sqrt{\rho_{\mathrm{LM}} d_{\mathrm{cr}} \gamma}}{3\eta_{\mathrm{SEBS}}(d_{\mathrm{cr}} - d_{\mathrm{i}})}\right) \quad \text{Eq. 19}$$

Figure 49(a) presents a state diagram showing different combinations of Ca_{SEBS} and We_{LM} favourable to LM jet formation with a desired core diameter. The lines represent different conditions favourable according to Equation 15 to produce a LM wire with core diameters of 400, 700, and 1000 μm at 180 °C. Since the internal diameter of the needle used in this experiment was approximately 400 μm, using this setup, a wire with a core diameter less than 400 μm could not be produced without subsequent processing. Therefore, the area under the 400 μm curve (hatched region marked on the plot) corresponds to those conditions where rather than a continuous jet, a series of LM droplets were observed. Conversely, in the grey region above the 400 μm curve, a continuous jet can be achieved with different core diameters. In contrast to the lines which represent theoretical predictions, the data points show the experimental results when continuous jets with different core diameters were produced. Open circles represent where the desired core diameter was 400 μm, and there was a range of core diameters between 390 to 450 μm. Open triangles represent when the achieved core diameter was between 620 and 720 μm, and squares represent when the achieved core diameter was 1040 μm. However, in all cases, the requirement of the We_{LM} was higher than the theoretical expectations. It is believed to be a result of the assumptions made in this experiment and limitations of the experimental setup. The flow speeds of both SEBS (u_{SEBS}) and LM (u_{LM}) were varied to identify the combinations of Ca_{SEBS} and We_{LM} which were favourable to a continuous LM jet formation. A system was assumed to be favourable to a continuous jet if it produced extrudate over 1 m long without any discrete droplets of LM. It was further noticed that, at a very high We_{LM} and a relatively low Ca_{SEBS}, the higher feed rate of LM causes the droplets to grow quickly which eventually results in bursting and the LM becomes no longer contained in the SEBS shell. Figure 49(b) shows an extrudate with LM droplets which was produced using u_{SEBS} = 2 mm/s and u_{LM} = 2.5 mm/s at 180 °C which corresponds to Ca_{SEBS} = 8.3 and $We_{LM} = 9.8 \times 10^{-7}$. Their microscopic images are shown in the inset to observe the shape of the droplets and the sections between them. At 200 °C, when free extruding under gravity, the lower viscosity of the SEBS dictates the thinner size of the extrudate as shown in Figure 49(c),

which was produced with the same feed rates as the extrudate in Figure 49(b). By increasing the feed rate of LM from u_{LM} = 3.5 mm/s to u_{LM} = 4.5 mm/s, while keeping the same SEBS feed rate (u_{SEBS} = 2 mm/s), a larger diameter LM core was produced, as shown in Figure 49(d). Due to Plateau-Rayleigh instabilities, at very low LM feed rates, non-uniform pressure distribution along the length of the core cylindrical LM caused material displacement and resulted in discontinuities.

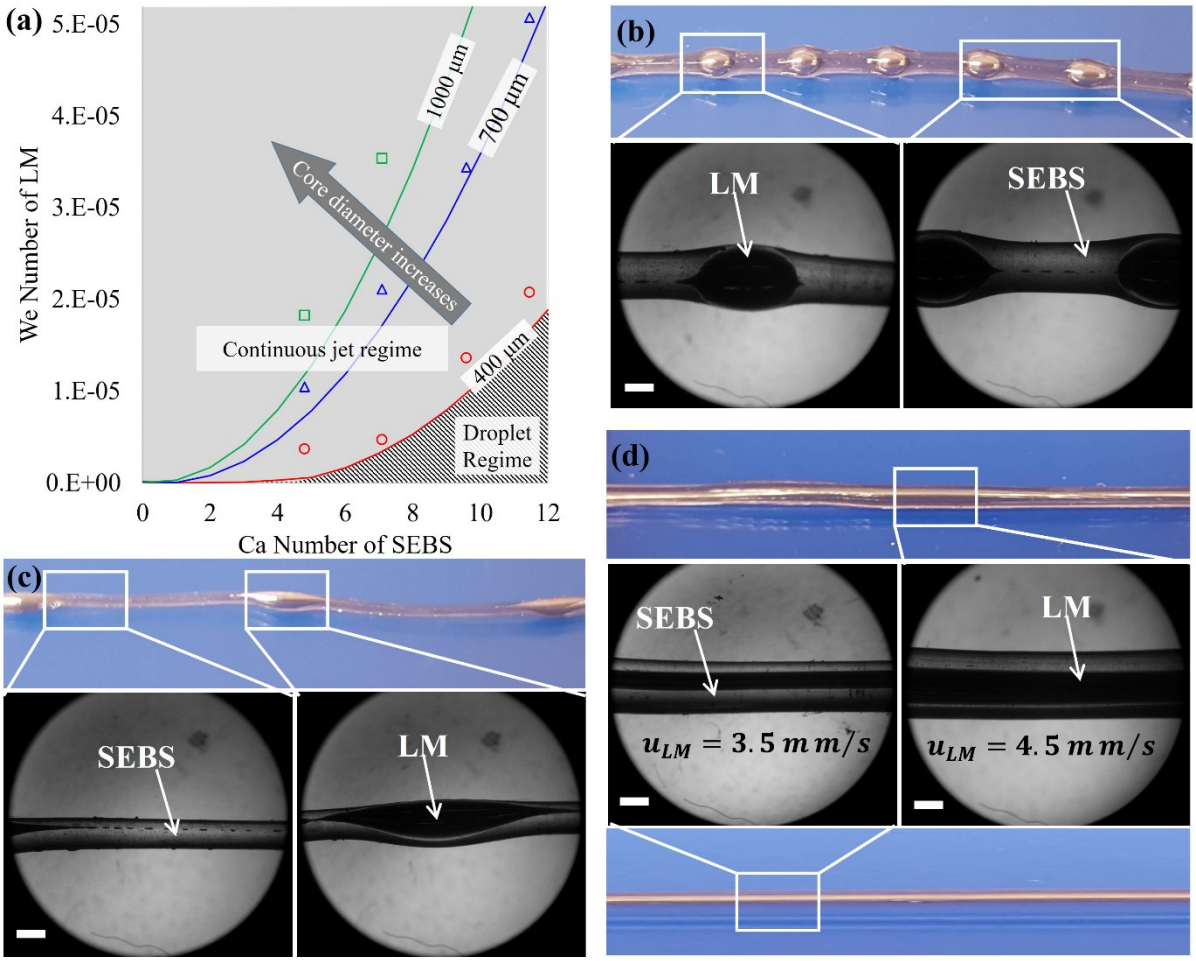

Figure 49. (a) State diagram showing the relationship between the Ca number of SEBS and the We number of LM, and how it affects the coaxial extrusion regime. The hatched region shows combinations of Ca and We numbers at which jet formation is not possible. A transition from the droplet regime to the continuous jet regime as the temperature increases from (b) 180 °C to (c) 200 °C is shown with flow rates of 2 mm/s and 2.5 mm/s for SEBS and LM, respectively. (d) Microscope image showing that increasing the flow rate of the LM caused the LM to be continuous and increase in diameter as the flow rate was further increased. Scale bars are 1 mm. Used with permission from [50].

Optical microscope images of the LM wires produced at different LM feed rates, but identical SEBS feed rates are shown in Figure 50(a)–(d). The diameter of the LM core increases with increasing LM feed rate. A simple stretch test was performed to show the elongation of the LM wire as shown in Figure 50(e) and (f), where no voids or loss of electrical conductivity were observed when stretched up to 4 times of its original length.

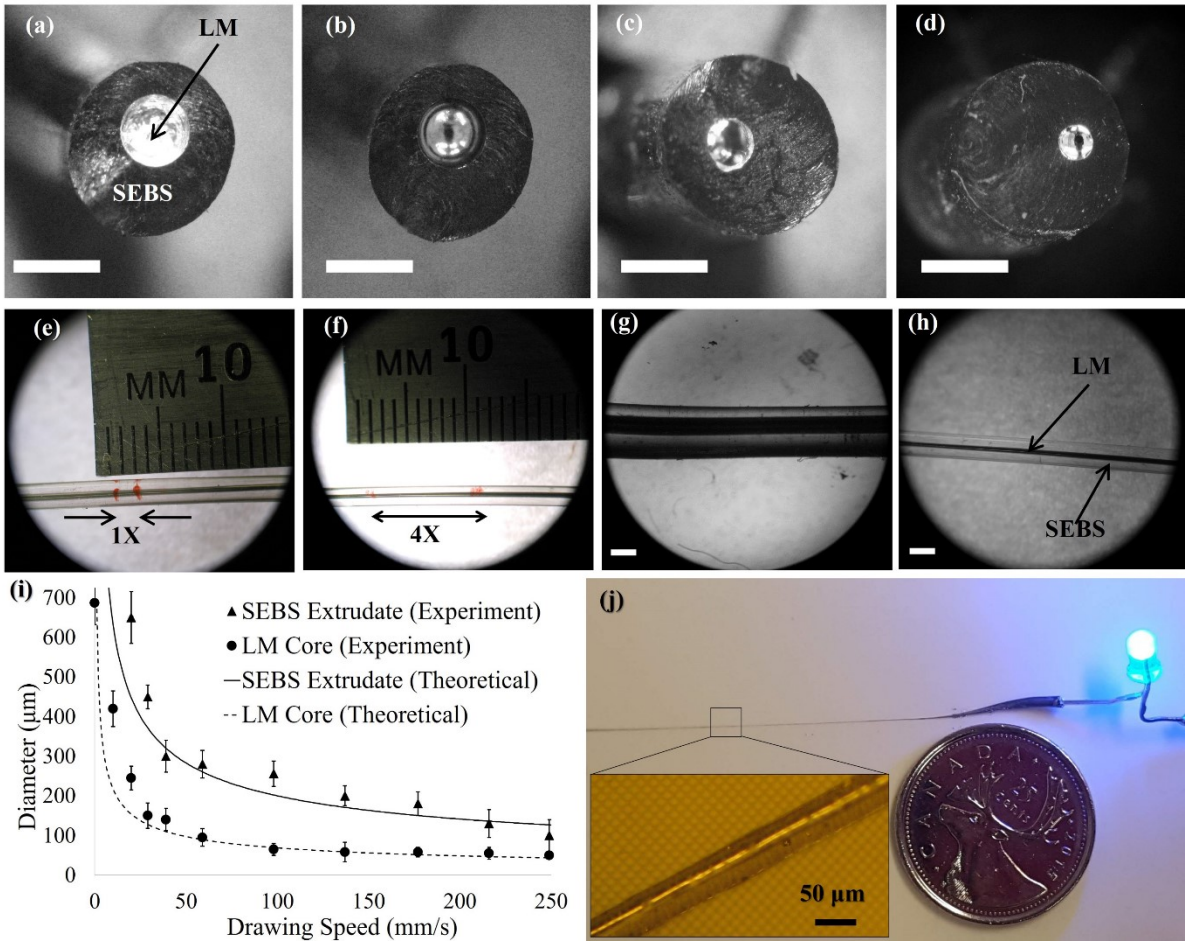

Figure 50. (a)-(d) Various cross-sections produced by holding the Ca number of the SEBS constant but decreasing the We number of the LM. (e) and (f) show repeatable stretchability of the wire up to 400 % with no noticeable decrease in electrical properties. (g) and (h) show the ability for the wire do be thermally drawn from a core diameter of approximately 670 µm to approximately 190 µm. (i) Graph showing the relationship between drawing speed and resultant diameter with agreement between the experimental devices and the theoretical values. (j) shows a drawn wire attached to an LED with electrical conductivity in the wire preserved. Used with permission from [50].

6.3.1 Drawing of the LM Wire

In order to produce wires with very fine LM diameters, an additional drawing step immediately after the coaxial LM wire is extruded can be applied, if the temperature of the polymer melt is still above the upper glass transition temperature (T_g). We assumed that the ratio of the diameters of LM core and SEBS shell would be constant. If there are no voids in the LM core, by considering a circular and uniform cross-section, Equation 20 can be derived from the conservation of mass.

$$\pi\left(\frac{d_{\text{Extrusion}}}{2}\right)^2 S_{Extrusion} = \pi\left(\frac{d_{Drawing}}{2}\right) S_{\text{Drawing}} \qquad \text{Eq. 20}$$

which reduces to

$$d_{\text{Drawing}} = d_{\text{Extrusion}} \sqrt{\frac{S_{\text{Extrusion}}}{S_{\text{Drawing}}}} \qquad \text{Eq. 21}$$

where $d_{Extrusion}$ is the diameter of either the as-extruded LM core or SEBS extrudate, $d_{Drawing}$ is their diameter after drawing, $S_{Extrusion}$ is the extrusion speed, and $S_{Drawing}$ is the drawing speed. The final size of the ultrafine LM wire was directly proportional to the square root of the ratio of extrusion speed to drawing speed. This fact was supported by the drawing test where the as-extruded wires were drawn in a controlled fashion using different drawing speeds. The test was performed using a motorized winder with a 7.5 cm wheel, placed on the print bed when the tri-extruder head was raised at a height of 20 cm above the bed. The motorized winder was placed directly below the nozzle so that only a vertically downward drawing force was applied. Figure 50(g) shows a wire having 670 ± 55 μm of LM core produced, which was then drawn with a speed of 30 mm/s resulting in a LM diameter core of approximately 190 μm, shown in Figure 50(h). Using this simple drawing technique, a LM microwire having a core diameter as narrow as 25 μm was achieved without any mechanical and electrical loss, by drawing with the maximum attainable speed (250 mm/s) of the current setup. After the drawing step, the LM micro-wires were examined using an optical microscope to measure the core and shell diameters. The plot in Figure 50(i) shows the effect of

the drawing speed on the size of the drawn wires. During this experiment, the average extrusion speed ($S_{Extrusion}$), core diameter, and shell diameter were kept constant at 1 mm/s, ≈ 620 μm, and ≈ 2000 μm, respectively. This plot suggests that as the drawing speed increases, initially the size of both the LM core and SEBS shell drastically decrease, and theoretically they should approach a plateau which would be determined by Plateau–Rayleigh instabilities and mechanical failures of the SEBS shell resulting in LM leakage. The latter effect might be partially attributed to the eccentricity of the LM core with respect to the SEBS shell due to alignment imperfections. A more concentric coaxial extrusion would further push the limit of the smallest size of drawn wires. The extremely rapid cooling of the extrudate prevents fully plastic behavior, and immediate drawing in a heated environment may potentially allow for the production of even smaller diameter wires. To demonstrate the electrical performance, a micro-wire (≈ 25 μm of LM core with ≈ 50 μm of SEBS shell) was used as a connector for an LED with no aging effect on its conductivity over a period of 72 h of continuous operation, shown in Figure 50(j). In the inset, a close-up microscopic image of the micro-wire is presented. This image was taken while the wire was placed on an array of microscale fibers with a 20 μm pitch to demonstrate the size of the wire. To analyze the electrical performance of the produced LM wire, A 10 cm long wire with a 2 mm SEBS shell and 620 μm LM core was used to observe the effect of cyclic stretching on the resistance of the conductor. From Figure 51, this relationship was found to be non-linear.

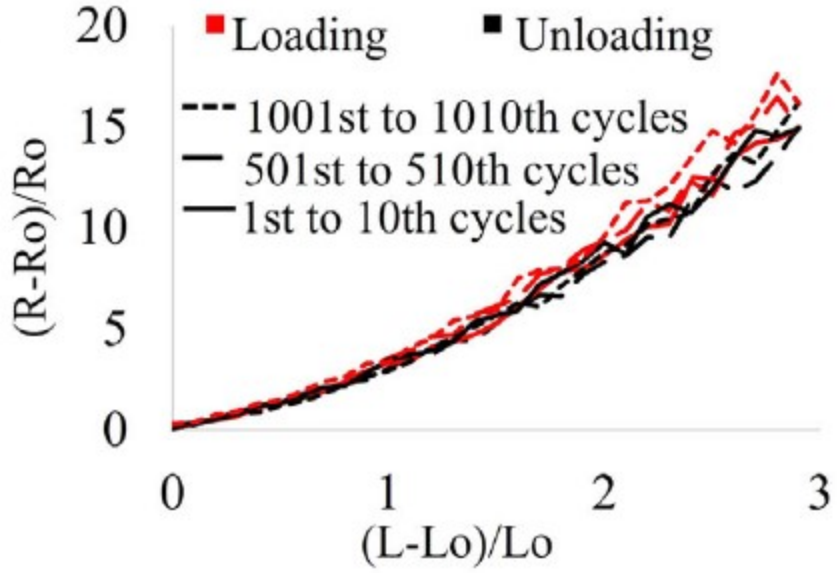

Figure 51. Plot of loading and unloading cycles of a 10 cm long SEBS/LM wire showing the relative change in resistance over a total of 1010 cycles. Used with permission from [50].

The graph shows three plots of the average change in resistance for the first 10 cycles, 501st to 510th cycles, and 1001st to 1010th cycles. The results show that there is a minimal effect on the average conductivity of liquid metal wire.

6.4 Conclusion and Future Work

In this chapter, a novel technique to directly print stretchable and flexible electronic devices by coaxially extruding an eGaIn LM core with an elastomeric shell made of SEBS was described. The mechanism of forming LM droplets versus a jet, which is described by a state diagram showing favourable conditions for a continuous LM core with a desired diameter was also discussed. This novel technique is the first of its kind to directly fabricate LM based conductive patterns in a single step without any post-processing such as injecting or casting. Along with coaxial extrusion, an additional immediate drawing step resulted in continuous high-quality LM microwires with core diameters as small as ≈ 25 μm. As well, the applicability of coaxial extrusion with a CNC-controlled setup was presented by fabricating and characterizing a resistive pressure sensor and an inductive strain sensor that both showed excellent repeatability over several loading and unloading cycles.

Future work on several facets of this work can be done to improve the quality and applicability of the LM wires:

- Investigations into reducing the diameter of the as-extruded wire diameters by using a smaller nozzle and a smaller diameter needle.
- Developing a mechanism to hold the LM needle more precisely concentric to the center of the nozzle.
- Developing other electronic devices that can benefit from the stretchability shown in this chapter.
- Developing a reliable interconnect method for interfacing the LM wires with conventional electronic devices. Although the jump cable connection method works as a proof of principle, a permanent connection that both provides sufficient strength to prevent disconnection of the wires, while also being compatible with the liquid metal alloy and copper wire needs to be designed.
- The technique developed in this chapter is believed to be equally useful for low-melting point metals or alloys with a hard thermoplastic shell for the applications where stretchability and flexibility are not desired, rather mechanical strength and rigidity are of primary concern. Conversely, alloys with melting points above room temperature, such as Field's Metal with a melting point of approximately 62 °C, may be able to be extruded within a flexible/stretchable core, allowing for the potential of a shape-memory composite wire.

Chapter 7: Conclusion

In this thesis, two general themes in the realm of polymer microfabrication were investigated: Polymer foams, and elastomeric devices enhanced by room temperature liquid metals. The methods in this thesis are not typical for polymer microfabrication and are often considered techniques for producing macroscale features. The continuous improvement, decreasing cost, and availability of FDM 3D printers has allowed for relatively accurate parts to be produced quickly with a large flexibility in the internal and external quality of features of the part. The work in this thesis took advantage of the mechanical aspect of these machines and coupled it with novel material combinations to produce highly functional parts directly off the printer. Several improvements have since been made to the printers in the lab, which will be detailed in future work.

Polymer foams were produced using soluble templates using solvent casting in the case of thermoplastic foams, and addition curing using thermosetting silicone foams with relative success. The applicability of an SEBS foam for non-polar liquid absorption was presented, but it was shown to be not structurally sound enough to return to its original shape after absorbing non-polar liquids. SEBS foams may be useful as a low-loss material for reconfigurable microwave antenna applications, due to the free space within the foam. Experiments using pure NaCl may show better results than with table salt and should be investigated. As well, using finer sizes of porogen should be investigated to determine a lower limit of pore size achievable using the templating method.

Thermoplastic foams were also produced using extrusion through an FDM nozzle after being preloaded with chemical foaming agents at temperatures below the foaming temperature, but above the T_g of the polymer. LLDPE and PLA foams were produced, requiring approximately a 30 % and 65 % reduction in extrusion speeds, respectively, to achieve identical extrudate thicknesses as that of virgin LLDPE and PLA. Future experiments are required to determine the optimal loading of foaming agent in LLDPE in order to produce as-printed densities comparable to those used by existing foundry casting operations.

eGaIn was used as a conductive liquid metal in two applications in this thesis. The first investigated its use as a reflective conductor for microwave arena applications. Several configurations of

reflector were investigated, with LM sandwiched between two layers of PDMS being the most effective. In order to produce an effective antenna assembly, improvements into reducing the bulging of the LM at the base of the reflector due to gravity need to be addressed. As well, an improved attachment method between the reflector and the antenna needs to be developed. The second LM experiment investigated its application as a core material in stretchable thermoplastic wires. The production and explanation of the mechanism of extrusion of the LM wires was discussed, detailing the distinct droplet and jetting regimes of the extrudate. Two devices were produced and characterized: a stretchable, planar, resistive spiral pressure sensor, and a 3D stretchable inductive strain sensor. The planar pressure sensor showed repeatable results up to a tested force of 3.2 kg, and the inductive strain sensor operated according to theoretical values with a correction factor applied. The applicability of the coaxial extrusion system lends itself to a vast number of material combinations, of which SEBS/LM wires can be used to immediately develop new electrical devices that can be used in highly dynamic applications, such as in wearables or neural interfaces. The work done in this thesis should hopefully provide a useful set of background knowledge for future researchers pursuing improvements to the experiments performed within this document or to those desiring to utilize the knowledge to develop novel and low-complexity methods for polymer microfabrication.

Bibliography

[1] P. Abgrall, V. Conedera, H. Camon, A. M. Gue, and N. T. Nguyen, "SU-8 as a structural material for labs-on-chips and microelectromechanical systems (review)," *Electrophoresis*, vol. 28, no. 24, pp. 4539–4551, 2007, doi: 10.1002/elps.200700333.

[2] O. Breuer and U. Sundararaj, "Big returns from small fibers: A review of polymer/carbon nanotube composites," *Polym Compos*, vol. 25, no. 6, pp. 630–645, 2004, doi: 10.1002/pc.20058.

[3] T. D. Ngo, A. Kashani, G. Imbalzano, K. T. Q. Nguyen, and D. Hui, "Additive manufacturing (3D printing): A review of materials, methods, applications and challenges," *Compos B Eng*, vol. 143, no. December 2017, pp. 172–196, 2018, doi: 10.1016/j.compositesb.2018.02.012.

[4] P. Sen and C. Kim, "Microscale Liquid-Metal Switches — A Review," *IEEE Transactions on Industrial Electronics*, vol. 56, no. 4, pp. 1314–1330, 2009, doi: 10.1109/TIE.2008.2006954.

[5] S. Cheng and Z. Wu, "Microfluidic electronics," *Lab Chip*, vol. 12, no. 16, pp. 2782–2791, 2012, doi: 10.1039/c2lc21176a.

[6] S. Lacour, "Stretchable Electronics," in *Stretchable Electronics*, T. Someya, Ed. John Wiley & Sonds, 2012, pp. 81–109. doi: 10.1002/9783527646982.

[7] N. Kazem, T. Hellebrekers, and C. Majidi, "Soft Multifunctional Composites and Emulsions with Liquid Metals," *Advanced Materials*, vol. 1605985, pp. 1–14, 2017, doi: 10.1002/adma.201605985.

[8] D. H. Kim and J. A. Rogers, "Stretchable electronics: Materials strategies and devices," *Advanced Materials*, vol. 20, no. 24, pp. 4887–4892, 2008, doi: 10.1002/adma.200801788.

[9] J. A. Rogers, R. Ghaffari, and D.-H. Kim, *Stretchable Bioelectronics for Medical Devices and Systems*. 2016. doi: 10.1007/978-3-319-28694-5.

[10] M. A. H. Khondoker and D. Sameoto, "Fabrication methods and applications of microstructured gallium based liquid metal alloys," *Smart Mater Struct*, vol. 25, no. 9, p. 093001, 2016, doi: 10.1088/0964-1726/25/9/093001.

[11] I. D. Joshipura, H. R. Ayers, C. Majidi, and M. D. Dickey, "Methods to pattern liquid metals," *J Mater Chem C Mater*, vol. 3, no. 16, pp. 3834–3841, 2015, doi: 10.1039/c5tc00330j.

[12] E. Aram and S. Mehdipour-Ataei, "A review on the micro- and nanoporous polymeric foams: Preparation and properties," *International Journal of Polymeric Materials and Polymeric Biomaterials*, vol. 65, no. 7, pp. 358–375, 2016, doi: 10.1080/00914037.2015.1129948.

[13] D. Zhu, S. Handschuh-Wang, and X. Zhou, "Recent progress in fabrication and application of polydimethylsiloxane sponges," *J Mater Chem A Mater*, vol. 5, no. 32, pp. 16467–16497, 2017, doi: 10.1039/c7ta04577h.

[14] K. M. Z. Andalib, "Increasing Void Fraction of the Polypropylene Foams Blown with Chemical Blowing Agents in High Temperature Extrusion," University of Toronto, 2015. [Online]. Available: https://tspace.library.utoronto.ca/handle/1807/70214

[15] "Standard Specification for Rigid, Cellular Polystyrene Thermal Insulation," *ASTM C578-19*. pp. 1–8, 2019.

[16] L. Cui, S. Kiernan, and M. D. Gilchrist, "Designing the energy absorption capacity of functionally graded foam materials," *Materials Science and Engineering A*, vol. 507, no. 1–2, pp. 215–225, 2009, doi: 10.1016/j.msea.2008.12.011.

[17] M. Sadighi and S. J. Salami, “An investigation on low-velocity impact response of elastomeric & crushable foams,” *Central European Journal of Engineering*, vol. 2, no. 4, pp. 627–637, 2012, doi: 10.2478/s13531-012-0026-0.

[18] M. Kozlowski, “Lightweight Plastic Materials,” in *Thermoplastic Elastomers*, A. Z. El-Sonbati, Ed. Intech Open, 2012, p. 291. doi: 10.5772/37624.

[19] D. N. H. Tran, S. Kabiri, T. R. Sim, and D. Losic, “Selective adsorption of oil–water mixtures using polydimethylsiloxane (PDMS)–graphene sponges,” *Environ. Sci.: Water Res. Technol*, vol. 1, no. 1, pp. 298–305, 2014, doi: 10.1039/c5ew00035a.

[20] S. J. Choi *et al.*, “A polydimethylsiloxane (PDMS) sponge for the selective absorption of oil from water,” *ACS Appl Mater Interfaces*, vol. 3, no. 12, pp. 4552–4556, 2011, doi: 10.1021/am201352w.

[21] R. A. Mrozek, C. S. Gold, B. Leighliter, J. M. Sietins, and J. L. Lenhart, “Open pore, elastomeric scaffolds through frustrated particle collapse,” *J Mater Sci*, vol. 51, no. 24, pp. 10761–10774, 2016, doi: 10.1007/s10853-016-0288-7.

[22] J. Reignier and M. A. Huneault, “Preparation of interconnected poly(ε-caprolactone) porous scaffolds by a combination of polymer and salt particulate leaching,” *Polymer (Guildf)*, vol. 47, no. 13, pp. 4703–4717, 2006, doi: 10.1016/j.polymer.2006.04.029.

[23] O. Kilic, S. Acar, A. Kisasoz, and K. A. Guler, “Investigation of carbon contamination in lost foam castings of low carbon steel,” *China Foundry*, vol. 15, no. 5, pp. 384–389, 2018, doi: 10.1007/s41230-018-8091-5.

[24] K. Siavashi, “The Effect of Casting Parameters on the Fluidity and Porosity of Aluminium Alloys in the Lost Foam Casting Process,” University of Birmingham, 2011.

[25] X. J. Liu, S. H. Bhavnani, and R. A. Overfelt, “Simulation of EPS foam decomposition in the lost foam casting process,” *J Mater Process Technol*, vol. 182, no. 1–3, pp. 333–342, 2007, doi: 10.1016/j.jmatprotec.2006.08.023.

[26] F. Li, H. Zhao, F. Ren, S. Song, X. Shao, and A. A. Volinsky, "Simulations and experiments of mould filling in lost foam casting," *International Journal of Cast Metals Research*, vol. 33, no. 4–5, pp. 194–200, 2020, doi: 10.1080/13640461.2020.1822572.

[27] "Polymer Foam Market Size | Global Industry Forecast [2020-2027]." https://www.fortunebusinessinsights.com/industry-reports/polymer-foam-market-101698 (accessed Sep. 23, 2022).

[28] X. Zhao, L. Li, B. Li, J. Zhang, and A. Wang, "Durable superhydrophobic/superoleophilic PDMS sponges and their applications in selective oil absorption and in plugging oil leakages," *J. Mater. Chem. A*, vol. 2, no. 43, pp. 18281–18287, 2014, doi: 10.1039/C4TA04406A.

[29] A. Stevenson, "Engineering with Elastomers," in *Rubber Technologist's Handbook*, S. K. De and J. R. White, Eds. Rapra Technology Limited, 2001, p. 287.

[30] D. Chen, J. Yang, and S. Kitipornchai, "Free and forced vibrations of shear deformable functionally graded porous beams," *Int J Mech Sci*, vol. 108–109, pp. 14–22, 2016, doi: 10.1016/j.ijmecsci.2016.01.025.

[31] M. F. Ahmed, Y. Li, Z. Yao, K. Cao, and C. Zeng, "TPU/PLA blend foams: Enhanced foamability, structural stability, and implications for shape memory foams," *J Appl Polym Sci*, vol. 136, no. 17, pp. 1–12, 2019, doi: 10.1002/app.47416.

[32] T. Tezel, V. Kovan, H. E. Camurlu, and E. S. Topal, "Designing and Manufacturing of Polymer-Foam Hybrid Materials Using Fused Deposition Modeling," *Adv Eng Mater*, vol. 21, no. 6, pp. 1–7, 2019, doi: 10.1002/adem.201800840.

[33] B. Koohbor, G. Youssef, K. Z. Uddin, and Y. Kokash, "Dynamic Behavior and Impact Tolerance of Elastomeric Foams Subjected to Multiple Impact Conditions," *Journal of Dynamic Behavior of Materials*, vol. 8, no. 3, pp. 359–370, 2022, doi: 10.1007/s40870-022-00340-z.

[34] Y. Hong, J. Guan, K. L. Fujimoto, R. Hashizume, A. L. Pelinescu, and W. R. Wagner, "Tailoring the degradation kinetics of poly(ester carbonate urethane)urea thermoplastic elastomers for tissue engineering scaffolds," *Biomaterials*, vol. 31, no. 15, pp. 4249–4258, 2010, doi: 10.1016/j.biomaterials.2010.02.005.

[35] "ISO 18064 - Thermoplastic Elastomers - Nomenclature and abbreviated terms," vol. 2014. 2015.

[36] D. Handlin, C. Ting, Z. Cheng, and P. Davé, "Soft , processable SEBS polymers for compounds," *Rubber World*, pp. 45–49, Oct. 2016.

[37] I. Mathew, K. E. George, and D. J. Francis, "Viscous and elastic behaviour of SEBS triblock copolymer," *Die Angewandte Makromolekulare Chemie*, vol. 217, no. 1, pp. 51–59, 1994, doi: 10.1002/apmc.1994.052170106.

[38] S. B. Hamilton, "Rtv Silicone Adhesive Sealants," in *Automotive Engineerin Congress*, 1971. doi: 10.1201/9781315136691-15.

[39] Momentive Performance Materials, "RTV157 and RTV159 Technical Data Sheet."

[40] A. del Campo and C. Greiner, "SU-8: a photoresist for high-aspect-ratio and 3D submicron lithography," *J. Micromech. Microeng. J. Micromech. Microeng*, vol. 17, no. 17, pp. 81–95, 2007, doi: 10.1088/0960-1317/17/6/R01.

[41] MicroChem, "SU-8 Permanent Photoresists Resist Description." http://www.microchem.com/pdf/SU-8-table-of-properties.pdf (accessed Mar. 21, 2017).

[42] R. Y. Lukin, A. M. Kuchkaev, A. v. Sukhov, G. E. Bekmukhamedov, and D. G. Yakhvarov, "Platinum-catalyzed hydrosilylation in polymer chemistry," *Polymers (Basel)*, vol. 12, no. 10, pp. 1–22, 2020, doi: 10.3390/POLYM12102174.

[43] A. J. Chalk and J. F. Harrod, “Homogeneous Catalysis II. The Mechanism of the Hydrosilation of Olefins Catalyzed by Group VIII Metal Complexes,” *J. Am. Chem. Soc.*, vol. 87, no. 1, pp. 16–21, 1965.

[44] Z. X. Zhang, X. R. Dai, L. Zou, S. B. Wen, T. K. Sinha, and H. Li, “A developed, eco-friendly, and flexible thermoplastic elastomeric foam from sebs for footwear application,” *Express Polym Lett*, vol. 13, no. 11, pp. 948–958, 2019, doi: 10.3144/expresspolymlett.2019.83.

[45] L. Q. Xu and H. X. Huang, “Foaming of poly(lactic acid) using supercritical carbon dioxide as foaming agent: Influence of crystallinity and spherulite size on cell structure and expansion ratio,” *Ind Eng Chem Res*, vol. 53, no. 6, pp. 2277–2286, 2014, doi: 10.1021/ie403594t.

[46] J. Grimminger and K. Muha, “Silicone surfactants for pentane blown rigid foam,” *Journal of Cellular Plastics*, vol. 29, no. 5, pp. 474–476, 1993, doi: 10.1177/0021955X9302900589.

[47] J. W. S. Lee and C. B. Park, “Use of nitrogen as a blowing agent for the production of fine-celled high-density polyethylene foams,” *Macromol Mater Eng*, vol. 291, no. 10, pp. 1233–1244, 2006, doi: 10.1002/mame.200600203.

[48] A. Sahnoune, “Foaming of thermoplastic elastomers with water,” *Journal of Cellular Plastics*, vol. 37, no. 2, pp. 149–159, 2001, doi: 10.1106/E7WD-X288-XFK7-6E90.

[49] N. LeMaster, “Tips and Techniques: How to Mold & Extrude Using Chemical Foaming Agents | Plastics Technology,” Jan. 28, 2011. https://www.ptonline.com/articles/how-to-mold-extrude-using-chemical-foaming-agents (accessed Sep. 30, 2022).

[50] M. A. H. Khondoker, A. Ostashek, and D. Sameoto, “Direct 3D Printing of Stretchable Circuits via Liquid Metal Co-Extrusion Within Thermoplastic Filaments,” *Adv Eng Mater*, vol. 21, no. 7, 2019, doi: 10.1002/adem.201900060.

[51] S. Zhu *et al.*, “Ultrastretchable fibers with metallic conductivity using a liquid metal alloy core,” *Adv Funct Mater*, vol. 23, no. 18, pp. 2308–2314, 2013, doi: 10.1002/adfm.201202405.

[52] M. Zandvakili, “Liquid Metal Based Test Structures and Reconfigurable Microfluidic Microwave devices and Antennas,” University of Alberta, 2017.

[53] Kraton Corporation, “Kraton ® G1657 M Polymer.” pp. 29–31, 2009.

[54] B. Tao *et al.*, “Determination of the Contents of Antioxidants and Their Degradation Products in Sodium Chloride Injection for Blood Transfusion,” *J Anal Methods Chem*, vol. 2020, 2020, doi: 10.1155/2020/8869576.

[55] J. Sanhueza, S. Nieto, and A. Valenzuela, “Thermal stability of some commercial synthetic antioxidants,” *JAOCS, Journal of the American Oil Chemists’ Society*, vol. 77, no. 9, pp. 933–936, 2000, doi: 10.1007/s11746-000-0147-9.

[56] J. Kovarova, J. Rotschova, O. Brede, and M. Burgers, “The effect of transformation products of the antioxidant BHT on the initial stages of thermo- and photo-oxidation of LDPE,” *Can J Chem*, vol. 73, no. 11, pp. 1862–1868, 1995, doi: 10.1139/v95-230.

[57] F. Sonnenberg, “Lost Foam Beads for Aluminum and Iron Castings,” in *Lost Foam - Casting Made Simple*, A. C. 11-D., Ed. American Foundry Society (AFS), 2008, pp. 71–83.

[58] H. Z. Chen, Z. de Shan, and H. Z. Dong, “Research of foam pattern processing for lost foam casting,” *Applied Mechanics and Materials*, vol. 331, pp. 600–603, 2013, doi: 10.4028/www.scientific.net/AMM.331.600.

[59] X. Xiao, Q. Xue, K. Xiao, and X. Hu, “LFC mold development of complex parts with free-form surface,” *Adv Mat Res*, vol. 228–229, pp. 532–536, 2011, doi: 10.4028/www.scientific.net/AMR.228-229.532.

[60] F. Sonnenberg, “Lost foam pattern molding,” in *Lost Foam - Casting Made Simple*, A. C. 11-D., Ed. American Foundry Society (AFS), 2008, pp. 99–107.

[61] F. Sonnenberg, “Metalcasting and the Lost Foam Process,” in *Lost Foam - Casting Made Simple*, AFS Committee 11-D., Ed. American Foundry Society (AFS), 2008, p. 1.

[62] A. Ergut, Y. A. Levendis, and J. Carlson, “Emissions from the combustion of polystyrene, styrene and ethylbenzene under diverse conditions,” *Fuel*, vol. 86, no. 12–13, pp. 1789–1799, 2007, doi: 10.1016/j.fuel.2007.01.009.

[63] X. J. Liu, R. A. Overfelt, and S. H. Bhavnani, “The effects of foam density and metal velocity on the heat and mass transfer in the lost foam casting process,” *Proceedings of the ASME Summer Heat Transfer Conference*, vol. 2003, pp. 317–323, 2003, doi: 10.1115/ht2003-47504.

[64] X. J. Liu, S. H. Bhavnani, and R. A. Overfelt, “Measurement of kinetic zone temperature and heat Transfer coefficient in the lost foam casting process,” *American Society of Mechanical Engineers, Heat Transfer Division, (Publication) HTD*, vol. 375, no. 3, pp. 411–418, 2004, doi: 10.1115/IMECE2004-59348.

[65] X. J. Liu, S. H. Bhavnani, and R. A. Overfelt, “Numerical Modeling of EPS Foam Decomposition in the Lost Foam Casting Process,” in *2005 ASME International Mechanical Engineering Congress and Exposition*, 2005, pp. 1–9.

[66] D. Garlotta, “A literature review of poly(lactic acid),” *J Polym Environ*, vol. 9, no. 2, pp. 63–84, 2001.

[67] Y. Di, S. Iannace, E. di Maio, and L. Nicolais, “Reactively modified poly (lactic acid): Properties and foam processing,” *Macromol Mater Eng*, vol. 290, no. 11, pp. 1083–1090, 2005, doi: 10.1002/mame.200500115.

[68] K. Oluwabunmi, N. A. D’Souza, W. Zhao, T. Y. Choi, and T. Theyson, “Compostable, fully biobased foams using PLA and micro cellulose for zero energy

buildings," *Sci Rep*, vol. 10, no. 1, pp. 1–20, 2020, doi: 10.1038/s41598-020-74478-y.

[69] "Athena of Velletri by CosmoWenman - Thingiverse." https://www.thingiverse.com/thing:196039 (accessed Oct. 01, 2022).

[70] "*MINI* All In One 3D printer test by majda107 - Thingiverse." https://www.thingiverse.com/thing:2806295 (accessed Oct. 01, 2022).

[71] "Density of Plastics Material: Technical Properties Table." https://omnexus.specialchem.com/polymer-properties/properties/density (accessed Oct. 22, 2022).

[72] A. Alonso, D. Lázaro, M. Lázaro, and D. Alvear, "Self-heating evaluation on thermal analysis of polymethyl methacrylate (PMMA) and linear low-density polyethylene (LLDPE)," *J Therm Anal Calorim*, vol. 147, no. 18, pp. 10067–10081, 2022, doi: 10.1007/s10973-022-11364-x.

[73] M. D. Dickey, R. C. Chiechi, R. J. Larsen, E. A. Weiss, D. A. Weitz, and G. M. Whitesides, "Eutectic gallium-indium (EGaIn): A liquid metal alloy for the formation of stable structures in microchannels at room temperature," *Adv Funct Mater*, vol. 18, no. 7, pp. 1097–1104, 2008, doi: 10.1002/adfm.200701216.

[74] M. Abu and H. Khondoker, "Development of a Multi-material Extruder System to 3D Print Hard Thermoplastics , Soft Elastomers and Liquid Metals," Dissertation, University of Alberta, 2019.

[75] J. E. Chandler, H. H. Messer, and G. Ellender, "Cytotoxicity of Gallium and Indium Ions Compared with Mercuric Ion," *J Dent Res*, vol. 73, no. 9, pp. 1554–1559, 1994, doi: 10.1177/00220345940730091101.

[76] M. D. Dickey, "Stretchable and Soft Electronics using Liquid Metals," *Advanced Materials*, vol. 1606425, pp. 1–19, 2017, doi: 10.1002/adma.201606425.

[77] Y. Lin *et al.*, "Drawing liquid metal wires at room temperature," *Extreme Mech Lett*, vol. 7, pp. 55–63, 2016, doi: 10.1016/j.eml.2016.03.010.

[78] F. Scharmann *et al.*, "Viscosity effect on GaInSn studied by XPS," *Surface and Interface Analysis*, vol. 36, no. 8, pp. 981–985, 2004, doi: 10.1002/sia.1817.

[79] R. F. Service, "Electronic textiles charge ahead," *Science*, vol. 301, no. 5635, pp. 909–911, Aug. 2003. doi: 10.1126/science.301.5635.909.

[80] M. Kubo *et al.*, "Stretchable microfluidic radiofrequency antennas," *Advanced Materials*, vol. 22, no. 25, pp. 2749–2752, 2010, doi: 10.1002/adma.200904201.

[81] H. Moghadas, M. Zandvakili, D. Sameoto, and P. Mousavi, "Beam-Reconfigurable Aperture Antenna by Stretching or Reshaping of a Flexible Surface," *IEEE Antennas Wirel Propag Lett*, vol. 16, pp. 1337–1340, 2017.

[82] D. J. Hartl, G. J. Frank, G. H. Huff, and J. W. Baur, "A liquid metal-based structurally embedded vascular antenna : I. Concept and multiphysical modeling," *Smart Mater Struct*, vol. 26, no. February, p. 025002, 2017, doi: 10.1088/1361-665X/aa5142.

[83] D. J. Hartl, G. J. Frank, and J. W. Baur, "Embedded magnetohydrodynamic liquid metal thermal transport: Validated analysis and design optimization," *J Intell Mater Syst Struct*, vol. 28, no. 7, pp. 862–877, 2017, doi: 10.1177/1045389X16657429.

[84] H. Yamaguch, X.-D. Niu, and X.-R. Zhang, "Application of graphene and graphene-based materials in clean energy-related devices Minghui," *Int J Energy Res*, vol. 35, no. 1, pp. 209–220, 2011, doi: 10.1002/er.1685.

[85] A. F. Chrimes, K. J. Berean, A. Mitchell, G. Rosengarten, and K. Kalantar-Zadeh, "Controlled Electrochemical Deformation of Liquid-Phase Gallium," *ACS Appl Mater Interfaces*, vol. 8, no. 6, pp. 3833–3839, 2016, doi: 10.1021/acsami.5b10625.

[86] K. Kim, S. Kim, T. Kim, W. Kim, and J. Lee, "Spray-Coated Liquid Metal Reflectors for Transparent Hydrogel Atomic Force Microscope Cantilevers," *Journal of*

Microelectromechanical Systems, vol. 25, no. 5, pp. 848–850, 2016, doi: 10.1109/JMEMS.2016.2589539.

[87] E. S. Elton *et al.*, "Dramatic effect of oxide on measured liquid metal rheology," *J Rheol (N Y N Y)*, vol. 64, no. 1, pp. 119–128, 2020, doi: 10.1122/1.5117144.

[88] W. Xie, F. M. Allioux, J. Z. Ou, E. Miyako, S. Y. Tang, and K. Kalantar-Zadeh, "Gallium-Based Liquid Metal Particles for Therapeutics," *Trends Biotechnol*, vol. 39, no. 6, pp. 624–640, 2021, doi: 10.1016/j.tibtech.2020.10.005.

[89] D. Morales, N. A. Stoute, Z. Yu, D. E. Aspnes, and M. D. Dickey, "Liquid gallium and the eutectic gallium indium (EGaIn) alloy: Dielectric functions from 1.24 to 3.1 eV by electrochemical reduction of surface oxides," *Appl Phys Lett*, vol. 109, no. 9, 2016, doi: 10.1063/1.4961910.

[90] D. Manasijević, D. Živković, I. Katayama, and Ž. Živković, "Calculation of activities in some gallium-based systems with a miscibility gap," *Journal of the Serbian Chemical Society*, vol. 68, no. 8–9, pp. 665–675, 2003, doi: 10.2298/JSC0309665M.

[91] B. P. Pashaev and V. v. Seleznev, "Magnetic susceptibility of gallium-indium alloys in liquid state," *Izvestiya Vysshikh Uchebnykh Zavedenii, Fizika*, no. 4, pp. 134–136, 1973.

[92] J. Row and C. Tsai, "Pattern Reconfigurable Antenna Array With Circular Polarization," *IEEE Trans Antennas Propag*, vol. 64, no. 4, pp. 1525–1530, 2016.

[93] W. S. Kang, J. A. Park, and Y. J. Yoon, "Simple reconfigurable antenna with radiation pattern," *Electron Lett*, vol. 44, no. 3, 2008, doi: 10.1049/el.

[94] J. Hu, S. Lin, and F. Dai, "Pattern Reconfigurable Antenna Based on Morphing Bistable Composite Laminates," *IEEE Trans Antennas Propag*, vol. 65, no. 5, pp. 2196–2207, 2017, doi: 10.1109/TAP.2017.2677258.

[95] J. Ren, X. Yang, J. Yin, and Y. Yin, “A Novel Antenna with Reconfigurable Patterns Using H-Shaped Structures,” *IEEE Antennas Wirel Propag Lett*, vol. 14, no. 1, pp. 915–918, 2015, doi: 10.1109/LAWP.2014.2387292.

[96] A. Dey and G. Mumcu, “Microfluidically Controlled Frequency-Tunable Monopole Antenna for High-Power Applications,” *IEEE Antennas Wirel Propag Lett*, vol. 15, pp. 226–229, 2016, doi: 10.1109/LAWP.2015.2438863.

[97] M. M. Finckenor and K. K. de Groh, “Space Environmental Effects,” 2015.

[98] C. Durin, J. C. Mandeville, and J. M. Perrin, “Active detection of micrometeoroids and space debris SODAD-2 experiment on SAC-D satellite,” *Advances in Space Research*, vol. 69, no. 10, pp. 3856–3863, 2022, doi: 10.1016/j.asr.2022.02.045.

[99] B. Ruben *et al.*, “Oxygen plasma treatments of polydimethylsiloxane surfaces: Effect of the atomic oxygen on capillary flow in the microchannels,” *Micro Nano Lett*, vol. 12, no. 10, pp. 754–757, 2017, doi: 10.1049/mnl.2017.0230.

[100] S. Gialanella and A. Malandruccolo, *Aerospace Alloys*. Springer, 2020.

[101] A. M. A. El-hameed and Y. A. Abdel-Aziz, “Aluminium Alloys in Space Applications : A Short Report,” *Journal of Advanced Research in Applied Sciences and Engineering Technology*, vol. 1, no. 1, pp. 1–7, 2021, doi: 10.37934/araset.22.1.17.

[102] “Aluminum Alloy Database,” in *Table 4b. Typical Physical Properties of Wrought Aluminum Alloys (Metric Units)*, Knovel. [Online]. Available: https://app.knovel.com/hotlink/itble/id:kt00UBBRY2/table-4b-typical-physical/table-4b-typical-physical

[103] K. Narh, V. Dwivedi, J. Grow, A. Stana, and W. Y. Shih, “The effect of liquid gallium on the strengths of stainless steel and thermoplastics,” *J Mater Sci*, vol. 33, pp. 329–337, 1998, doi: 10.1023/A:1004359410957.

[104] J. Y. Uan and C. C. Chang, “Gallium-induced magnesium enrichment on grain boundary and the gallium effect on degradation of tensile properties of aluminum alloys,” *Metall Mater Trans A Phys Metall Mater Sci*, vol. 37, no. 7, pp. 2133–2145, 2006, doi: 10.1007/BF02586134.

[105] T. Mae and S. Hori, “Embrittlement of aluminum by liquid gallium,” in *Keikinzoku*, 1984, vol. 34, no. 1, pp. 3–7.

[106] Y. L. Park, B. R. Chen, and R. J. Wood, “Design and fabrication of soft artificial skin using embedded microchannels and liquid conductors,” *IEEE Sens J*, vol. 12, no. 8, pp. 2711–2718, 2012, doi: 10.1109/JSEN.2012.2200790.

[107] S. Yang, P. Liu, M. Yang, Q. Wang, J. Song, and L. Dong, “From Flexible and Stretchable Meta-Atom to Metamaterial: A Wearable Microwave Meta-Skin with Tunable Frequency Selective and Cloaking Effects,” *Sci Rep*, vol. 6, no. February, pp. 1–9, 2016, doi: 10.1038/srep21921.

[108] M. D. Bartlett, A. Fassler, N. Kazem, E. J. Markvicka, P. Mandal, and C. Majidi, “Stretchable, High-k Dielectric Elastomers through Liquid-Metal Inclusions,” *Advanced Materials*, vol. 28, no. 19, pp. 3726–3731, 2016, doi: 10.1002/adma.201506243.

[109] a Fassler and C. Majidi, “Soft-matter capacitors and inductors for hyperelastic strain sensing and stretchable electronics,” *Smart Mater Struct*, vol. 22, no. 5, p. 055023, 2013, doi: 10.1088/0964-1726/22/5/055023.

[110] S. Eom and S. Lim, “Stretchable complementary split ring resonator (CSRR)-based radio frequency (RF) sensor for strain direction and level detection,” *Sensors (Switzerland)*, vol. 16, no. 10, pp. 1–12, 2016, doi: 10.3390/s16101667.

[111] K. Jakus, J. E. Riiter, and C. A. Larsen, “Crazing and acoustic emission in poly(methyl methacrylate)/acetone and polystyrene/methanol systems,” *Polym Eng Sci*, vol. 21, no. 13, pp. 854–858, 1981.

[112] L. G. Stevens and C. E. T. White, “Indium and Bismuth,” in *Properties and Selection: Nonferrous Alloys and Special-Purpose Materials*, vol. 2, ASM International, 1990, pp. 750–757. doi: 10.31399/asm.hb.v02.a0001092.

[113] P. Geddis, L. Wu, A. McDonald, S. Chen, and B. Clements, “Effect of static liquid galinstan on common metals and non-metals at temperatures up to 200 °C,” *Can J Chem*, vol. 98, no. 12, pp. 787–798, 2020, doi: 10.1139/cjc-2020-0227.

[114] O. H., “Fe-Ga (Iron-Gallium),” *J Phase Equilibria Diffus*, vol. 25, p. 100, 2004.

[115] A. Fassler and C. Majidi, “Liquid-Phase Metal Inclusions for a Conductive Polymer Composite,” pp. 1928–1932, 2015, doi: 10.1002/adma.201405256.

[116] “Ecoflex ™ Series Technical Bulletin.”

[117] G. Agarwal, N. Besuchet, B. Audergon, and J. Paik, “Stretchable Materials for Robust Soft Actuators towards Assistive Wearable Devices,” *Sci Rep*, vol. 6, no. September, pp. 1–8, 2016, doi: 10.1038/srep34224.

[118] U. Daalkhaijav, O. D. Yirmibesoglu, S. Walker, and Y. Mengüç, “Rheological Modification of Liquid Metal for Additive Manufacturing of Stretchable Electronics,” *Adv Mater Technol*, vol. 3, no. 4, pp. 1–9, 2018, doi: 10.1002/admt.201700351.

[119] H. Chang *et al.*, “Recoverable Liquid Metal Paste with Reversible Rheological Characteristic for Electronics Printing,” *ACS Appl Mater Interfaces*, vol. 12, no. 12, pp. 14125–14135, 2020, doi: 10.1021/acsami.9b20430.

[120] L. E. Helseth, “Interdigitated electrodes based on liquid metal encapsulated in elastomer as capacitive sensors and triboelectric nanogenerators,” *Nano Energy*, vol. 50, no. April, pp. 266–272, 2018, doi: 10.1016/j.nanoen.2018.05.047.

[121] H. L. Yan *et al.*, “Coaxial printing method for directly writing stretchable cable as strain sensor,” *Appl Phys Lett*, vol. 109, no. 8, pp. 1–5, 2016, doi: 10.1063/1.4961493.

[122] Y. Yu, F. Liu, and J. Liu, “Direct 3D printing of low melting point alloy via adhesion mechanism,” *Rapid Prototyp J*, vol. 23, no. 3, pp. 642–650, 2017, doi: 10.1108/RPJ-12-2015-0185.

[123] D. Sameoto, “Manufacturing Approaches and Applications for Bioinspired Dry Adhesives,” in *Bio-inspired Structured Adhesives*, 9th ed., Springer International, 2017, pp. 221–244. doi: 10.1007/978-3-319-59114-8_11.

[124] M. A. Paglicawan and J. R. Celorico, “Properties of styrene-ethylene-butylene styrene block copolymer/exfoliated graphite nanoplatelets nanocomposites,” *Polymers and Polymer Composites*, vol. 29, no. 9_suppl, pp. S154–S165, 2021, doi: 10.1177/0967391121991290.

[125] P. Gupta, M. Bera, and P. K. Maji, “Nanotailoring of sepiolite clay with poly [styrene-b-(ethylene-co-butylene)-b-styrene]: structure–property correlation,” *Polym Adv Technol*, vol. 28, no. 11, pp. 1428–1437, 2017, doi: 10.1002/pat.4019.

[126] M. A. H. Khondoker, A. Asad, and D. Sameoto, “Printing with mechanically interlocked extrudates using a custom bi-extruder for fused deposition modelling,” *Rapid Prototyp J*, vol. 24, no. 6, pp. 921–934, 2018, doi: 10.1108/RPJ-03-2017-0046.

[127] M. A. H. Khondoker, N. Baheri, and D. Sameoto, “Tendon-Driven Functionally Gradient Soft Robotic Gripper 3D Printed with Intermixed Extrudate of Hard and Soft Thermoplastics,” *3D Print Addit Manuf*, vol. 6, no. 4, pp. 191–203, 2019, doi: 10.1089/3dp.2018.0102.

[128] M. A. H. Khondoker and D. Sameoto, “Direct coupling of fixed screw extruders using flexible heated hoses for FDM printing of extremely soft thermoplastic elastomers,” *Progress in Additive Manufacturing*, vol. 4, no. 3, pp. 197–209, 2019, doi: 10.1007/s40964-019-00088-4.

[129] “Filastruder Kit.” https://www.filastruder.com/products/filastruder-kit?variant=323882043 (accessed Oct. 01, 2022).

[130] “Geeetech Prusa I3 M201 - Geeetech Wiki.” https://www.geeetech.com/wiki/index.php/Geeetech_Prusa_I3_M201 (accessed Oct. 01, 2022).

[131] K. Polat and M. Şen, “Preparation and characterization of a thermoplastic proton-exchange system based on SEBS and polypropylene blends,” vol. 11, no. 3, pp. 209–218, 2017.

[132] N. Hallfors, A. Khan, M. D. Dickey, and A. M. Taylor, “Integration of pre-aligned liquid metal electrodes for neural stimulation within a user-friendly microfluidic platform,” *Lab Chip*, vol. 13, no. 4, pp. 522–526, 2013, doi: 10.1039/c2lc40954b.

[133] J. A. Bamford, R. Marc Lebel, K. Parseyan, and V. K. Mushahwar, “The fabrication, implantation, and stability of Intraspinal Microwire arrays in the spinal cord of cat and rat,” *IEEE Transactions on Neural Systems and Rehabilitation Engineering*, vol. 25, no. 3, pp. 287–296, 2017, doi: 10.1109/TNSRE.2016.2555959.

[134] A. Toossi, D. G. Everaert, A. Azar, C. R. Dennison, and V. K. Mushahwar, “Mechanically Stable Intraspinal Microstimulation Implants for Human Translation,” *Ann Biomed Eng*, vol. 45, no. 3, pp. 681–694, 2017, doi: 10.1007/s10439-016-1709-0.

[135] Y. L. Park, C. Majidi, R. Kramer, P. Brard, and R. J. Wood, “Hyperelastic pressure sensing with a liquid-embedded elastomer,” *Journal of Micromechanics and Microengineering*, vol. 20, no. 12, 2010, doi: 10.1088/0960-1317/20/12/125029.

[136] H. J. Kim, C. Son, and B. Ziaie, “A multiaxial stretchable interconnect using liquid-alloy-filled elastomeric microchannels,” *Appl Phys Lett*, vol. 92, no. 1, pp. 1–4, 2008, doi: 10.1063/1.2829595.

[137] R. H. Nagaoka, “The Inductance Coefficients of Solenoids,” *Journal of the College of Science, Imperial University*, vol. 27, no. 6, pp. 1–33, 1909.

[138] A. S. Utada, A. Fernandez-Nieves, H. A. Stone, and D. A. Weitz, “Dripping to jetting transitions in coflowing liquid streams,” *Phys Rev Lett*, vol. 99, no. 9, pp. 1–4, 2007, doi: 10.1103/PhysRevLett.99.094502.

[139] J. Eggers, “Nonlinear dynamics and breakup of free-surface flows,” *Rev Mod Phys*, vol. 69, no. 3, pp. 865–926, 1997, [Online]. Available: papers2://publication/uuid/1329B18C-197E-4787-8771-930B99E1706E

[140] P. B. Umbanhowar, V. Prasad, and D. A. Weitz, “Monodisperse emulsion generation via drop break off in a coflowing stream,” *Langmuir*, vol. 16, no. 2, pp. 347–351, 2000, doi: 10.1021/la990101e.

[141] Y. Li, J. Zhai, D. Xu, and G. Chen, “The study of Plateau–Rayleigh instability with DPD,” *Eur Phys J Plus*, vol. 136, no. 6, 2021, doi: 10.1140/epjp/s13360-021-01599-2.

Appendices

Appendix A – Table of Material Properties

Material	Material Type	Density [g/cm^3]	Tensile Strength [MPa]	Yield Strength [MPa]	Elongation to Failure [%]	Hardness	Electrical Conductivity [S/m]
AA6061-T6	Aluminum alloy	2.7	310	276	12	95 HBW (500 kg)	2.5×10^7
EcoFlex 00-30	Thermoset	1.07	1.4	N/A	900	Shore 00-30	N/A
eGaIn	Gallium alloy	6.3	N/A	N/A	N/A	N/A	3.4×10^6
Grey Cast Iron	Cast iron	7.2	207	N/A	N/A	174 – 210 HBW (3000 kg)	1.3×10^6
Kraton G1657 (SEBS)	Thermoplastic elastomer	0.90	23.4	N/A	750	Shore A-47	N/A
LLDPE	Thermoplastic	0.91	Not reported	Not reported	Not reported	Not reported	N/A
LW-PLA	Thermoplastic	0.4 – 1.24	Not reported	Not reported	Not reported	Not reported	N/A

Appendix B – Reconfigurable Horn Antenna Drawing

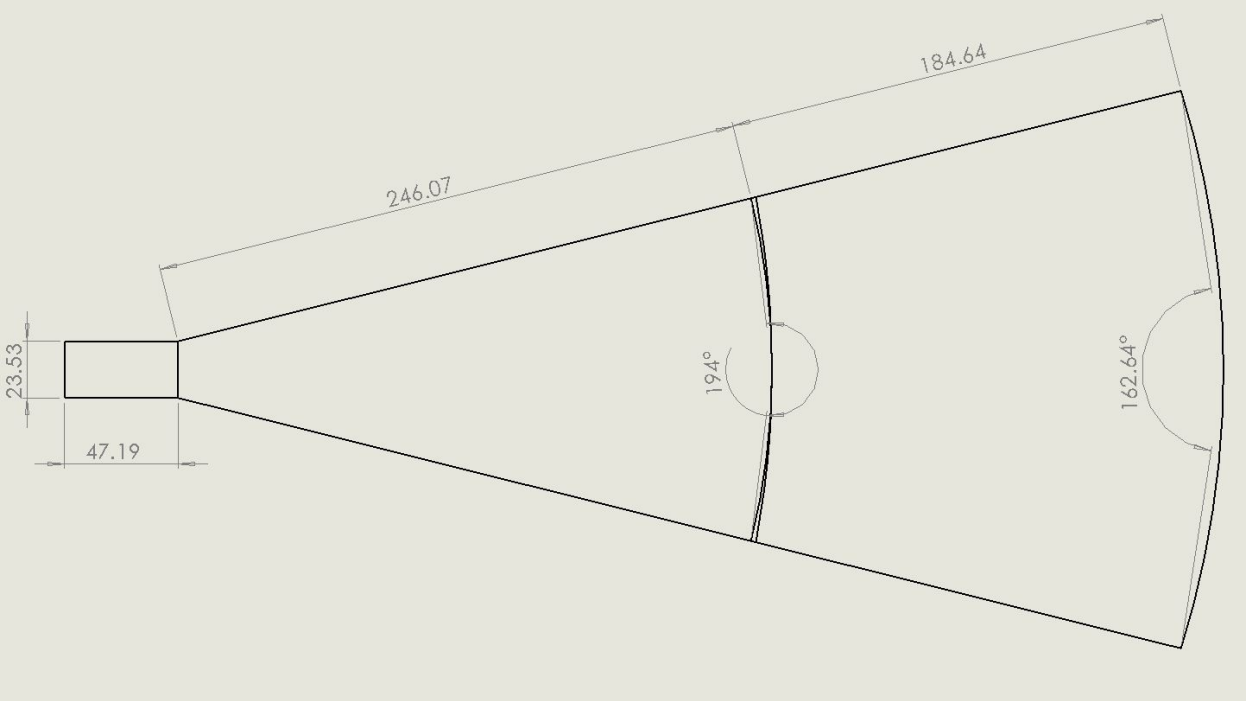

Figure B1. Antenna Top View

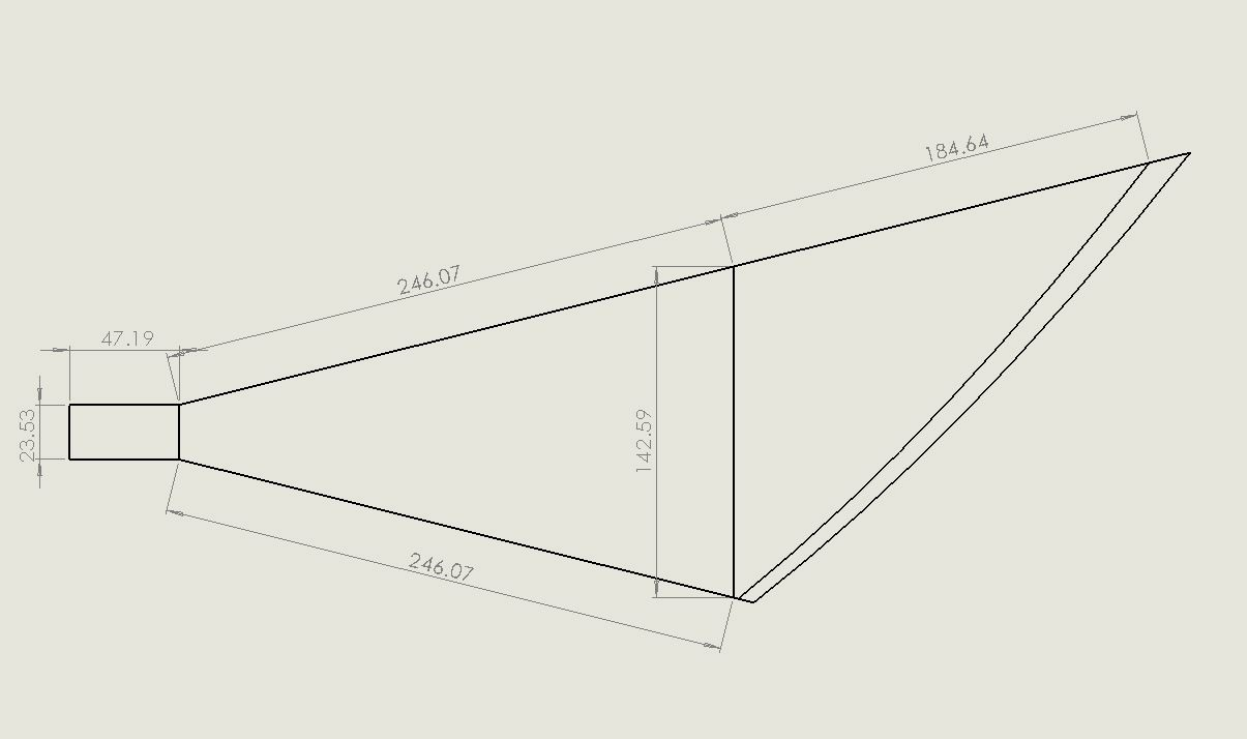

Figure B2. Antenna Side View

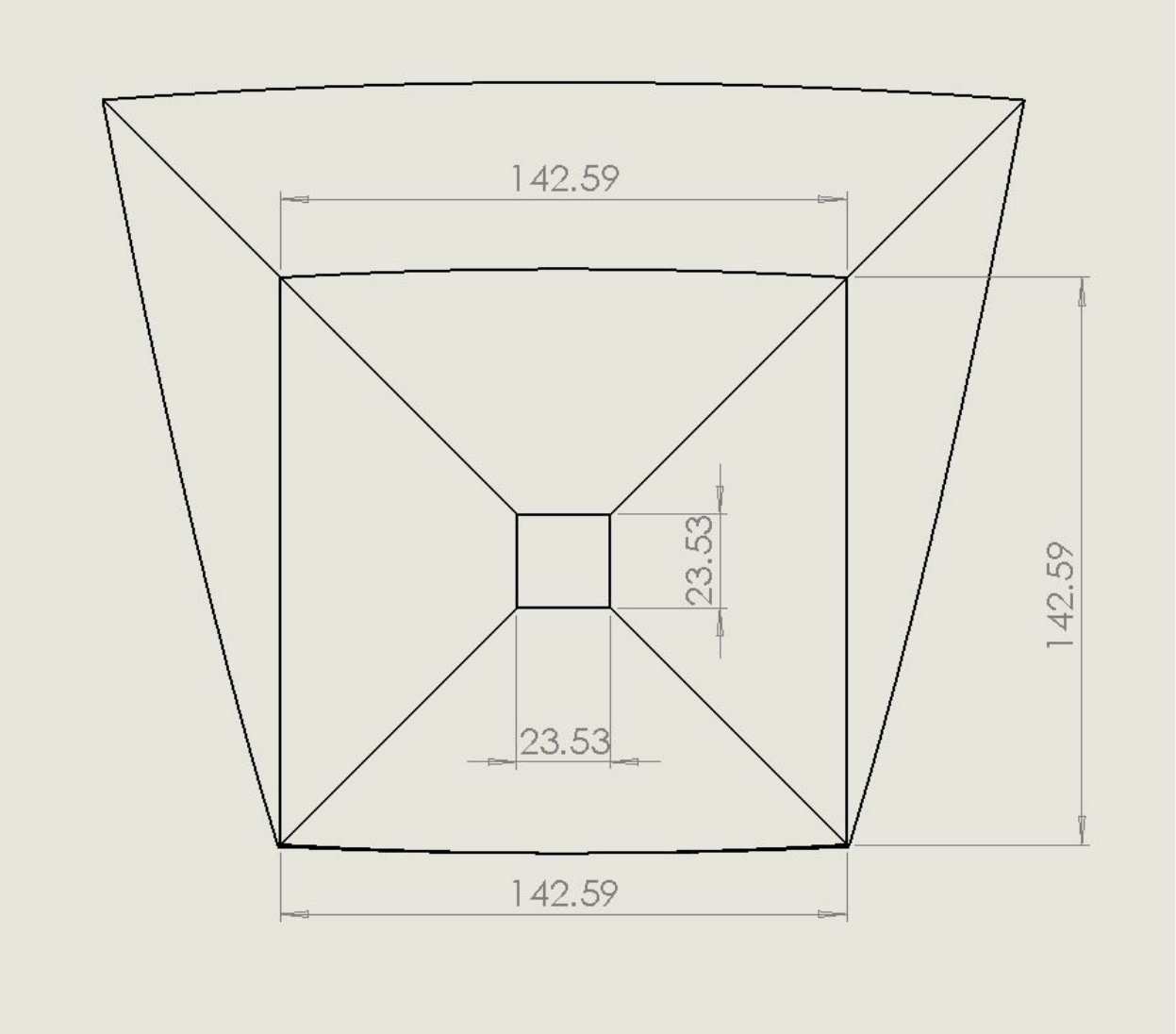

Figure B2. Antenna Rear View

Appendix C – Phase Diagram

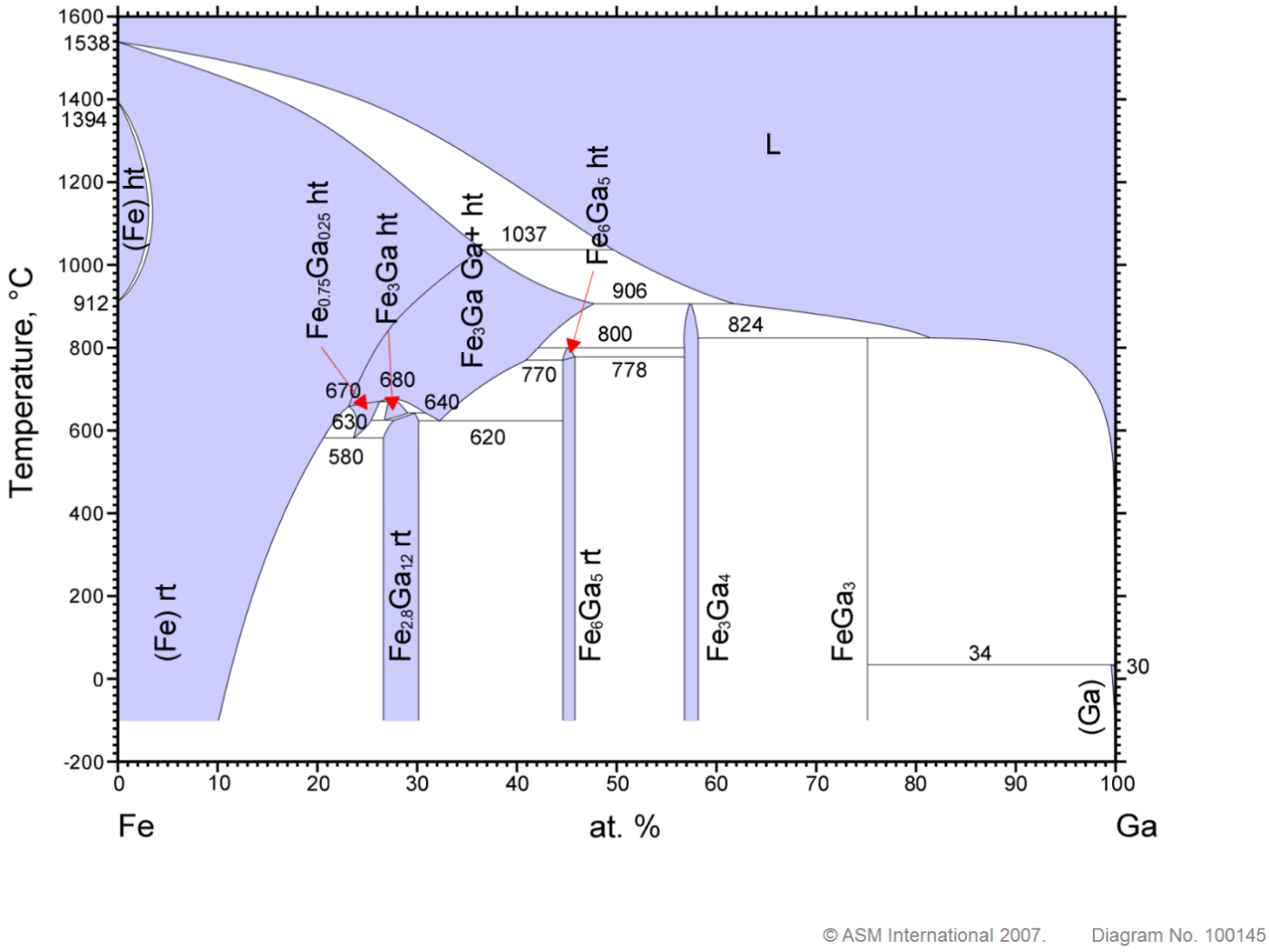

Figure C1. Fe-Ga Phase Diagram [114]